Thèse de Thanh Hai Nguyen, Lille 1, 2011

Université des Sciences and Technologies de Lille
Ecole Doctorale Sciences pour l'Ingénieur, Université Lille Nord−de−France

THÈSE

Présentée à

L'Université des Sciences et Technologies de Lille

Pour obtenir le titre de
DOCTEUR DE L'UNIVERSITÉ
Spécialité: Micro et Nanotechnologies
Par
Thanh Hai NGUYEN

Tunneling spectroscopy of hetero−nanocrystals

Soutenue le 29 novembre 2011 devant la commission d'examen composée de:

Tuami LASRI	Président
Damien RIEDEL	Rapporteur
Roland CORATGER	Rapporteur
Gerhard MEYER	Examinateur
Bruno GRANDIDIER	Directeur de thèse

© 2012 Tous droits réservés.

http://doc.univ-lille1.fr

© 2012 Tous droits réservés.

Abstract

Semiconductor colloidal nanocrystals are quite attractive, because of their physical properties, such as discrete energy levels, which can be easily tailored from the variation of their size and chemical composition, and also because of their compatibility with the fabrication of low–cost electronic devices. However, devices prepared from semiconductor nanocrystals are still facing limitations due to a high environmental sensitivity of their organic shell. In order to increase their optical properties, core–shell nanocrystals have thus been synthesized, where a new degree of freedom is offered by the presence of a junction between two types of semiconductor material.

Scanning tunneling microscopy is the appropriate tool to image and probe the electronic properties of individual nanostructures and, in particular, of heterostructure nanocrystals. This system can be compared to a double barrier tunnel junction, where the transport properties are governed by the transmission probability across both potential barriers (chapter 1). In principle, the synthesis of an homogenenous shell around the core should thus favor the charging phenomena.

In order to investigate the Coulomb effect in those quantum objects by tunneling spectroscopy (this technique being described in chapter 2), the thesis has first focussed on a prototypical model: an isolated silicon dangling bond, where its charge state has been changed in a controlled manner (chapter 3). Then, PbSe/CdSe core-shell nanocrystals have been studied and a general method is described to correctly identify the electrical nature of the charge carriers in the tunneling spectra (chapter 4). In contrast to nanocrystals that are covered by a layer of ligands only, the transport through core-shell structures reveals, for a majority of nanocrystals, that the same type of charge carrier tunnel on both sides of the apparent gap. Charging peaks are also observed and allow the measurements of the charging energy in these systems. A similar transport regime is obtained for CdSe/CdS dot in rod nanocrystals (chapter 5), demonstrating the reproducibility of the characterized transport phenomena when the nanocrystals consist of a heterostructure.

© 2012 Tous droits réservés.

Thèse de Thanh Hai Nguyen, Lille 1, 2011

© 2012 Tous droits réservés.

http://doc.univ-lille1.fr

Résumé

Les nanocristaux semi-conducteurs possèdent des tailles qui se situent entre celles des molécules et des matériaux cristallins. Leurs propriétés physiques sont donc dominées par des effets de confinement quantique, leur spectre d'énergie étant caractérisé par des états électroniques discrets. Une telle structure électronique leur confère d'être des sources de lumière de longueur d'onde accordable, très prisées pour l'imagerie biologique. Cependant, pour palier aux problèmes de photostabilité et accroître les applications potentielles de ces objets, des nanocristaux à hétérostructures, formés généralement d'un cœur et d'une coquille, de composition chimique différente du cœur, ont été synthétisées ces dernières années. Une étude approfondie de leur structure électronique et en particulier de la localisation des porteurs de charge s'avère nécessaire pour pouvoir à plus long terme faire de l'ingénierie de structure de bande de manière similaire à ce qui existe avec des hétérostructures semi-conductrices réalisées à partir de matériaux massifs.

La microscopie à effet tunnel est l'outil idéal pour imager et sonder les propriétés électroniques de nanocristaux individuels déposés sur une surface. Le système peut être comparé à une jonction tunnel à doublé barrière tunnel, dont les propriétés de transport sont en partie déterminees par les probabilités de transmission au travers de chaque barrière de potentiel (chapitre 1). A priori, la présence d'une coquille homogène autour du cœur doit favoriser le blocage de Coulomb dans de tels nanocristaux.

Pour caractériser les effets de Coulomb dans des objets quantiques par spectroscopie tunnel (technique détaillée au chapitre 2), mes travaux de recherche ont tout d'abord porté sur un système modèle : une liaison pendante silicium, dont l'état de charge a pu être modifié de manière contrôlée (chapitre 3). Des nanocristaux cœur–coquille (PbSe/CdSe) à symétrie sphérique ont ensuite été étudiés (chapitre 4). Pour lever toute ambiguïté sur la nature électrique des porteurs de charge, les mesures sont effectuées en variant l'épaisseur de la jonction tunnel entre la pointe et les nanocristaux. Contrairement aux nanocristaux sans coquille, les expériences révèlent que le transport est dominé par le même type de porteurs de charge à polarisation positive et négative de la jonction. Ces mesures donnent également accès à l'énergie de charge des nanocristaux. Un régime de transport similaire est obtenu pour des nanobâtonnets constitués d'un cœur sphérique CdSe enfermé dans un bâtonnet de CdS (chapitre 5), démontrant la reproductibilité des phénomènes observés lorsque les nanocristaux sont constitués d'hétérostructures cœur–coquille.

© 2012 Tous droits réservés.

© 2012 Tous droits réservés.

Acknowledgement

This thesis had been done at the Institut Supérieur d'Electronique et du Numérique Institute of Electronic (ISEN) and Microelectronic and Nanotechnology (IEMN) since December 2008. I want to thank Mr Alain Cappy and Mr Lionel Buchaillot for their authorization to work in the laboratory at ISEN and IEMN.

I want to thank to Mr Tuami Larsi for his acceptance to be the president of the jury of my thesis defend, also, I send my thanks to Mr Damien Riedel and Mr Roland Coratger who agreed to be referees for my thesis. I also want to thank Mr Gerhard Meyer for his agreement to attend my thesis defend as an opponent.

I also adore Mr Bruno Grandidier for his supervision and support during last three years. Under his supervising and his collaboration I can get a wide range of experience and good knowledge about experimental achievement which allows me to have a thesis defend.

Also, I want to say thank to Jean–Philipps Nys, Dominique Deresmes for their experimental supports during the time at IEMN and ISEN. Those made my research can be proved sufficiently.

I thank to Florence Senez and Christelle Sethi-Fouque for her organization of my thesis defend.

I also want to thanks my colleagues Maxim Berthe, Gautier Mahieu, Tao Xu, Justin Habinshuti, Corentin Durand for their help during the time at ISEN and IEMN.

I thanks to the members of physics group, with them I find a friendly working environment.

I also want to thank the Herodot network, which gave me many opportunities to take part in the scientific meetings, those are very useful for my PhD study and also for my future.

Finally, I want to thank my family my girl friend and other Vietnamese students in Lille, who always back me to pursue the PhD study.

© 2012 Tous droits réservés.

© 2012 Tous droits réservés.

Contents

Introduction

© 2012 Tous droits réservés.

© 2012 Tous droits réservés.

© 2012 Tous droits réservés.

© 2012 Tous droits réservés.

List of figure

© 2012 Tous droits réservés.

© 2012 Tous droits réservés.

© 2012 Tous droits réservés.

© 2012 Tous droits réservés.

http://doc.univ-lille1.fr

Introduction

Semiconductor nanocrystals (NCs) are defined as nanometer scale system where the charge carriers are confined in at least one dimension. They display unique and excellent properties for optoelectronic applications. However, the unexpected behaviors due to the trapping of charge carrier by the surface states can restrict their light emission or absorption in device–application. Several solutions have been suggested and the synthesis of core/shell NCs shows good promises to overcome the current limitations. In addition, the ability to engineer the band offsets and electronic states of heterostructure nanocrystals though their size, shape and composition makes them attractive for applications in optoelectronics devices. The combination of different semiconductors can improve the performance of a heteronanostructure, but it also produces unexpected properties that can limit their possibilities in applications. Hence, the understanding of their electronic properties is critical for devices manufacturing. By mean of scanning tunneling microscopy (STM) and spectroscopy (STS), this thesis deals with studying the electronic properties of semiconductor NCs consisting in the assembly of two different materials

This work starts with the definition of a semiconductor nanocrystal, and describes some of their applications. It also underlines the current limitations in device–application. The heterojunction structures are also presented and the electronic properties of nanocrystal in the presence of a shell layer are discussed. Experimentally, tunneling spectroscopy is a very useful method to carry out transport measurement of nanostructures. The basic idea of tunneling spectroscopy is based on Double Barrier Tunneling Junction (DBTJ) which is analyzed and applied in a particular case of a nanocrystal.

In Chapter 2, the theoretical background of scanning tunneling microscopy (STM) and spectroscopy (STS) techniques are explained. NCs are strongly affected by quantum confinement and exhibit discrete energy levels corresponding to quantized states in the valence band (VB) and the conduction band (CB), respectively. STS offers a unique advantage to probe the states in NCs via resonances of electrons from a STM tip with those energy levels. Additionally, the X–ray photoelectron spectroscopy (XPS) technique is also discussed because it will be exploited to study the quality of the shell in hetero–NCs.

Tunneling spectroscopic measurements on NCs require a very stable system to minimize the noise caused by mechanical vibrations, temperature broadening, trapping effects by defect,… for instance. Due to the lack of experience about STM and STS at the starting point, prior to my PhD study, we have considered a prototypical case: tunneling through a single orbital – the Si dangling bond. Our

© 2012 Tous droits réservés.

goal was to learn if we could charge it with two electrons. If we could design a method to reproducibility charge a single level, it could be very useful to study electronic transport through more complicated systems, such as a core/shell NC. By performing tunneling spectroscopic measurement, the transition from shell–tunneling to shell–filling regime with the feedback control loop on is observed for a single Si dangling bond. From the disappearance of the first excited state of the neutral DB and the emergence of a new state in the conduction band , the injection of the second electron into the DB state while it is already occupied by another electron is demonstrated. From the energy difference between the ground state of the DB and the state corresponding to the injection of the second electron, we have been able o measure the Coulomb energy of a single orbital.

In Chapter 4, colloidal PbSe/CdSe core/shell NCs deposited on a gold substrate have been investigated by mean of scanning tunneling spectroscopy at low temperatures and X–ray photoelectron spectroscopy. STM image reveals high close packed monolayers of PbSe/CdSe NCs at long range distance. By locating the tip above an individual NC, it is possible to perform spectroscopic measurements to get information of quantized energy level of the PbSe core in respect to an additional shell. By comparing to the case of PbSe core NC only, the zero–conductance gap of core/shell NC is found to be larger than the case of just only PbSe NC. Such increase of the zero–conductance gap is explained by analyzing the position of the electronic resonances as a function of the tip–NC distance. We demonstrate that the same type of carriers tunnel on both side of the zero–conductance gap for the majority of the NCs allowing to measure the charging energy. Additionally, photoemission spectroscopy experiments reveal the existence of partial CdSe shell which accounts for the fluctuations seen among the spectra.

Chapter 5 describes the study of CdSe/CdS Dot–in–Rod NCs. STS measurements performed a this Dot–in–Rod Nanocrystals allow to determine the position of the CdSe core concerning to the position of the onset on tunneling spectra acquired on different positions along a rod. However, from the experience gained in Figure 5.6, we show that the interpretation of the spectra is not so straightforward preventing the measurement of the band offset at the interface between the spherical core and the rod–like shell.

© 2012 Tous droits réservés.

Chapter 1

Basic concepts

1.1. Semiconductor Nanocrystals (NCs)

1.1.1. What is a semiconductor nanocrystal?

The field of nanostructure physics has been exponentially developed in recent years, and much of theoretical insights have been achieved hand in hand with progress in experimental techniques and possibilities in applications. Additionally, modern semiconductor processing techniques made it possible to artificially create the quantum confinement of a few electrons [1]. Such kind of man–made semiconductor structures are called semiconductor Nanocrystals (or NCs). Generally, a nanocrystal is classified as a single crystalline nanomaterial with at least one dimension smaller than 100 nm [2]. NCs get huge technological interest since their electrical and optical properties show strong size dependence and therefore are controllable through delicate manufacturing processes.

Semiconductor NCs with the size in the range of around 10 nm are considered as Quantum dots (QDs) (as seen in Figure 1.1). Specially, a semiconductor quantum dot (QD) is a portion of matter whose excitons are confined in all three spatial dimensions. A QD contains a few hundred to a few thousand atoms and its properties can be controlled not only by the type of material, but also by its size, shape and topology [3]. QDs experience quantum–size effect and display standard atomic physics properties with adjustable quantized energy spectra through their sizes and shapes [4]. The effects of confinement have been revealed experimentally since 1920's when the absorption and luminescence color toward longer wavelengths with colloids CdS was observed [5]. In 1960's, differences in absorption spectra between semiconductor particles and the corresponding macroscopic materials were also reported [6, 7, 8]. Theoretical approach for studying the effect of the size on the electronic structure explored in 1980's resulting in the understanding of the properties of nanocrystals in term of quantum confinement [9, 10, 11], and the term “quantum dot” was coined by M. Reed et. al. in 1988 [12].

© 2012 Tous droits réservés.

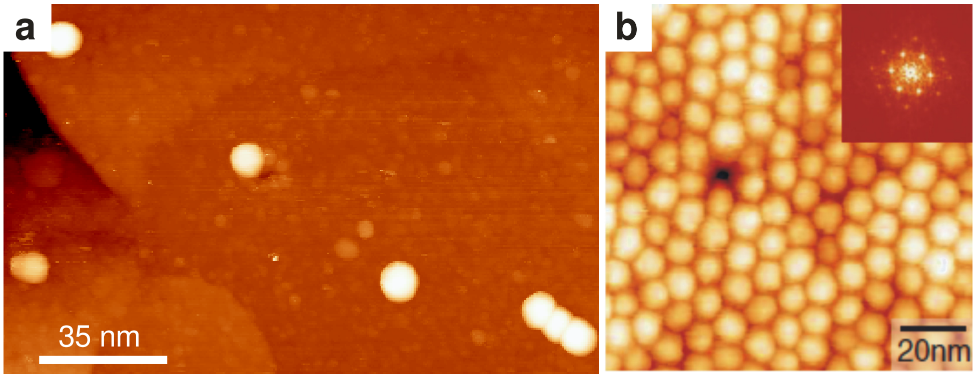

Figure 1.1: Large scale STM image of (a) 5.3 [13] *nm and (b) 7.3 nm* [14] *PbSe QDs covalently bound to the gold substrate.*

1.1.2. Applications of semiconductor NCs

With the strong confinement of electrons, holes and excitons inside, NCs have discrete energy levels and a tunable energy gap (the separation between Highest Occupied Molecular Orbital (HOMO) and Lowest Unoccupied Molecular Orbital (LUMO)) that is strongly size–dependence. Experimental results show that NCs with only a few nanometers in diameter are about ten times brighter than the best organic dyes and can be prepared in many different sharply defined colors [15]. Based on those significant properties, semiconductor NCs have been studied as promise materials in various electronic applications, especially, in the field if optoelectronics.

Quantum dot–based Photovoltaic devices: Since 1991, photovoltaic cells using TiO_2 films had been investigated and found to exhibit efficiency of converting incident light energy to electrical energy, and to be incredibly encouraging because of low–cost materials [16]. In 2001, a single–nanocrystal architecture in which an array of single particles between electrodes, corresponding to a separation of ~1 exciton diffusion length, was proposed to enhance the device efficiency [17]. Although the research is still developing, future QDs–based photovoltaic cells may offer advantages likes: more flexibility, lower costs, clean power generation, and higher efficiency.

Light emitting devices: There are some interests of using QDs as light–emitting diodes (LED) to make displays and other light sources, [QDs–LED, QDs–WLED (White LED)]. The emission color of QDs can be tuned from the visible throughout the infrared spectrum [18]. The development of QDs for use in LED in Liquid Crystal Display (LCD) television has been done and got significant success [19]. Much effort is carrying now in order to enhance the sufficient stability of QDs under prolonged radiation, which can be used to emit visible or near infrared light of any wavelength being excited by light with shorter wave length.

© 2012 Tous droits réservés.

Photodetector devices: Quantum dot photodetectors (QDPs) can be fabricated either by solution–processing [20] or from conventional single–crystalline semiconductors [21]. The second method allows to create QDPs by integrating QDs with flexible organic electronics. Solution–processed QDPs can be readily integrated with a variety of substrates and also attached on top of other integrated circuits.

Recently, the application of quantum dot in **Quantum computing** has attracted scientists worldwide. By applying a small voltage, there will be a flow of electrons through the quantum dot that can be controlled. So, it is possible to measure precisely the charge and even the spin. With several entangled QDs, or qubits (quantum bits), plus a suitable way of performing operations, quantum calculations and computers would be available.

1.1.3. Current limitations in application of core NCs

Despite of huge interest in application, NCs–based devices still suffer from unexpected behaviors that can limit their efficiency known as "blinking" effects. The distribution of local defects and interface states leads to the random turning on and off of NCs [22, 23]. Additionally, there is also the Auger recombination where energy of one excition is nonradiatively transferred to another carrier [24]. This process was reported to happen on subnanosecond time scales and reduce the optical gain lifetime [25]. It also limits the available time to extract multiple excitons generated via carrier multiplication and limit the LED brightness due to the build–up of charged NCs [26], [27].

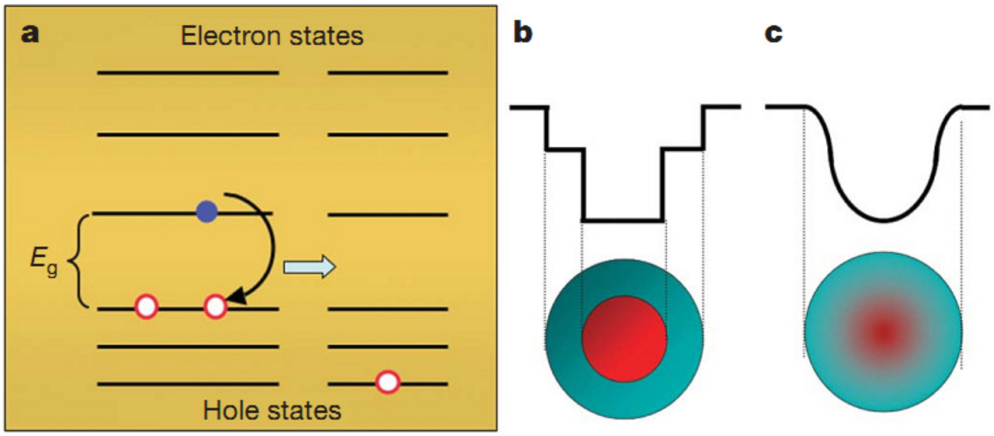

*Figure 1.2: Non–radiative Auger–like recombination and potential energy functions of Nanocrystals. (**a**) Diagram of an Auger process. E_g corresponds to the nanocrystal energy gap. An electron (filled blue circle) non–radiatively recombines with a hole (red circle), producing an electronically excited hole. (**b**) The potential energy function presents a series of steps for traditional nanocrystals. The undefined slope at the boundary between unlike materials results in an uncertainty in momentum. (**c**) A gradually changing potential energy function exists for non–blinking CdZnSe/ZnSe nanocrystals [28].*

© 2012 Tous droits réservés.

In order to reduce the "blinking" effect and to improve the NCs–based devices, many efforts have been done and got new achievements. Surrounding NCs by a shell of another material may sweep out the effects of NCs surface defects and, hence, the associated trapping energy levels. The combination of two different semiconductors together is called a heterostructure or a heterojunction. Sizing down this heterostructure to nano scale gives rise to a heteronanocrystal, such as: core/shell NCs. Wang et al. report the continuous non–blinking photoluminescence by covering the CdZnSe NCs with a layer of ZnSe creating a gradually changing potential energy function (as seen in Figure 1.2) [28]. In another work, a significant suppression of Auger decay rates was found in the structure consisting of a small CdSe core and a thick CdS shell. Consequently, an optical amplification with an extraordinarily large bandwith and a record low excitation thresholds are achieved [29].

1.2. Semiconductor heterojunction structure

1.2.1. Heterojunction

A heterojunction is the interface that occurs between two different crystalline semiconductors. These semiconducting materials have unequal band gaps as opposed to a homojunction. The combination of multiple heterojunctions together in a device is called a "heterostructure" although the two terms are commonly interchangeable. The advantage of engineering the electronic energy bands makes heterojunction materials useable in many solid state device applications, including semiconductor lasers, solar cells, transistors (or "heterotransistors")…

Based on the position of band offsets, semiconductor interfaces can be divided into three different categories: Type–I (straddling gap), Type–II (staggered gap), and Type–III (broken gap) (see Figure 1.3).

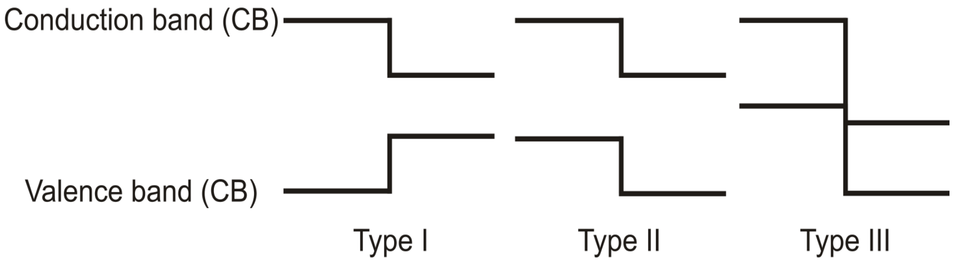

Figure 1.3: The three types of semiconductor heterojunctions depending on band alignment.

The relevant physical parameters for the determination of the band offset include: band gap, electron affinity and work function (as presented in Figure 1.4), which are defined as:

© 2012 Tous droits réservés.

- The difference between CB (Conduction Band) and VB (Valence Band), or band gap, varies from hundreds of meV for a semiconductor to over 4 eV for an insulator.

- The work function of a material is the energy difference between the Fermi energy (chemical equilibrium energy) and the vacuum level (where electron removal occurs).

- Electron affinity of each material is the energy difference between the conduction band level and the vacuum level.

A simple method to calculate the band offsets for an ideal heterojunction is to use Anderson's rule, as drawn out in Figure 1.4. Assuming that the conduction band offsets, ΔE_C, depends only on the electron affinity, χ, difference between the two semiconductors labeled 1 and 2, we have:

$$\Delta E_C = \chi_1 - \chi_2 = \Delta\chi \tag{1.1}$$

where χ is the electron affinity.

The change in band gap is:

$$\Delta E_G = E_{G2} - E_{G1} \tag{1.2}$$

Then the valence band offset, ΔE_V, is given by:

$$\Delta E_V = \Delta E_G - \Delta\chi \tag{1.3}$$

Both equations (1.1) and (1.3) are valid only if the potential steps caused by atomic dipoles at the semiconductor surfaces and the heterostructure interfaces can be neglected. When two materials are brought together and allowed to reach chemical/thermal equilibrium, the Fermi level in each material aligns and is constant throughout the system. To the extent that they are able, electrons in the materials leave some regions (depletion) and build up in others (accumulation) in order to find equilibrium. When this occurs a certain amount of band bending occurs near the interface. The band bending voltage is usually called the build–in potential and labeled V_{bi}. As a result:

$$\Delta E_C = E_{C_1} - E_{C_2} - eV_{bi} \tag{1.4}$$

where E_{C_1}, E_{C_2} are the relative positions of the edges of conduction bands of the two materials with respect to the Fermi level in the quasineutral region far away from the heterostructure.

© 2012 Tous droits réservés.

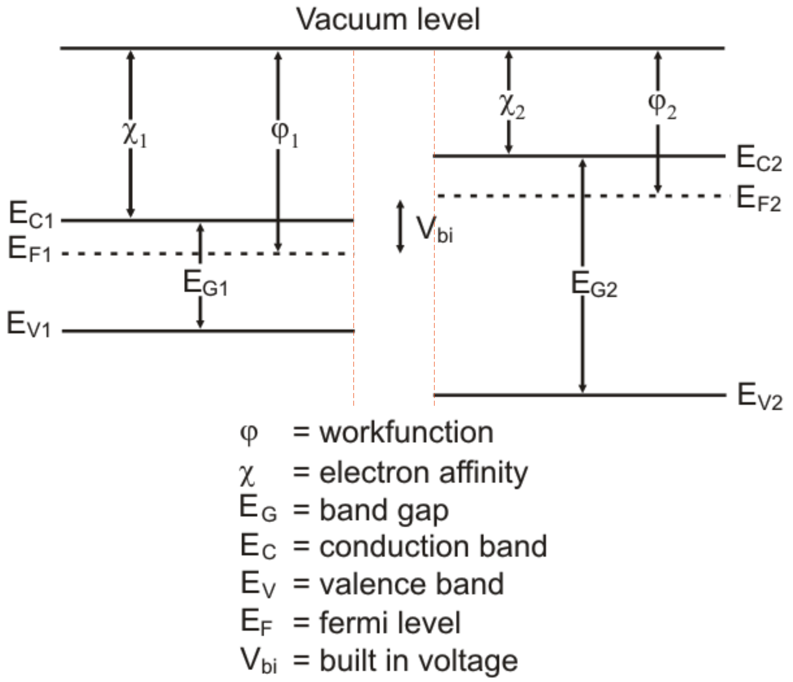

Figure 1.4: The important variables for heterojunction characterization and analysis are defined for two physically separated semiconductors (indicated by the red dashed curve).

1.2.2. Nanoscale heterojunction

The concept of heterostructure has been primarily explored in the context of Type−I core/shell NCs, in which, the shell of a wide band gap semiconductor is used to improve confinement of both an electron and a hole in the core made of a lower−gap material. With the presence of a shell layer, the interactions of core−localized e−h pairs (excitons) with surface traps decreases resulting in significant improvements of NC emission quantum yields [30, 31, 32]. Conversely, Type−II colloidal structures allow the controll of both single [33] and multiexciton [34] lifetimes. Also, the spatial separation between positive and negative charges produced in these structures can be beneficial for applications in photovoltaic technologies.

Recent reports showed that it is possible to use the same materials but change the type of band alignment, from Type−I to Type−II for example, by changing the size or thickness of the crystal involved. For example the band alignment of CdS/ZnSe core/shell NCs are found to vary from Type−I to Quasi Type−II and Type−II heterostrucre depending on the shell thickness (see Figure 1.10) [35]. Additionally, by decreasing the size of CdSe NCs grown on TiO_2, the electrons are found to be transferred faster from the higher CdSe conduction band into TiO_2 [36].

© 2012 Tous droits réservés.

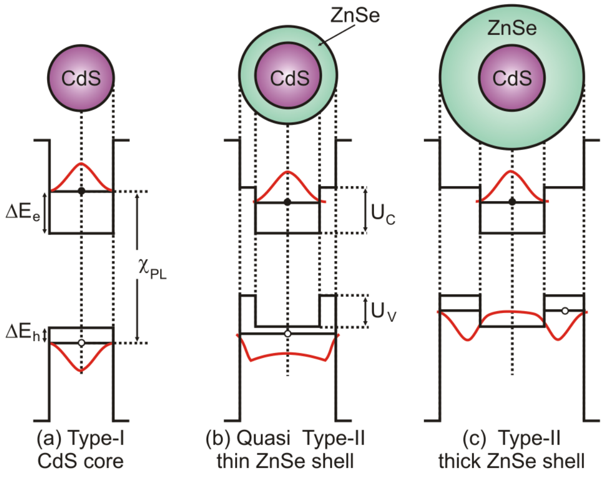

(a) Type-I
CdS core

(b) Quasi Type-II
thin ZnSe shell

(c) Type-II
thick ZnSe shell

Figure 1.5: Different localization regimes supported by CdS(core)/ZnSe(shell) NCs as a function of shell thickness, H. (a) Bare CdS-core NCs ($H = 0$) correspond to type–I localization, for which electron and hole wavefunctions (shown by red lines) have identical spatial distributions and, hence, the e–h overlap integral, Θ, is unity. (b) Core/shell NCs with thin shells ($0 < H < H_c$, $R > R_c$) correspond to the quasi type–II regime, in which the electron is localized in the core but the hole is delocalized over the entire NC volume. These structures produce partial separation between electrons and holes, which results in reduced values of Θ ($0.7 < \Theta < 1$). (c) Hetero-NCs with thick shells ($H > H_c$, $R > R_c$) can produce the true type–II regime, for which electrons and holes are separated between the core and the shell. For these charge–separated states, the e–h overlap integral can approach zero (adapted from S. A. Ivanov et al.) [35].

1.3. Scanning Tunneling Spectroscopy study of semiconductor NCs

1.3.1. Double Barrier Tunneling Junction (DBTJ)

The study of Double Barrier Tunneling Junction (DBTJ) has been done in 1960s in Thin–Film Triodes [37] with the prospect to obtain a Negative Differential Resistance (NDR) effect which plays an important role in in high–speed semiconductor devices [38, 39], in molecular electronic devices [40]. NDR arises as a variation of the transmission coefficient through the junctions when the energy of the incident electron varies. To demonstrate this effect, a 1D (1 Dimensional) model can be used where a central quantum well is surrounded by two insulating barriers in contact with leads, as seen in Figure 1.6(a). The thickness of the barriers are d_2 and d_4 and the heights are Φ_1 and Φ_4 respectively.

For a simple barrier, the transmission depends exponentially on the product of Kd, here, d is the thickness of the barrier and $K = \sqrt{2m\left(\Phi_0 - E\right)/\hbar^2}$ is the wave vector inside the barrier region, m is the mass of an electron and $\hbar$ is the reduced Planck's constant, Φ_0 is height of the potential barrier and E is the energy of the electron.

© 2012 Tous droits réservés.

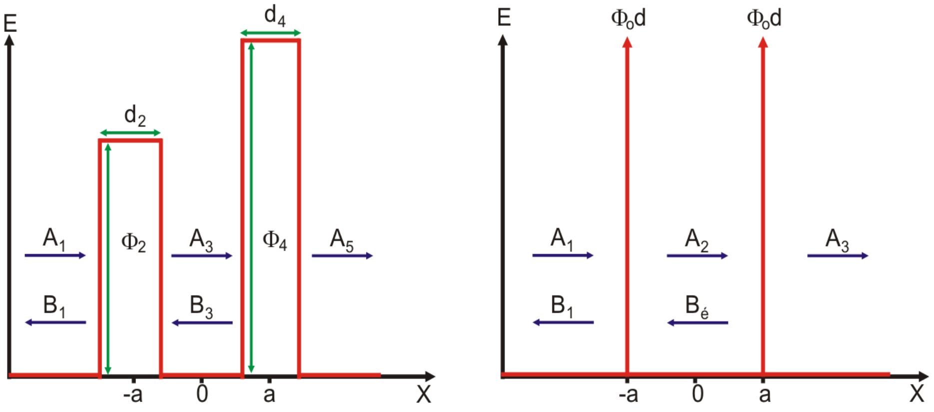

(a) (b)

Figure 1.6: Energy diagram of the DBTJ without (a) and with (b) the Krönig and Penney approximation. A_i and B_i are the incident wave amplitudes and the reflected amplitudes respectively.

In the case of double barrier junction, using the approximation of Krönig and Penney [41], the tunnel barriers are modeled with two Dirac–like functions (see Figure 1.6(b)). Where $d \to 0$ and $\Phi_i \to \infty$. The product and $\Phi_i d$ is assumed to be constant as: $\Phi_0 d$.

In order to calculate the transmission coefficient, we need to determine the wave function in three different regions. The general solution of the Shrödinger equation in each region is:

$$\begin{aligned} \varphi_1(x) &= A_1 e^{ikx} + B_1 e^{-ikx} \\ \varphi_2(x) &= A_2 e^{ikx} + B_2 e^{-ikx} \\ \varphi_3(x) &= A_3 e^{ikx} \end{aligned} \tag{1.5}$$

with $k = \sqrt{\frac{2m}{\hbar^2} E}$.

The continuity of the wave functions requires in those infinitely thin barriers:

- φ is continuous in $x_0 = -a$ and $x_0 = a$:

$$\varphi(x_{0+}) = \varphi(x_{0-}) \tag{1.6}$$

- $\frac{\partial \varphi}{\partial x}$ is discontinuous in $x_0 = -a$ and $x_0 = a$:

© 2012 Tous droits réservés.

$$\frac{\partial\varphi}{\partial x}(x_{0+})-\frac{\partial\varphi}{\partial x}(x_{0-})=\frac{2m\Phi_0 d}{\hbar^2}\varphi(x_0) \tag{1.7}$$

The equation (1.7) can be proved by integration of the Shrödinger equation:

$$\frac{-\hbar^2}{2m}\frac{\partial^2\psi}{\partial x^2}+\Phi_0\psi=E\psi \tag{1.8}$$

Integrating (1.8) between $a-d/2$ and $a+d/2$ yields:

$$\frac{-\hbar^2}{2m}\int_{a-d/2}^{a+d/2}\frac{\partial^2\psi}{\partial x^2}dx+\int_{a-d/2}^{a+d/2}\Phi_0\psi dx=E\int_{a-d/2}^{a+d/2}\psi dx \tag{1.9}$$

when $d\to 0$ then $\psi \sim constant$ and $\psi(a-d/2)=\psi(a+d/2)$, so:

$$\left(\left.\frac{\partial\psi}{\partial x}\right|_{a+d/2}-\left.\frac{\partial\psi}{\partial x}\right|_{a-d/2}\right)=(\Phi_0-E)\frac{2md}{\hbar^2}\psi(a) \tag{1.10}$$

here $\Phi_0 \gg E$ when $d\to 0$. The combination the solutions of the equations in (1.5) with the continuous and discontinuous conditions in (1.6) and (1.7) reveal the below system as matching conditions. At the boundaries, the continuity of the wave functions and the discontinuity of the first derivative yield:

$$\begin{gathered}
\alpha\frac{B_1}{A_1}-\frac{1}{\alpha}\frac{A_2}{A_1}-\alpha\frac{B_2}{A_1}=-\frac{1}{\alpha}\\
\alpha\frac{A_2}{A_1}+\frac{1}{\alpha}\frac{B_2}{A_1}-\alpha\frac{A_3}{A_1}=0\\
\alpha(1+M)\frac{B_1}{A_1}+\frac{1}{\alpha}\frac{A_2}{A_1}-\alpha\frac{B_2}{A_1}=\frac{1}{\alpha}(1-M)\\
-\alpha\frac{A_2}{A_1}+\frac{1}{\alpha}\frac{B_2}{A_1}+\alpha(1+M)\frac{A_3}{A_1}=0
\end{gathered} \tag{1.11}$$

where $M=\frac{2im\Phi_0 d}{\hbar^2 k}$ and $\alpha=e^{ika}$.

The ratio between the incident wave amplitudes A_1 and A_3 (the amount of the out going flow of electrons over the incident flow) corresponds to the transmission coefficient $T(E)$:

© 2012 Tous droits réservés.

$$T\left(E\right)=\frac{\left|A_3e^{ikx}\right|^2}{\left|A_1e^{ikx}\right|^2}=\left|\frac{A_3}{A_1}\right|^2 \tag{1.12}$$

Extracting the ratio A_3/A_1 from the solution of (1.11) gives:

$$\frac{A_3}{A_1}=\frac{4}{\left(M+2\right)^2-\alpha^4M^2} \tag{1.13}$$

Finally:

$$T\left(E\right)=\frac{1}{1+\frac{\left|M\right|^2}{4}\left(2\cos\left(2ka\right)+\left|M\right|\sin\left(2ka\right)\right)^2} \tag{1.14}$$

At $tan\left(2ka\right)=-\frac{2}{M}$, a sharp resonance in (1.14) can be observed. In fact, at this energy position, the transmission coefficient even reaches unity regardless to the thickness of the barrier, but the condition $d \ll a$ must be satisfied, corresponding to perfect transparency. Such a model is appropriate to describe the transport through a semiconductor nanocrystal which is isolated from surrounding electrodes by two tunneling barriers (see Figure 1.7), the electrodes being the tip and a metallic sample in a STM configuration.

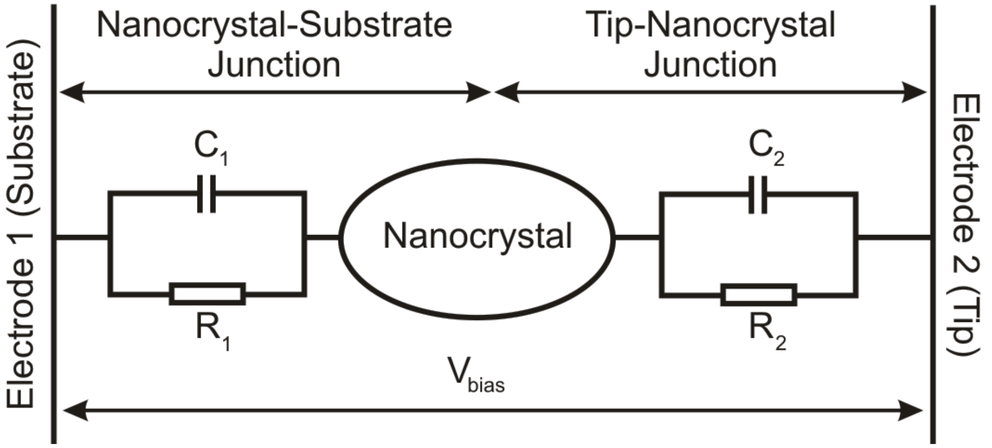

Figure 1.7: Schematic of a single nanocrystal in a DBTJ, where C_1 *and* C_2 *stand for the capacitances of the tunneling barriers and* R_1 *and* R_2 *are equivalent resistances related to the probability transmissions across both tunneling junctions.*

© 2012 Tous droits réservés.

1.3.2. Tunneling spectroscopy of semiconductor NCs

Due to the small size and quantum confinement effects in semiconductor quantum dots, their electronic wave functions were predicted to display atomic–like symmetries and discrete energy level structures [42, 43]. Both theoretical and experimental works have been successful to identify and interpret the tunneling process of charge carriers through the available quantized states inside the NCs [44, 45, 46].

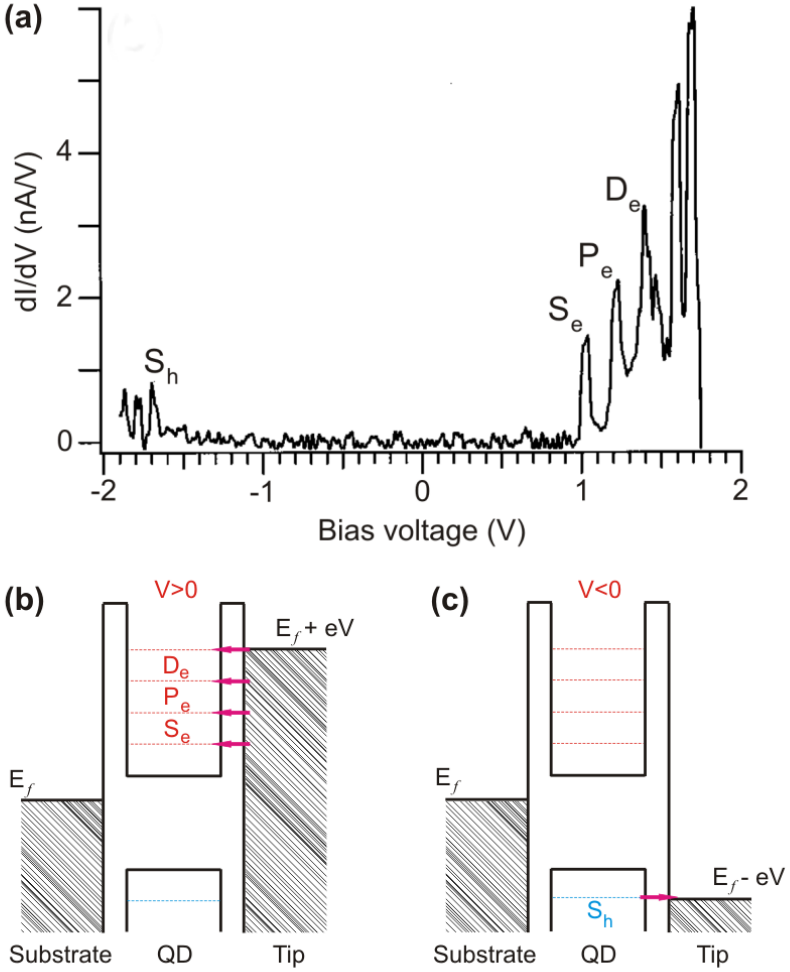

Figure 1.8: (a) Shell–tunneling spectrum of a 4.3 nm CdSe quantum dot at 4.2 K, I_{set} = 5 pA and V_{bias} = 1.4 eV. Five peaks in the range of bias voltage V > 1 eV correspond to single particle states. The onsets at positive and negative bias correspond to LUMO (S_e) and HOMO (S_h) respectively. The zero–conductivity gap corresponds to the quasi–particle gap of the QD [45]. (b) Schematic illustration of shell–tunneling spectroscopy at positive bias, electrons tunnel one by one from the tip through the resonant states of the QD. (c) Schematic illustration of shell–tunneling spectroscopy at negative bias, hole injected from the tip to the QD (adapted from E. P. A. M Bakkers et al.) [45].

© 2012 Tous droits réservés.

The discrete electron states appear as resonances when the NCs are probed in a double barrier tunneling junction configuration. A major step in this field was achieved with tunneling spectroscopy experiments on InAs nanocrystals that reveal rich features caused by the interplay between quantum confinement and single–charge effects [44]. The later studies also show the same behaviors in chalcogen NCs [45, 47]. As presented in Figure 1.8(a) the tunneling spectrum of a 4.3 nm CdSe nanocrystal contains a zero–conductivity gap around zero bias and is followed by a series of peaks at both positive and negative bias. The single peaks correspond to single particle tunneling of electrons (S_e, P_e, D_e) and holes (S_h) from the tip to the resonant states in the NC at positive and negative bias respectively (see Figure 1.8(b) and (c)). The conductance curve in Figure 1.8(a), then, is attributed to a *shell–tunneling* spectrum. In this tunneling regime, electron is injected one by one to the discrete states in the NC whenever the Fermi level of the tip reach a state (see Figure 1.8(b)) [45].

The shell–tunneling regime is normally observed with low current set point when the tip–NC distance is quite large (with I_{set} = 5 pA, the estimated tip–NC distance is around 1.4 nm) [45]. In this case, the zero–conductivity region, also called as the apparent band gap, corresponds to:

$$\eta e\Delta V = \varepsilon_1^e - \varepsilon_1^h + 2\Sigma \qquad (1.15)$$

where $\eta = \frac{C_1}{C_1 + C_2}$ is the drop voltage across the two junction as seen in Figure 1.7, ΔV is the apparent band gap, ε_1^e and ε_1^h are the conduction band ground state (or LUMO: lowest unoccupied "molecular" orbital) and valence band ground state (or HUMO: highest occupied "molecular" orbital) of the NC, and $\Sigma = \frac{1}{2}\frac{e^2}{C_1 + C_2}$ is the polarization energy.

At larger current set point (shorter tip–NC distance), the possibility for charging the NC will increase resulting in the shell–filling regime where more than one charge carrier reside in the NC at the same time, see in Figure 1.9. The STM image of an isolated InAs with an $I - V$ curve acquired on the same dot through a DBTJ created by the tip–InAs NC–substrate system (see Figure 1.9(a)). The $I - V$ curve contains a region of suppressed tunneling current around the zero bias which is followed by a series of steps at both negative and positive voltages. Whereas, a series of discrete single–electron tunneling peaks is clearly observed in tunneling conductance spectrum (Figure 1.6(b)), and the separations are determined by both single–electron charging energy and the discrete level spacings [44]. At positive bias, the separation of the first two peaks is attributed to the

© 2012 Tous droits réservés.

charging energy E_C (this energy will be named as U in the following parts) indicating the tunneling of the second electron into the same state in CB.

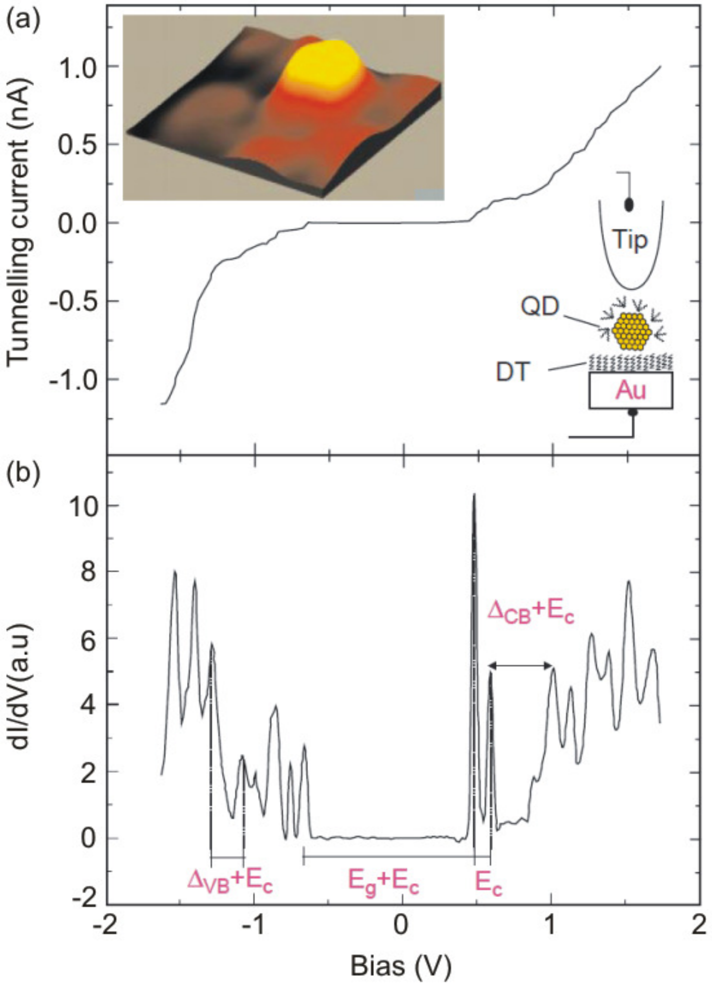

Figure 1.9: STM image and STS spectrum of a single InAs nanocrystal 32Å in radius, acquired at 4.2 K. The nanocrystal quantum dots (QD) are linked to the gold substrate by hexane dithiol molecules (DT), as shown schematically in the right inset. Left inset, a 10×10 nm STM topographic image, showing the nanocrystal. For measuring the I–V characteristics, the STM tip was positioned above the QD, thus realizing a double–barrier tunnel junction configuration. (a), The tunnelling I–V characteristic, exhibiting single–electron tunneling effects. (b) The tunnelling conductance spectrum, dI/dV versus V, obtained by numerical differentiation of the I–V curve (a.u., arbitrary units). The arrows depict the main energy separations: Ec is the single–electron charging energy, E_g *is the nanocrystal bandgap, and* Δ_{VB} *and* Δ_{CB} *are the spacing between levels in the valence and conduction bands, respectively (adapted from U. Banin at el.)* [44].

In the shell–filling regime, the identification of the peaks may be more complex than the case of shell–tunneling regime and it is interesting to consider

© 2012 Tous droits réservés.

the work of Averin et al. [48] and Niquet et al. [46] to correctly assign the peak observed in the tunneling spectra. Indeed, when the probability transmission across both barriers becomes comparable, the same type of charge carrier is able to tunnel on both sides of zero–conductivity region depending on the position of the Fermi level in the nanocrystals. Such situation also favors the charging of the NCs, where the charging energy is given by:

$$U = \frac{e^2}{C_1 + C_2} \tag{1.16}$$

© 2012 Tous droits réservés.

References

---

[1] S. M. Reimann, and M. Manninen, “*Electronic structure of quantum dots”*, Rev. Mod. Phys. **74**, 1283–1342 (2002).

[2] B. D. Fahlman, “*Material Chemistry*”, Springer: Mount Pleasant, MI. **1**, 282–283 (2007).

[3] D. J. Milliron, S. M. Hughes, Y. Cui, L. Manna, J. B. Li, L. W. Wang, A. P. Alivisatos, “*Colloidal nanocrystal heterostructures with linear and branched topology”*, Nature **430**, 190–195 (2004).

[4] B. Billaud, and T. T. Truong, “*Some theoretical results on semiconductor spherical quantum dots”*, Com. Mat. Sci. **49**, 322–325 (2010).

[5] G. Jaeckel, and Z. Tech, J. Phys. **6**, 301–325 (1926).

[6] C. R. Berry, “*Structure and Optical Absorption of AgI Microcrystals”*, Phys. Rev. **161**, 848 (1967).

[7] C. R. Berry, “*Effect of Crystal Surface on the Optical Absorption Edge of AgBr”*, Phys. Rev. **153**, 989 (1967).

[8] E. J. Meehan, and J. K. Miller, “*Complex refractive index of colloidal silver bromide in the near-ultraviolet*”, J. Phys. Chem. **72**, 1523–1529 (1968).

[9] A. I. Ekimov, and A. A. Onushchenko, “*Quantum size effect in three-dimensional microscopic semiconductor crystals*”, J. Exp. Theor. Phys. Lett. **34**, 345–349 (1981).

[10] L. E. Brus, “*A Simple Model for the Ionization Potential, Electron Affinity, and Aqueous Redox Potentials of Small Semiconductor Crystallites*”, J. Chem. Phys. **79**, 5566 (1983).

[11] L. E. Brus, “*Electron–Electron and Electron–Hole Interactions in Small Semiconductor Crystallites: The Size Dependence of the Lowest Excited Electronic State*”, J. Chem. Phys. **80**, 4403 (1984).

[12] M. A. Reed, J. N. Randsll, R. J. Aggarwal, R. J. Matyi, T. M. Moore, and A. E. Wetsel, “*Observation of discrete electronic states in a zero–dimensional semiconductor nanostructure*”, Phys. Rev. Lett. **60**, 535 (1988).

[13] P. Liljeroth, P. A. Z. Emmichoven, S. G. Hickey, H. Weller, B. Grandidier, G. Allan, and D. Vanmaekelbergh, “*Density of States Measured by Scanning–Tunneling Spectroscopy Sheds New Light on the Optical Transitions in PbSe Nanocrystals*”, Phys. Rev. Lett. **95**, 086801 (2005).

[14] P. Liljeroth, K. Overgaag, A. Urbieta, B. Grandidier, S. G. Hickey, and D. Vanmaekelberg, “*Variable Orbital Coupling in a Two–Dimensional Quantum–Dot Solid Probed on a Local Scale*”, Phys. Rev. Lett. **97**, 096803 (2006).

[15] T. Ha, “*How nanocrystals lost their blink*”, Nature **459**, 649–650 (2009).

[16] B. O’Regan, and M. Gratzel, “*A low–cost, high efficiency solar cell based on dye–sensitized colloidal* TiO_2”, Nature **353**, 737–740 (1991).

© 2012 Tous droits réservés.

http://doc.univ-lille1.fr

---

[17] J. S. Salafsky, "*A "channel" design using single semiconductor nanocrystals for efficient (opto)electronic devices films*", Sol. Stat. Elec. **45**, 53−58 (2001).

[18] "*Quantum dots LED may be screen of choice for future electronics*", M. I. T. News Office December 18 (2002).

[19] T. H. Kim, K. S. Cho, E. K. Lee, S. J. Lee, J. Chae, J. W. Kim, D. H. Kim, J. Y. Kwon, G. Amaratunga, S. Y. Lee, B. L. Choi, Y. Kuk, J. M. Kim, and K. Kim, "*Full−colour quantum dot displays fabricated by transfer printing*", Nature Photonics **5**, 176−182 (2011).

[20] G. Konstantatos, and E. H. Sargent, "*Solution−Processed Quantum Dot Photodetectors*", Proceedding of the IEEE **97** (10), 1666−1683 (2009).

[21] J. Vaillancourt, and X. J. Lu, "*High Operating Temperature (HOT) Middle Wave Infrared (MWIR) Quantum−Dot Photodetector*", Optics and Photonics Letters **4** (2), 1−5 (2011).

[22] M. Nirmal, B. O. Dabbousi, M. G. Bawendi, J. J. Macklin, J. K. Trautman, T. D. Harris, and L. E. Brus, "*Flourescence intermittency in single cadmium selenide nanocrystals*", Nature **383**, 802−804 (1996)

[23] M. Kuno, D. P. Fromm, H. F. Hammann, A. Gallagher, and D. J. Nesbitt, "*Nonexponential "bliking" kinetics of single CdSe quantum dots: A universal power low behavior*", J. Chem. Phys. **112**, 3117−3120 (2000).

[24] V. I. Klimov, A. A. Mikhailovsky, D. W. McBranch, C. A. Leatherdale, and M. G. Bawendi, "*Quantization of Multiparticle Auger Rates in Semiconductor Quantum Dots*", Science **287**, 1011−1013 (2000).

[25] V. I. Klimov, A. A. Mikhailovsky, S. Xu, AL Malko, J. A. Hollingsworth, C. A. Leatherdale, H. J. Eisler, and M. G. Bawendi, "*Optical Gain and Stimulated Emission in Nanocrystal Quantum Dots*", Science **13**, 314−317 (2000).

[26] A. J. Nozik, "*Quantum dot solar cells*", Physica E **14**, 115−120 (2002).

[27] P. O. Anikeeva, C. F. Madigan, J. E. Halpert, M. G. Bawendi, and V. Bulovic, "*Electronic and excitonic processes in light−emitting devices based on organic materials and colloidal quantum dots*", Phys. Rev. B **78**, 085434 (2008).

[28] X. Wang, X. Ren, K. Kahen, M. A. Hahn, M. Rajeswaran, S. Maccagnano−Zacher, J. Silcox, G. E. Cragg, A. L? Efros, and T. D. Krauss, "*Non−blinking semiconductor nanocrysttals*", Nature **459**, 686−689 (2009).

[29] F. Garcia−Santamaria, Y. Chen, J. Vela, R. D. Schaller, J. A. Hollingsworth, and V. I. Klimow, "*Suppressed Auger Recombination in "Gian" Nanocrystals Boots Optical Gain Performance*", Nano Lett. **9** (10), 3482−3488 (2009).

[30] A. M. Hines, and P. Guyot−Sionest, "*Synthesis and Characterization of Strongly Luminescing ZnS−Capped CdSe Nanocrystals*", J. Phys. Chem. **100**, 468−471 (1996).

[31] Y. W. Cao, and U. Banin, "*Synthesis and characterization of InAs/InP and InAs/CdSe core/shell nanocrystals*", Angew. Chem. Int. Ed. **38**, 3692−3694 (1999).

© 2012 Tous droits réservés.

---

[32] J. J. Li, Y. A. Wang, W. Z. Guo, J. C. Keay, T. D. Mishima, M. B. Johnson, X. G. Peng, "*Large−Scale Synthesis of Nearly Monodisperse CdSe/CdS core/shell Nanocrystals Using Air−Stable Reagents via Successive Ion Layer Adsorption and Reaction*", J. Am. Chem. Soc. **125**, 12567−12575 (2003).

[33] L. P. Balet, S. A. Ivanov, A. Piryatinski, M. Achermann, and V. I. Klimov, "*Inverted Core/Shell Nanocrystals Continuously Tunable between Type−I and Type−II Localization Regimes*", Nano Lett. **4**, 1485−1488 (2004).

[34] J. Nanda, S. A. Ivanov, H. Htoon, I. Bezel, A. Piryatinski, S. Tretiak, and V. I. Klimov, "*Absorption cross sections and Auger recombination lifetimes in inverted core−shell nanocrysrals: Implications for lasing performance*", J. Appl. Phys. **99**, 034309 (2006).

[35] S. A. Ivanov, A. Piryatinski, J. Nanda, S. Tretiak, K. R. Zavadi, W. O. Vallace, D. Werder, and V. I. Klimov, "*Type−II Core/Shell CdS/ZnSe Nanocrystals: Synthesis, Electronic Structures, and Spectroscopic Properties*", J. Am. Chem. Soc. **129**, 11708−11719 (2007).

[36] I. Robal, M. Kuno, and P. V. Kamat, "*Size−Dependent Electron Injection from Excited CdSe Quantum Dots into* TiO_2 Nanoparticles", J. Am. Chem. Soc. **129**, 4136–4137 (2007).

[37] R. H. Davis, and H. H. Hosack, "*Double Barrier in Thin−Film Triodes*", J. Appl. Phys. **34**, 864–866 (1963).

[38] S. Sze, "*Physics of Semiconductor Devices*", Wiley, New York (1981).

[39] L. L. Chang, E. E. Mendez, and C. Tejedor, "*Resonant Tunneling in Semiconductors*", Plenum, New York (1991).

[40] R. L. Carroll and C. B. Gorman, "*The Genesis of Molecular Electronics*", Angew. Chem., Int. Ed. **41**, 4378 (2002).

[41] R. L. Krönig, and W. G. Penney, "*Quantum Mechanics of Electrons in Crystal Lattices*", Proc. R. Soc. London. Ser. A. **130**, 499−513 (1931).

[42] D. J. Norris, A. Sacra, C. B. Murray, and M. G. Bawendi, "*Measurement of the size dependent hole spectrum in CdSe quantum dots*", Phys. Rev. Lett. **72**, 2612–2615 (1994).

[43] U. Banin, J. C. Lee, A. A. Guzelian, A. V. Kadavanich, A. P. Alivisatos, W. Jaskolski, G. W. Bryant, A. L. Efros, M. Rosen, "*Size dependent electronic level structure of InAs nanocrystal quantum dots: Test of multiband effective mass theory*", J. Chem. Phys. **109**, 2306–2309 (1998).

[44] U. Banin, Y. Cao, D. Katz, and O. Millo, "*Identification of atomic−like electronic states in indium arsenide nanocrystal quantum dots*", Nature **400**, 542–544 (1999).

[45] E. P. A. M. Bakkers, Z. Hens, A. Zunger, A. Franceschetti, L. P. Kouwenhoven, L. Gurevich, and D. Vanmaekelberg, "*Shell−Tunneling Spectroscopy of the Single−Particle Energy Levels of Insulating Quantum dots*", Nano Lett. **1**, 551−556 (2001).

[46] Y. M. Niquet, C. Delerue, M. Lannoo, and G. Allan, "*Single−particle tunneling in semiconductor quantum dots*", Phys. Rev. B **64**, 113306 (2001).

© 2012 Tous droits réservés.

---

[47] E. P. A. M. Bakkers, and D. Vanmaekelbergh, "*Resonant electron tunneling through semiconducting nanocrystals in a symmetrical and an asymmetrical junction*", Phys. Rev. B **62**, 7743−7746 (2000).

[48] D. V. Averin, A. N. Korotkov, and K. K. Likharev, "*Theory of single−electron charging of quantum wells and dots*", Phys. Rev. B **42** (12), 6199−6211 (1991).

© 2012 Tous droits réservés.

Chapter 2

Scanning Tunneling Microscopy (STM) and Spectroscopy (STS)

2.1. Introduction

Imaging the surface of materials has always been a challenge to scientists worldwide. It was Erwin Müller [1] who obtained for the first time the atomically resolved images of metallic surface by using field ion microscopy. However, the major breakthrough in the field of microscopy was made in early 1980s with the invention of Scanning Tunneling Microscopy (STM) by Binnig and Rohrer [2] who were awarded the Nobel Prize latter, in 1986.

The principle of the STM is remarkably simple and it can be compared with the way an old−fashioned record player works. Just like in a record player, the instrument uses a sharp needle, referred to as the ‘tip’, brought so close to interrogate the morphology of the sample surface, as presented in Figure 2.1. In the standard imaging process, the tip scans over the surface and the tunneling current is kept constant by a feedback system via adjusting the tip−sample distance z. This frequently used mode of imaging is known as the constant current mode. The z−piezo regulation voltage is recorded during scanning and is presented by a color−scale image, the bright areas correspond to the protrusions on the surface and the darker ones to depressions. For very flat surfaces and small scanning areas, it is possible to measure the tunneling current during scanning while keeping the height constant. This mode refers to the constant height topography.

For the STM, a good resolution is considered to be 0.1 nm laterally and 0.01 nm in depth [3]. With such a precision, individual atoms within materials are routinely imaged and manipulated. The STM can be used in a variety of environment like ultra high vacuum, liquids, or gas ambient, and in the range of temperatures from near zero Kelvin to a few hundred degrees Celsius [4, 5, 6, 7]. But, STM can be a challenging technique, as it requires extremely clean and stable surfaces, sharp tips, excellent vibration control, and sophisticated electronics for obtaining high resolution images and stable and very flat signal.

© 2012 Tous droits réservés.

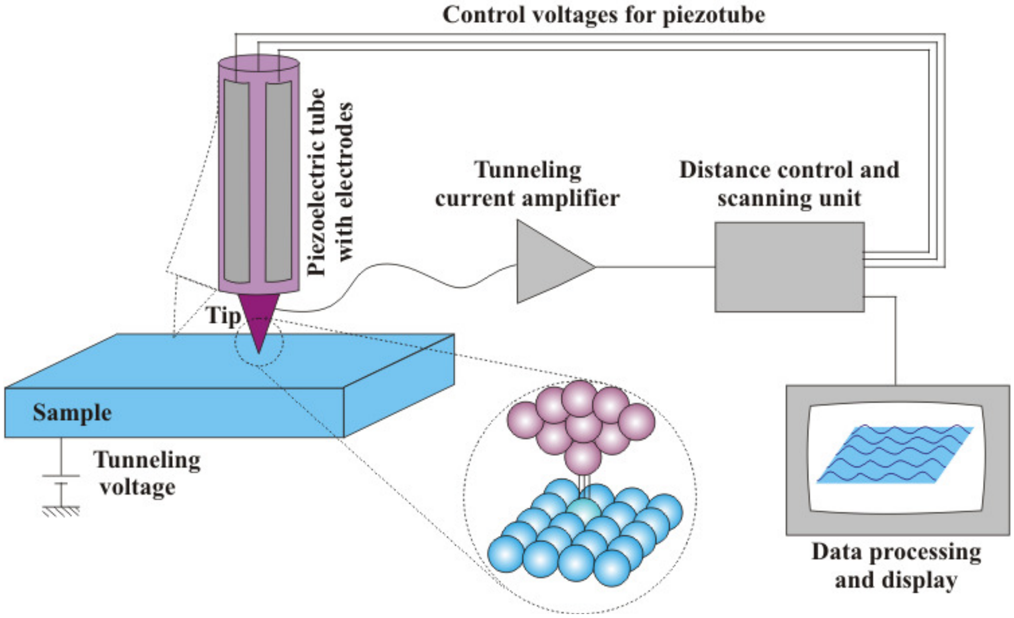

Figure 2.1: A simple schematic view of the STM.

Having been recognized as one of the most powerful technique to observe the surface reconstruction at nano-scale, many other scanning probe microscopy techniques have been developed based upon the principle of STM: photon scanning microscopy (PSTM) [3]; scanning tunneling potentiometry (STP) [3]; spin polarized scanning tunneling microscopy (SPSTM), which uses a ferromagnetic tip to tunnel spin-polarized electrons into a magnetic sample [8] and atomic force microscopy (AFM), in which the force caused by interaction between the tip and the sample surface is measured. With STM, Eigler et al. showed the possibility of manipulating individual atoms and molecules [9, 10] for example by building the islands of CO molecules. Also, the possibility for investigating chemical reactions with STM was reported by making and breaking individual chemical bonds between a metal atom Fe and CO molecules [11].

2.2. Scanning tunneling microscopy

2.2.1. Principle of operation

The operation of STM lies on the physics of tunneling that is linked to quantum mechanics. Classically, when objects hit an impenetrable barrier it will not pass through. In contrast, objects with very small size, electrons for example, have wavelike characteristics which permit such an event, referred to as tunneling. Assuming 1–dimensional (1D) case in the presence of a potential $U(z)$, the energy levels $\psi(z)$ of the electrons are given by the solutions of Schrödinger's equation:

© 2012 Tous droits réservés.

$$-\frac{\hbar^2}{2m}\frac{\partial^2\psi(z)}{\partial z^2}+U(z)\psi(z)=E\psi(z) \tag{2.1}$$

where $\hbar=\dfrac{h}{2\pi}$ is the Planck's constant, z is the vertical position of the tip above the surface, and m is the mass of an electron [12]. If an electron of energy E is incident upon an energy barrier of height $U(z)$ with $E>U(z)$, the electron wave function is a traveling wave solution:

$$\psi(x)=\psi(0)e^{\pm ikz} \tag{2.2}$$

with

$$k=\frac{\sqrt{2m\left(E-U(z)\right)}}{\hbar} \tag{2.3}$$

and $\psi(0)$ is the wave–function amplitude. When $E<U(z)$, the wave functions correspond to decaying waves:

$$\psi(z)=\psi(0)e^{\pm\kappa z} \tag{2.4}$$

where:

$$\kappa=\frac{\sqrt{2m\left(U(z)-E\right)}}{\hbar} \tag{2.5}$$

quantifies the decay (or decay constant) of the wave inside the barrier.

The solution $\psi(z)=\psi(0)e^{-\kappa z}$ describes a state of the electron decaying in the $+z$ direction and the other solution, $\psi(z)=\psi(0)e^{+\kappa z}$ describes the electron state decaying in the $-z$ direction [12].

Using an elementary model, the potential barrier of a metal–vacuum–metal junction is related to the work function of the electrodes, as shown in Figure 2.2. The *work function* Φ of a metal surface is defined as the minimum energy required to remove an electron from the host material to the vacuum level. Generally, the work function depends on both the material and the crystallographic orientation of the surface. If the thermal excitation is neglected, the *Fermi level* is the upper limit of the occupied states in a metal, taking the vacuum level as the reference point of energy, $E_f=-\Phi$ and the work function of the tip and the sample is considered to be equal. The electron at the Fermi level in the sample can tunnel into the tip and *vice versa* [12].

© 2012 Tous droits réservés.

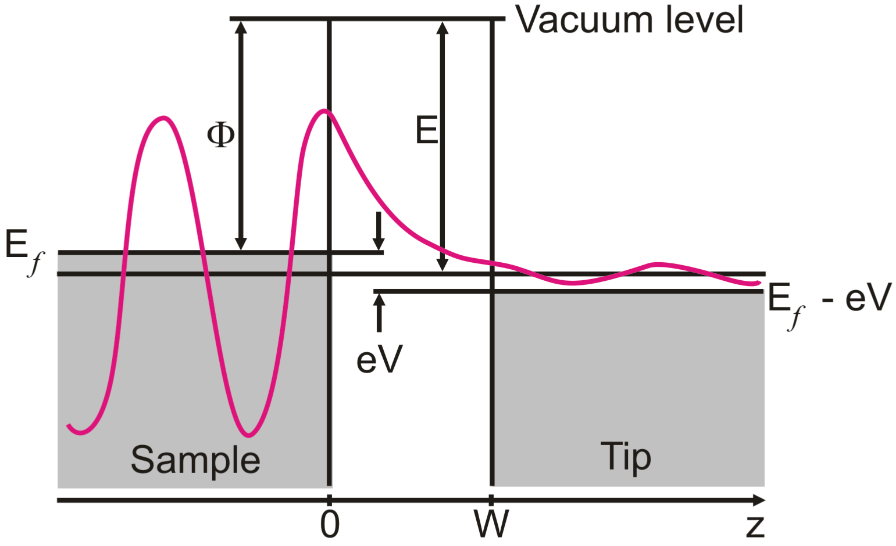

Figure 2.2: A one-dimensional metal-vacuum-metal tunneling junction. The sample (left) and the tip (right) are modeled as semi-infinite pieces of free electron metal [12]*.*

However, tunneling requires the empty state level of the same energy for electron to tunnel into the other side of the barrier. Due to this restriction, the tunneling current can be related to the density of available or filled states in the sample depending on the sign of the sample bias [12]. The system of tip–sample in tunneling contact in equilibrium is shown in Figure 2.3 for different polarities of the applied voltages on the sample and. The tunneling current is zero in equilibrium, Figure 2.3(a), ($V = 0$). When there is a bias voltage, the sample Fermi levels is shifted by eV. At positive voltage V, Figure 2.3(b), electrons in the range of energies from E_f to $E_f + eV$ can tunnel from the unoccupied states of the tip into the available states of the sample. Inversely at negative bias V, the electrons from the sample with energies in between $E_f - eV$ to E_f can tunnel into unoccupied states of the tip, see Figure 2.3(c).

Assuming the barrier width is W, the probability P, for that an electron at position $z = 0$ (left edge of the barrier) could be found at the position $z = W$ (right edge of the barrier or at the tip surface) is proportional to the square of the decaying wave function as [12]:

$$P \propto \left|\psi_n(0)\right|^2 e^{-2\kappa W} \tag{2.6}$$

here, $\psi_n(0)$ is the value of the nth sample state at the sample surface, and:

$$\kappa = \frac{\sqrt{2m\Phi}}{\hbar} \tag{2.7}$$

© 2012 Tous droits réservés.

is the decay constant of a sample state near the Fermi level in the barrier region. Accepting eV as the unit of the work function, and Å^{-1} as the unit of the decay constant, the Equation (2.6) becomes [12]:

$$\kappa = 0.51\sqrt{\Phi(eV)}\text{Å}^{-1} \tag{2.8}$$

For a typical metal, with $\Phi = 4.5eV$, the decay constant is of the order 1 Å^{-1}.

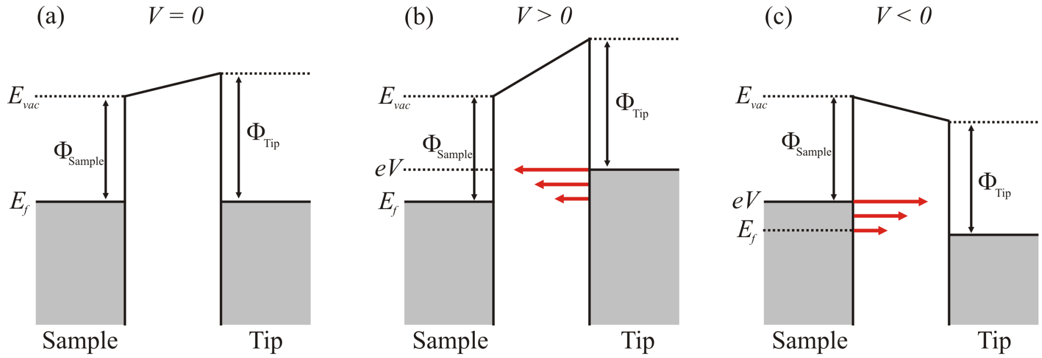

Figure 2.3: A tunneling junction consisting of a tip and a sample: (a) $V = 0$, equilibrium state, no tunneling current, (b) $V > 0$, positive sample bias, tunneling current from tip to sample, (c) $V < 0$, negative sample bias, tunneling current from sample to tip. Here, E_{vac} is the energy of vacuum level; E_f is the Fermi level of both the tip and the sample; Φ_{Tip} and Φ_{Sample} are the work functions of the tip and the sample respectively, and $\Phi_{Tip} = \Phi_{Sample} = \Phi$.

2.2.2. Contribution of the density of state

During the scanning process, the density of states in the tip is considered constant. Then the tunneling current is directly proportional to the number of states on the sample surface and is given by the sum of the probability transmission over all the available states positioned between E_f and $E_f + eV$ (see Figure 2.3 (b)):

$$I \propto \sum_{E_f}^{E_f+eV} |\psi_n(0)|^2 e^{-2\kappa W} \tag{2.9}$$

If the applied voltage V is small enough that the density of electronic states does not vary significantly, then the sum in (2.9) can be written in term of the *local density of state* (LDOS) at the Fermi level. At a certain location z and energy E in a small interval ε, the LDOS $\rho_s(z,E)$ of the sample is given by [12]:

$$\rho_s(z,E) = \frac{1}{\varepsilon}\sum_{E}^{E+\varepsilon} |\psi_n(z)|^2 \tag{2.10}$$

© 2012 Tous droits réservés.

The LDOS is the number of electrons per unit volume per unit energy at a certain point in space and at a given energy. It is interesting to note here that the probability density for a specific state, $|\psi_n|^2$, depends on the normalization condition (its integral in the whole space should be 1). Whenever the volume increases, the probability density $|\psi_n|^2$ of a single state decreases, but the number of states per unit energy increases, hence, the LDOS remains constant.

By replacing ε by eV and E by E_f and taking $z=0$, the tunnel current can be written in term of the sample's LDOS as:

$$\begin{aligned} I &\propto eV\rho_s\left(0,E_f\right)e^{-2\kappa W} \\ &\approx eV\rho_s\left(0,E_f\right)e^{-1.025\sqrt{\Phi}W} \end{aligned} \tag{2.11}$$

where $\rho_s\left(0,E_f\right)$ is the LDOS near the Fermi level of the sample at the sample surface [12]. According to (2.11), the current decay is about $e^2 \approx 7.4$ times per Å. Therefore, the dependence of the logarithm of the tunneling current with respect to distance is a good measure of the work function or the tunneling barrier height [13, 14].

2.3. Scanning tunneling spectroscopy

2.3.1. Feedback loop system

For operating the STM system, it is necessary to measure the current and control the movement of the tip to accurately track the surface topography, and then to translate the information into an useable form. A feedback loop is installed to constantly monitor the tunneling current and adjusts the tip to maintain a constant tunneling current that is continuously compared to a set–point current. If both currents are not equal, the z–piezo will move the tip closer or farther from the sample surface to minimize the error signal. These adjustments are recorded by the computer and presented as an STM image. One of the first STM feedback system was described by Park and Quate et al. [15]. Later, A. I. Olive et al. analyzed theoretically the feedback system in the STM [16].

2.3.2. *I*–*V* spectroscopy

For understanding the tunneling phenomena in STM, the concepts developed through the study of metal-insulator-metal (MIM) tunneling experiments were demonstrated by Giaever et al. [17, 18]. The most extensively theoretical method to understand the MIM tunneling junction (referring to the tip–sample tunneling junction) is the time–dependent perturbation approach developed by Bardeen [19]. A schematic diagram of the Bardeen approach is presented in Figure 2.4. In Bardeen approach, instead of trying to solve the Schrödinger equation of the combined system,

© 2012 Tous droits réservés.

the system is considered as two separated subsystems. The electronic states of each system are obtained by solving the stationary Schrödinger equation and the rate of transferring an electron from one electrode to the other (from the tip to the sample) is calculated by using time−dependent perturbation theory [4].

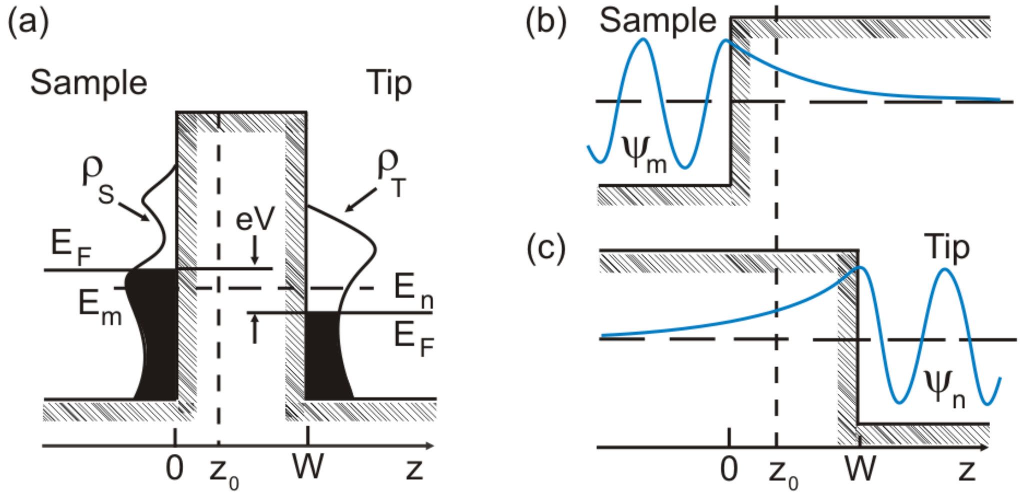

Figure 2.4: The Bardeen approach to tunneling theory. Instead of solving the Schrodinger equation for the coupled system, (a), Bardeen (1960) makes clever use of perturbation theory. Starting with two free subsystems, (b) and (c), the tunneling current is calculated through the overlap of the wave functions of free systems using the Fermi golden rule. Here, (ψ_m, E_m) *and* (ψ_n, E_n) *are the wave functions of the* m *and* n *states respectively;* E_f *is the Fermilevel;* ρ_S *and* ρ_T *are the density of state (DOS) of the sample and the tip correspondingly;* W *is the distance between the two electrodes (tip and sample).*

Later, in the mid-1980s, also by using time-dependent perturbation theory, Tersoff and Hamann [20, 21] calculated the wave function of the total system. In their approach, the potential of the tip is described as a perturbation, $V_T(t)$, and is plugged into the time-dependent Schrödinger equation:

$$i\hbar \frac{\partial \psi_n}{\partial t} = \left[-\frac{\hbar^2}{2m} \frac{\partial^2}{\partial z^2} + V_S + V_T(t) \right] \psi_n \qquad (2.12)$$

where V_S refers to the potential of the substrate (or the sample) and ψ_n refers to the wave function of the n^{th} state. The wave function $\psi_n(z,t)$ is often assumed to have the form of $\psi_n(z,t) = \psi_n(z) e^{-iE_n t/\hbar}$.

Consequently, the amplitude of electron transfer, or the tunneling matrix element M, is determined by the overlap of the surface wave functions of the two subsystems at a separation surface [4]. In other words, the tunneling matrix element M is

© 2012 Tous droits réservés.

determined by a surface integral on a separation surface between the two electrodes [19], $z = z_0$:

$$M_{mn} = -\frac{\hbar^2}{2m} \int\limits_{z=z_0} \left(\psi_m^* \nabla \psi_n - \psi_m \nabla \psi_n^* \right) dS \qquad (2.13)$$

here ψ_m and ψ_n are also the wave functions of the sample and the tip respectively and dS is the surface element. The rate of electron transfer is then determined by the Fermi golden rule [22]. Specifically, the transition probability w_{mn} of an electron tunneling from the n^{th} state into the m^{th} state can be written as:

$$w_{mn} = \frac{2\pi}{\hbar} \left| M_{mn} \right|^2 \delta\left(E_m - E_n \right) \qquad (2.14)$$

The δ function in equation (2.14) indicates that only the states with the same energy level in both electrodes can contribute to the tunneling effect. The tunneling current is calculated by summing up over all possible electronic states. At any finite temperature, the electron density in both the sample and the tip follows the Fermi distribution function. If the density of state (DOS) of the tip and the sample are presented by ρ_T and ρ_S, respectively, at a bias voltage V, we obtain:

$$I = \frac{4\pi e}{\hbar} \int_{-\infty}^{+\infty} \left[f\left(E_F + \varepsilon \right) - f\left(E_F + eV + \varepsilon \right) \right] \rho_S\left(E_F + \varepsilon \right) \rho_T\left(E_F + eV + \varepsilon \right) \left| M \right|^2 d\varepsilon \qquad (2.15)$$

where $f(E) = \left\{ 1 + \exp\left[\left(E - E_F \right) / k_B T \right] \right\}^{-1}$ is the Fermi distribution function.

If $k_B T$ is smaller than the energy resolution required in the measurement, then the Fermi distribution function can be approximated by a step function. In this case, the tunneling current is:

$$I = \frac{4\pi e}{\hbar} \int_{0}^{eV} \rho_S\left(E_F + \varepsilon \right) \rho_T\left(E_F + eV + \varepsilon \right) \left| M \right|^2 d\varepsilon \qquad (2.16)$$

If it is assumed that the magnitude of the tunneling matrix element does not change appreciably in the interval of interest, then, the tunneling current is determined by the convolution of the DOS of both electrodes [18, 19]:

$$I \propto \int_{0}^{eV} \rho_S\left(E_F + \varepsilon \right) \rho_T\left(E_F + eV + \varepsilon \right) d\varepsilon \qquad (2.17)$$

© 2012 Tous droits réservés.

Assuming that only s-like wave functions contribute to the tunneling from the tip with radius R, the density of states of the tip near the Fermi level can be represented by:

$$\rho_T\left(E_f\right) \propto \left|\psi_n\right|^2 \propto e^{-2\kappa(R+z)} \tag{2.18}$$

with z is the distance from the tip to the sample surface and κ in this case has the form:

$$\kappa = \sqrt{\frac{2m}{\hbar^2}\frac{\left(\phi_T+\phi_S\right)}{2} - E + \frac{eV}{2}} \tag{2.19}$$

where ϕ_T and ϕ_S are the work functions of tip and sample, and E is the energy of state relative to the Fermi level, and $\phi = \left(\phi_T+\phi_S\right)/2$ is considered as the effective work function. Generally we assume that only electron states near the Γ point of the surface Brillouin zone contribute to the tunneling. Otherwise, if the latter condition is not satisfied, (2.7) can be replaced by:

$$\kappa = \sqrt{\frac{2m}{\hbar^2}\frac{\left(\phi_T+\phi_S\right)}{2} - E + \frac{eV}{2} + k_{\|}^2} \tag{2.20}$$

in which $k_{\|}$ is the parallel momentum of the surface electronic state.

Thus:

$$I \propto \int_0^{eV} \rho_S\left(E+\varepsilon\right) e^{-2\kappa z} dE \tag{2.21}$$

To simplify the writing of the equations, we define the energy− and bias−dependent electron transmission probability T as [23]:

$$T\left(E,eV\right) = \exp\left(-2\kappa z\right) = \exp\left(-\frac{2z\sqrt{2m}}{\hbar}\sqrt{\frac{\Phi_S+\Phi_T}{2}+\frac{eV}{2}-E}\right) \tag{2.22}$$

The structure of dI/dV as a function of sample bias V is associated with the DOS of the surface whenever the sample bias is less than the work functions of the tip and the sample. It has the form:

$$\frac{dI}{dV} \propto e\rho_S\left(eV\right)T\left(eV,eV\right) + e\int_0^{eV} \rho_S\left(E_f+\varepsilon\right)\frac{d}{d\left(eV\right)}\left(T\left(\varepsilon,eV\right)\right)d\varepsilon \tag{2.23}$$

© 2012 Tous droits réservés.

Although the tunneling transmission probability is generally unknown, T varies smoothly and monotonously based on Equation (2.22) in the WKB approximation. Hence, the structure in dI/dV usually features the DOS in the first term in (2.23) [24].

From equation (2.22), it is seen that the transmission probability, T, depends on the tip–sample distance, hence the tunneling current I (equation (2.21)) and the conductance dI/dV (equation (2.23) also strongly depends on the tip–sample distance). Therefore, in order to be able to compare the similar measurements and also to minimize the dependence of dI/dV on tip–sample distance, it is necessary to normalize the conductance by dividing dI/dV by I/V, we obtain [25, 26, 27]:

$$\frac{dI/dV}{I/V} = \frac{\rho_S(eV) + \int_0^{eV} \frac{\rho_S(E_f+\varepsilon)}{T(eV,eV)} \frac{d}{d(eV)} \left(T(\varepsilon, eV) \right) d\varepsilon}{\frac{1}{eV} \int_0^{eV} \rho_S(E_f+\varepsilon) \frac{T(\varepsilon,eV)}{T(eV,eV)} d\varepsilon} \qquad (2.24)$$

Because $T(E,eV)$ and $T(eV,eV)$ appear as ratios in the numerator and denominator of this equation, their exponential dependences on V and z tend to cancel [26]. The first term in the numerator of (2.24) is simply the LDOS of the sample.

- For $V > 0$: $T(E,eV) \le T(eV,eV)$, and the maximum transmission occurs at $E = E_{f,Tip}$. Because all the terms in (2.24) are of the same order of magnitude, so a normalized is DOS measured in addition to a slowly varying background.
- For $V < 0$: $T(E,eV) > T(eV,eV)$, the maximum transmission now occurs at $E = E_{f,Sample}$. The background term and the term in the denominator are of the same order, but both are larger than at positive bias. Therefore, it is usually more difficult to probe the low–lying filled surface states of the substrate.

By using the tunneling spectroscopic mode (STS), the LDOS is usually obtained by averaging hundred of $I-V$ traces on a given location on the sample surface. The dI/dV can also be recorded on each point on a selected area. If the surface is well–ordered the extend of electronic states can then be mapped out [28].

2.3.3. Inelastic electron tunneling spectroscopy

Experimentally, the major part of the electrons pass across the tunnel barrier without energy loss, but a small amount can also release some of their energy due to scattering events. Measuring these events have given rise to inelastic electron tunneling spectroscopy (IETS) [29, 30, 31, 32, 33, 34]. Considering the case of a molecule in a tunneling junction, electrons from the tip can be injected into this molecule and lose

© 2012 Tous droits réservés.

part of their energy before tunneling to the sample electrode. This loss of energy can occur with the emission of photons or vibrations.

Welmsley et al. [30] have reported very useful IETS spectra by measuring currents and voltages across a metal–insulator–adsorbate–metal (M–I–A–M) device in a special way that is able to extract vibrational and electronic spectroscopic information about the metals (magnons and photons), the insulator and the adsorbate [35]. Additionally, relying on IETS developed by Jackvic and Lambe since 1960s [36], Binnig et al. [37] have reported the method for extracting the vibrational structure of single molecule.

The advantages of IETS include [35]:

- Ultra–high sensitivity: less than 10^{13} molecules are required to provide a spectrum [29, 38, 39].
- Overtone and combination bands are exceptionally weak [29, 33, 40, 41, 42, 43, 44, 45, 46].
- Optically, forbidden transitions may be observed as strong bands [47, 48, 41].
- Oxide bands are generally less intense than adsorbate bands. It is possible to obtain adsorbate spectra in the "IR opaque" regions of oxide spectrum [29, 30, 31, 32, 33, 34].

Elastic tunneling

In Ref. 33, Hips and Mazur have explained in detail the IETS by using an Al–Al_2O_3–anthracene–Pb diode (Figure 2.5). In their work, the free electron theory is used to model the metals (Al and Pd). The insulator (anthracene) is treated as a vacuum space. The electron states are filled up to the Fermi energy E_f, the work function of the metal is given by Φ. Whenever a metal is brought in contact with an insulator, electrons flow via tunneling until the Fermi surfaces (from the two electrodes) are matched [33]. As drawn in Figure 2.5, the HOMO (Highest Occupied Molecular Orbital) and the LUMO (Lowest Unoccupied Molecular Orbital) of anthracene are considered as well as a few schematically vibrational levels. Additionally, the interaction between the metallic electronde and the anthracene causes a shift in anthracene's zero of energy but does not produce significant changes in its level spacing [33].

Assuming that a small positive voltage, V, is applied to the Pb electrode $(\Sigma(Pb))$ in Figure 2.5(a). The molecule , X, being closer to the Pb than to the Al, its potential stays very close to that of Pb. At this point, electrons have sufficient energy to tunnel

© 2012 Tous droits réservés.

into the empty states of $\left(\Sigma\left(Pb\right)\right)$ electrode [33]. If the electrons do not lose energy, they tunnel elastically [33]:

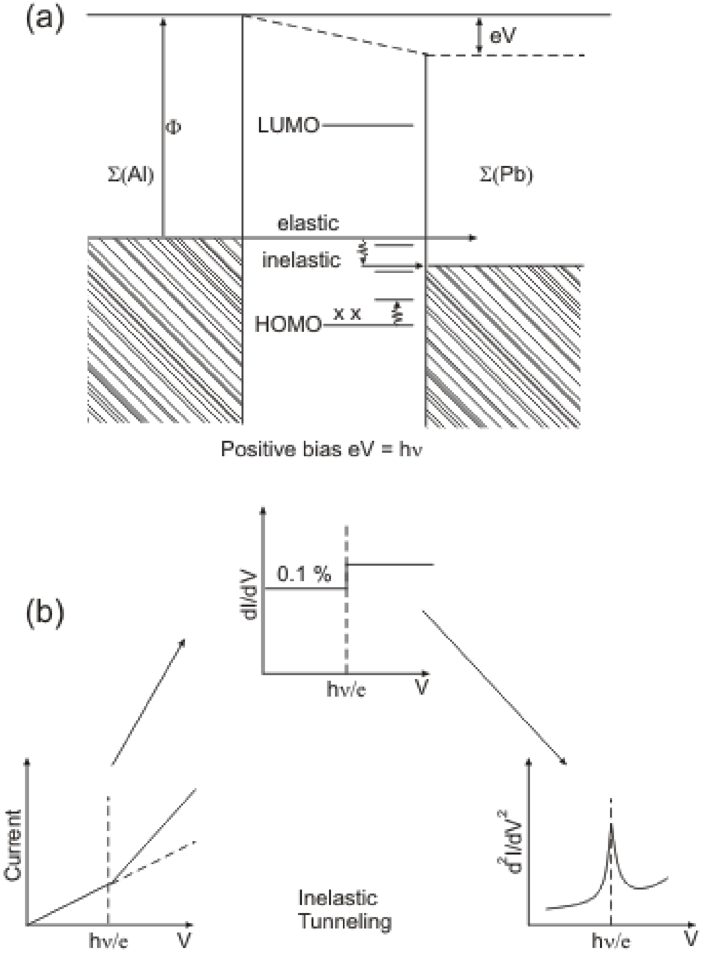

Figure 2.5: Energy diagram for a mode $Al\text{–}Al_2O_3\text{–}$*anthracene*$\text{–}Pb$ *tunnel diode showing elastic and inelastic tunneling channels (a). The hatched regions present the filled states of the two electrodes. The area in the center shows the insulator and adsorbate. The HOMO and LUMO orbital energies and a few vibrational levels are indicated. Energy loss (equilibration) for tunneling electron occurs through a cascade process in the molecular layer electrode. The* $I-V$ *curve, conductance–curve, and the IETS spectrum resulted from an inelastic channel opening at* $V=h\nu/e$ *are shown (b)* [33].

Inelastic tunneling

Besides elastic tunneling, there are also other tunneling mechanisms that could give contribution to the current. Through the tunneling process, the electronic charge interacts with time-varying molecular dipoles (electronic or vibrational) to induce excitation of the molecule in the barrier resulting to the loss of energy by the electron.

© 2012 Tous droits réservés.

The inelastic channel just opens at the bias voltage of $V = h\nu/e$, and results in additional final states with an associated increase in current due to this new channel [33]. As depicted in Figure 2.5(b), there is a change in the slope of $I(V)$ curve at $V = h\nu/e$. Correspondingly, the dI/dV curve shows a step at the same value of the voltage. Plotting the d^2I/dV^2 versus V produces a peak at $V = h\nu/e$. The width of this peak depends on the sharpness of the onset of the inelastic process. The IETS line width depends on temperature and is about ~0.434T mV/K [49], T is the experimental temperature. Experimentally, an IET (Inelastic Electron Tunneling) spectrum is a plot of d^2I/dV^2 versus V [42, 50].

2.3.4. *Z–V* spectroscopy

In this mode, the feedback loop is kept closed while the bias voltage V varies. As a result, the regulator adjusts Z in order to remain I constant. The tip–sample distance variations Z are stored as a function of V.

This mode is often used to measure the height of the tunnel barrier, when eV becomes comparable to $\phi = \frac{\phi_T + \phi_S}{2}$, the shape of the barrier progressively becomes triangular and when eV becomes greater than ϕ, oscillations of the tip-sample distance are detected due to the occurrence of field emission resonances. The first experiments to show resonances caused by the localized states in the barrier was published by Binnig et al. [2].

Despite that this mode is also able to detect the changes of the tip and sample density of state ρ_T and ρ_S, it is not broadly used because of the lack of resolution . It is not allowed to do spectroscopy at both negative and positive biases in the same spectrum, because, when V reaches to zero, the tip and the sample will enter into contact.

2.3.5. *I–Z* spectroscopy

As described above, the tunneling current depends exponentially on the tip-surface separation, i.e., $I \propto e^{-2\kappa z}$, and also on the effective work function ϕ. For large tip–sample distances, the effective work function must approach the surface local work function (but if the tip and the sample do not have the same work function, it will be an average work function) which is defined as the work needed to remove an electron from the solid's Fermi level to a position far away from the surface, so that image force effects can be neglected.

The work function of the substrate may exhibit some spatial variation, which can be easily determined because the work function of the tip is usually fixed. The most straightforward method to determine the effective work function ϕ is to open the

© 2012 Tous droits réservés.

feedback loop and quickly measure the current I as a function of tip–sample separation z [51, 52, 53]. Subsequently, $\ln(I)$ can be plotted versus the tip–sample distance:

$$\ln(I) \approx -2\left(\sqrt{\frac{2m\phi}{\hbar^2} - E - \frac{eV}{2}}\right)z \qquad (2.25)$$

If the sample bias is small, and the electronic structures of the sample and the tip are neglected, the effective work function, Φ_{eff}, can be extracted from the $\ln(I)$ curve versus tip–sample distance z:

$$\Phi_{eff} \approx \left(\frac{d\ln(I)}{dz}\right)^2 \qquad (2.26)$$

2.4. The Omicron Low Temperature Scanning Tunneling Microscopy

In this thesis, the main microscope I worked with is a Low-Temperature Scanning Tunneling Microscopy (LT-STM), a commercial product from Omicron Nanotechnology (Figure 2.6). It is able to perform experiments in Ultra-High Vacuum (UHV) (the pressure ~ 7.5×10^{-11}) and also at low temperatures (77 K with liquid Nitrogen or 5 K with liquid Helium). All the UHV chambers are made of stainless steel and connected together via the gate valves.

Additionally, during my secondment at Gerhard Meyer's group in IBM Zurich Research Laboratory I worked with a home-built LT-STM combined with a photon detection system.

The Omicron LT-STM consists of:

2.4.1. The load-lock chamber

It can be considered as the gate for loading the samples, the tips,… from the air into the UHV chambers. This chamber contains a sliding transfer rod with three places for positioning samples or tips. Samples are loaded through a viewport that can be opened. It has a viton gasket instead of a copper gasket. The disadvantages of using a viton gasket is the maximum bake-out temperature, 120 °C, that for some samples does not allow to desorb all contaminants. The vacuum level in the load-lock is limited, the highest vacuum is 1×10^{-9} *Torr* using a turbomolecular pump.

2.4.2. The preparation chamber

The vacuum in this UHV chamber usually reaches the value of ~7.5×10^{-11} *Torr* that is achieved with an ion getter pump and a Titanium Sublimation Pump (TSP).

© 2012 Tous droits réservés.

When the load-lock and the preparation chambers are pumped down, the valve can be opened and the transfer rod of the load-lock can slide into the preparation chamber. The samples can be transferred into the preparation chamber by using the second sliding transfer rod located in the preparation chamber. Inside the preparation chamber, there is a storage place with 5 slots and a manipulator that allows storing and preparing the sample for the STM experiment.

The manipulator can hold one sample and is able to move in three-dimensions and rotate around it axis. The manipulator has a resistive heater, a thermocouple and different electrical connections. As a result, the sample can be thermally prepared by resistivity heating or by an established current through it. Experimentally, the use of this manipulator is important because it allows the preparation of extremely clean samples and unpolluted tips.

- In our experiments, the tip is made from a polycrystalline tungsten wire and prepared by electro-chemical etching process in NaOH solution. After that, it is introduced into the load-lock chamber and consequently to the UHV preparation chamber by the transfer rod. Whenever the tip is on the manipulator, the tungsten wire of the tip is connected to a finger at the ground potential and the manipulator is polarized, so that, the tip is heated by Joule effect. Regularly, the tip is baked out at high temperatures (about 1000 K, orange color) for several hours to get rid of the oxide by an established current running through the foil contacting the tip. Finally, some flashes are done to the yellow color to remove all the contaminants.

- Resistive samples, like semiconductor, also need to be heated to remove their native oxide layer, to clean and also reconstruct the surface without defects. In this case, one end of the sample is polarized against the other and a current runs through the sample to be heated by Joule effect.

- With metallic samples, the procedure is different as they are not resistive material. Usually, metal surfaces are cleaned by repeated cycles of ion sputtering and heating. The ion sputtering aims at desorbing the contaminants. Regularly, it is done with Argon gas and an ion gun facing the manipulator. Due to the fact that the surface is damaged by the sputtering process, the surface needs to be reconstructed by heating with the resistive heater of the manipulator. This sequence must be repeated several times for removing the contaminants of the surface.

Below the manipulator, there is an evaporation stage. Once the selected material is put on this stage, it can be evaporated to adsorb on another sample hold on top in the manipulator. The presence of molecules in the atmosphere of the chamber is detected by a mass spectrometer. It is quite important to check out the desorption of materials when nanostructures are capped to be protected from air contaminants. Additionally, the preparation chamber also contains a gas inlet and a tungsten filament used for

© 2012 Tous droits réservés.

special surface reconstructions like hydrogenation or nitridation. The gas (hydrogen or nitrogen) is cracked by the filament and heated to high temperature, then, the resulting ions are attracted by an electric field created by polarizing the sample.

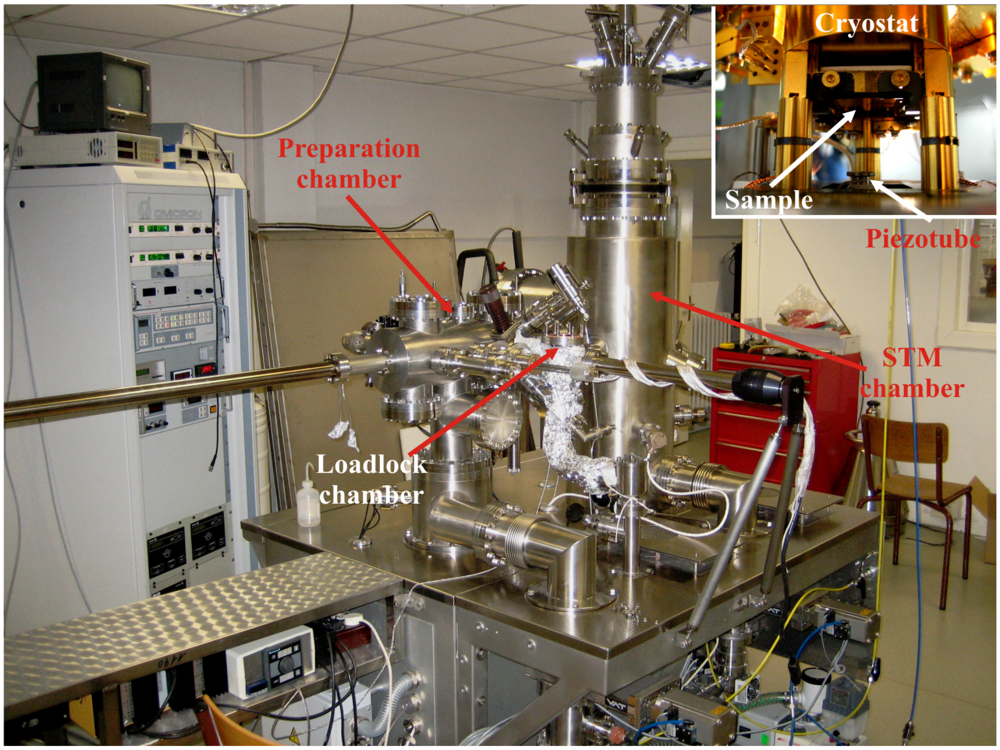

Figure 2.6: Outside view of the Omicron LT-STM and inside view (the inset image) of the STM chamber

2.4.3. The STM chamber

This chamber is maintained in UHV by an ion getter pump and a TSP. The base pressure at room temperature after bake–out is 7×10^{-11} *T*. There are six available positions in the carrousel for containing samples or tips and a wobblestick is used to transfer samples and tips into the STM. Two cryostats are connected to the STM to cool down the system. One of the two cryostats (the outer) acts as a shield and is filled with Nitrogen, whereas the second cryostat (the inner) can be filled up with Nitrogen or Helium corresponding to temperatures of 77 *K* and 5 *K*.

While scanning, the tip is moved and the sample is fixed. The movements of the tips are classified as:

- Coarse positioning is done through a “stick and slip” piezoelectric system. It makes possible to move the tip in the X, Y, Z coordinate system with displacements of 5 *mm*, 5 *mm*, and 10 *mm*, see Figure 2.7.

© 2012 Tous droits réservés.

- Fine movements and images scans are made by a piezoelectric tube on top of which the tip is mounted. At room temperature, it can move over an area of $10\mu m \times 10\mu m$ and the tip is able to move in the Z direction by some micrometers. As temperature decreases, the sensitivity of the piezo also decreases. As a result, for the same excitation, a smaller area is covered. For example: at 4K, the tube is only able to scan an area of $1.8\mu m \times 1.8\mu m$ laterally and. The z–piezo extends over $0.2\mu m$ only.

In order to be able to work with a high resolution, the system must be isolated from any vibration. As the STM is kept in high vacuum, there is no coupling with vibrations coming from the air, like acoustic wave, but the mechanical vibrations from the floor might affect the UHV chamber. So, the STM is mounted on an Eddy current damping system. While operating, the STM is in the suspended state at low temperatures.

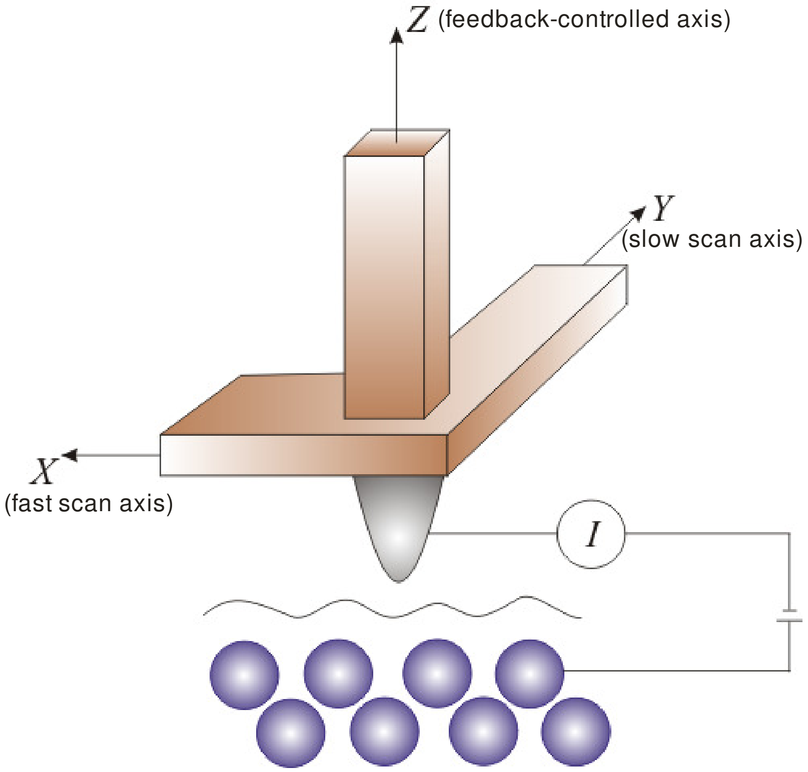

Figure 2.8: Simplified schematics of a STM.

2.5. X–Ray Photoelectrons Spectroscopy (XPS)

Photoelectrons spectroscopy (or photoemission) had been developed since 1960s by K. Siegbahn et al. [54] based on the determination, at high resolution, of binding energy of electrons emitted from a material by the photoelectronic effect [55, 56].

© 2012 Tous droits réservés.

Analysis of the binding energy allows to characterize precisely the chemical composition of the surface material, and to determine the chemical environment of different atomic species.

2.5.1. Principle of XPS

Figure 2.8 presents the photoemission energy diagram of a semiconductor. This energy diagram as is available for deducing the kinetic energy E_{Kin} of electrons emitted from a semiconductor surface under illumination, the photon energy of an incident beam is $h\upsilon$. The binding energy of electron E_L and the workfunction of the material ϕ_S are related to E_{Kin} by:

$$E_{Kin} = h\nu - E_L - \phi_S \qquad (2.27)$$

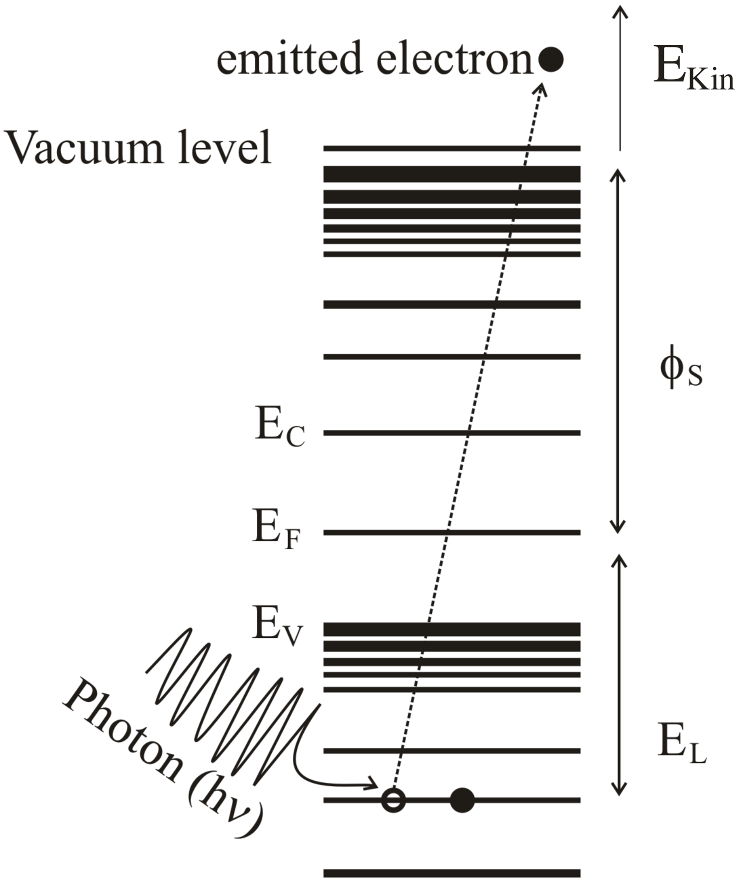

Figure 2.8: Energy diagram for the photoemission of a semiconductor material; KE is the kinetic energy; ϕ_S *is the workfunction of the material;* E_L *is the binding energy of electron;* E_C *,* E_F *, and* E_V *are the conduction band, Fermi and valence band levels respectively.*

© 2012 Tous droits réservés.

The presence of a continuum energy above the vacuum level allows the absorption of all photons with energy higher than the vacuum level: $I = \phi_S + E_L$, so there is no selection rule. The excess of energy is transferred to electrons in form of kinetic energy: $E_{Kin} = h\nu - I$.

There are two kinds of electrons that are collected in photoemission experiment:

- **Primary electrons**: the electrons are emitted faster without collision before escaping from the material.
- **Secondary electrons**: the electrons lose energy (inelastic diffusion) before they reach to the material surface.

The spectra of collected electrons then are the combination of primary electrons and secondary electrons which have kinetic energy close to zero. Here, the emitted electrons are collected by a kinetic–energy analyzer which plays a role as a filter.

During the measurement, the sample is electrically connected to the spectrometer (analyzer) via the sample holder, the electronic and the cable of the system is considered to have the Fermi level aligned with each other. The work function of the analyzer (ϕ_A) and the one from the sample (ϕ_S) are different due to the difference of the contact potential between the sample and the analyzer. Normally, ϕ_A is smaller than ϕ_S, as consequence, there will be an acceleration of the emitted electrons when they reach the analyzer and their increase of energy will be: $\phi_S - \phi_A$. Hence, the kinetic energy of the primary electron will be:

$$E_{Kin} = h\nu - E_L - \phi_S + (\phi_S - \phi_A) = h\nu - E_L - \phi_A \qquad (2.28)$$

All the spectra are displaced by the workfunction difference $(\phi_S - \phi_A)$ toward high energy (in case $\phi_S > \phi_A$). So, the electrons extracted from the sample can bombard the surface of the analyzer and also create secondary electrons. These electrons are not affected by the contact potential and contribute to secondary electrons of the sample in the final spectra. In order to distinguish two types of electrons in the spectra, it is better to use a potential difference between the sample and the analyzer: E_{acc}.

By using E_{acc}, the kinetic energy of the primary electron becomes:

$$E_{Kin} = h\nu - E_L - \phi_A + E_{acc} \qquad (2.29)$$

The equation in (2.29) shows that the kinetic energy of a primary electron measured by the analyzer does not depend on the workfunction of the material but on the workfunction of the analyzer.

© 2012 Tous droits réservés.

For the expression (2.29), it is necessary to know the binding energy of the electrons emitted by the material but the workfunction of the analyzer generally is not continuous. So, to be able to solve this problem, the Fermi level of metal (Au, Ag, …) is preferred to be used experimentally for calibrating the scale of the kinetic energy by comparing it to the Fermi level E_F of the sample.

2.5.2. XPS instrument

The X–ray photoelectron spectroscopy requires to operate in a high vacuum environment (10^{-9} to 10^{-10} mbar). In fact, it is necessary to avoid the collision between electrons with molecules of residual gas before the electrons reach the analyzer. The illustration of the main elements of an XPS system is exhibited in Figure 2.10. It includes:

- A source of monochromatic photon at an energy of 1487 eV in the wavelength range.
- An analyzer that measures the kinetic energy of electrons.

Additionally, there is also a system of vacuum pump used to maintain the ultra high vacuum inside the vacuum chamber where the measurements are carried out.

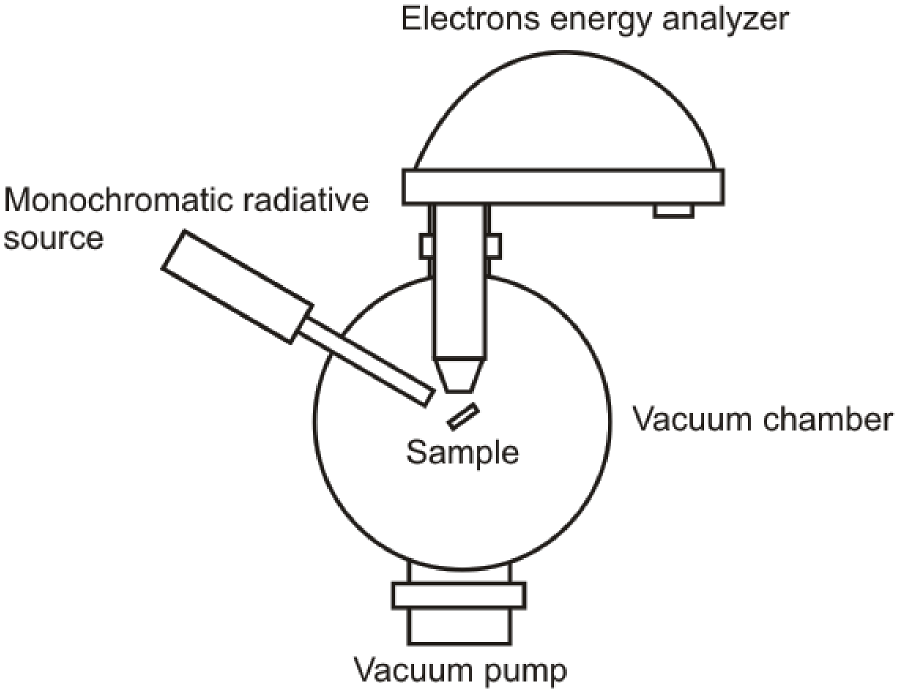

Figure 2.9: Illustration of the main components of a XPS spectrometer

© 2012 Tous droits réservés.

2.5.3. Analyzer and detector

The analyzer that measures the kinetic energy of electrons is a device that allows to scatter the kinetic energy of electrons. Thus, it can be considered as a filter. Figure 2.10 shows a Concentric Hemispherical Analyzer (or CHA) containing two non–oxidizing steel concentric hemispheres with radius R_1 and R_2 respectively for the inner and outer hemispheres.

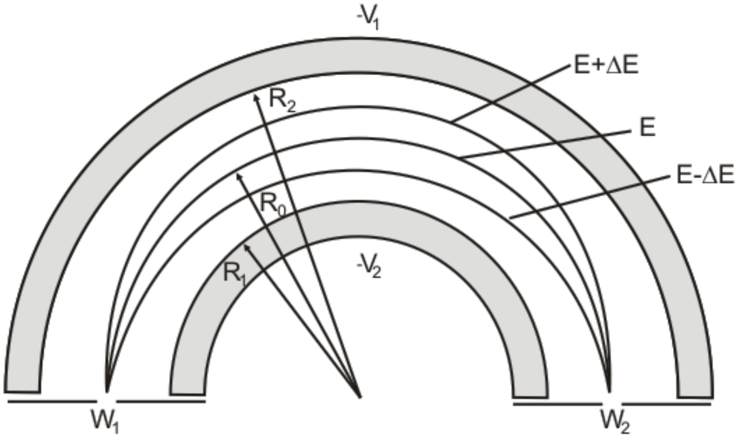

Figure 2.10: Schematic illustration of an electron–energy analyzer

A negative potential is applied to both hemispheres as V_1 and V_2 ($V_1 < V_2$) (Figure 2.10). The entrance and exit slits have the width of W_1 and W_2 respectively and locate on the same plane with the centre of the two hemispheres. R_0 is the radius of the surface of homogenous potential sphere in the middle of the analyzer.

The potential of this equipotential surface (V_0) is presented as:

$$V_0 = \frac{V_1 R_1 + V_2 R_2}{2R_0} \tag{2.30}$$

This expression indicates that whenever the electrons reach the entrance slit with a kinetic energy of $E = eV_0$, they follow a path along the equipotential surface and then escape from the exit slit. The others electrons having an energy different from eV_0 will follow others paths and will not exit the analyzer.

R_0, R_1 and R_2 are fixed, but V_1 and V_2 can vary. Therefore, it is possible to select the electrons (by their kinetic energy) to pass the analyzer and travel to the detector. However, it is necessary to keep the same absolute resolution ΔE (the FWHM of peaks) in all spectra. The relative resolution is defined as:

© 2012 Tous droits réservés.

$$R = \frac{\Delta E}{E} \tag{2.31}$$

Considering an absolute resolution of 0.7 eV, it is necessary o have a relative resolution 0.07 for kinetic energy of E = 10 eV and another relative resolution of 0.0007 for energy of 1000 eV. In fact, the resolution 0.0007 is not achievable unless the analyzer is as large as:

$$R = \frac{\Delta E}{E} = \frac{W}{R_0} \text{ with } W = \frac{W_1 + W_2}{2} \tag{2.32}$$

In order to get the same absolute resolution on all spectra, the electrons are slowed by a system of electrostatic lens before going inside the analyzer. At the entrance of the analyzer, all the electrons have the same kinetic energy which is called the "*pass energy*". Then, the Expression in (2.32) becomes:

$$R = \frac{\Delta E}{E_0} = \frac{W}{R_0} \tag{2.33}$$

E_0 is fixed by the potentials imposed in the hemispheres of the analyzer. The electrons are slowed down with electrostatic lens until their energy reaches E_0. Thanks to these magnetic lenses, only the electrons with the kinetic energy of E_0 can be focused at the entrance slit of the analyzer.

As the electron current arriving at the exit slit of the analyzer is in the order of some femto–Ampere ($10^4\, e^- / s$), the electrons are recorded as the pulse signal as a function of their kinetic energy. An electron multiplier is attached after the exit slit to ensure the efficiency of electron detection.

2.6. Conclusion

This chapter discussed the principles of the scanning tunneling microscope. Theoretical background of STM has been introduced based on quantum tunneling effect between two electrodes. The exponential dependence of the tunneling current on the tip-sample distance and its localization makes possible to image the surface with atomic resolution and even probes the density of states and electronic configuration of single nano-object through the STS technique. Various types of spectroscopy modes were presented as $I-V$ spectroscopy, $Z-V$ spectroscopy, $I-Z$ spectroscopy. Those modes will be quite useful to study the electronic properties of nano–objects. Finally, in order to better understand the environment of the nano–objects, the analysis of photoelectrons can be performed with X–ray photoelectron spectroscopy.

© 2012 Tous droits réservés.

References

---

[1] Müller EW, "*The field ion microscope*", Z. Phys. 131:136–42 (1951).

[2] Binnig G, Rohrer H, "*Scanning Tunneling Microscopy*", Helv. Phys. Acta, **55**, 726 (1982).

[3] C. Bai, "*Scanning tunneling microscopy and its applications*", New York: Spinger Verlag. ISBN 3540657150 (2000).

[4] C. Julian Chen, "*Introduction to Scanning Tunneling Microscopy*", Oxford University Press. ISBN 0195071506 (1993).

[5] M.S. Hoogeman, D. Glastra van Loon, R.W.M. Loos, H.G. Ficke, E. de Haas, J.J. van der Linden, H. Zeijlemaker, L. Kuipers, M.F. Chang, M.A.J. Klik, and J.W.M. Frenken, "*Design and performance of a programmable-temperature scanning tunneling microscope*", Rev. Sci. Instr. **69**, 2072 (1998).

[6] L. Kuipers, R.W.M. Loos, H. Neerings, J. ter Horst, G.J. Ruwiel, A.P. de Jongh and J.W.M. Frenken, "*Design and Performance of a High-Temperature High-Speed STM*", Rev. Sci. Instr. **66**, 4557 (1995).

[7] P. B. Rasmussen, B. L. M. Hendriksen, H. Zeijlemaker, H. G. Ficke, J. W. M. Frenken, "*The 'Reactor STM': A scanning tunneling microscope for investigation of catalytic surfaces at semi-industrial reaction conditions*", Rev. Sci. Instr. **69**, 3879, (1998).

[8] R. Wiesendanger, I. V. Shvets, D. Bürgler, G. Tarrach, H.-J. Güntherodt, and J. M. D. Coey, "*Recent advances in spin-polarized scanning tunneling microscopy*", Ultramicroscopy **338**, 42–44 (1992).

[9] D. M. Eigler, and E. K. Schweizer, "*Positioning single atoms with a scanning tunneling microscope*", Nature **344**, 524–526 (1990).

[10] J. A. Stroscio, D. M. Eigler, "*Atomic and molecular manipulation with the scanning tunneling microscope*", Science **254**, 1319–1326 (1991).

[11] H. J. Lee, W. Ho, "*Single-bond formation and characterization with a scanning tunneling microscope*", Science **286**, 1719–1724 (1999).

[12] C. Julien Chen, "*Introduction to Scanning Tunneling Microscopy*", Oxford University Press. ISBN 0195071506 (1993).

[13] Coombs, J. H., and Pethica, J. B, *"Properties of vacuum tunneling currents: anomalous barrier heights",* IBM J. Res. Develop. **30**, 455–459 (1986).

[14] Garcia. N, "*Theory of scanning tunneling microscopy and spectroscopy: Resolution, image and field states, and thin oxide layers",* IBM J. Res. Develop. **30,** 533–542 (1986).

[15] Park S. I, Quate C. F, "*Theories of the feedback and vibration isolation systems for the scanning tunneling microscope*", Rev. Sci. Instrum. **58**, 2004–2009 (1987).

[16] A. I. Olive, E. Anguiano, N. Denisenko, M. Aguilar, and J. L. Pena, "*Analysis of scanning tunneling microscopy feedback system*", Rev. Sci. Instrum. **66**, 3196–3203 (1995).

© 2012 Tous droits réservés.

---

[17] I. Giaever, "*Energy gap in superconductors measured by electron tunneling*", Phys. Rev. Lett. **5**, 147−148 (1960).

[18] I. Giaever, "*Electron tunneling between two superconductors*", Phys. Rev. Lett. **5**, 464−466 (1960a).

[19] J. Bardeen, "*Tunneling from a many-particle point of view*", Phys. Rev. Lett. **6**, 57–59 (1960).

[20] J. Tersoff , and D. R. Hamann, "*Theory and application for the scanning tunneling microscope*", Phys. Rev. Lett. **50,**1998–2001 (1983).

[21] J. Tersoff, and D. R. Hamann, "*Theory of the scanning tunneling microscope*", Phys. Rev. B **31**, 805–13 (1985).

[22] L. D. Landau, and L. M. Lifshitz, "*Quantum Mechanics",* third edition, Pergamon Press, Oxford (1977).

[23] R. J. Hamers and D. F. Padowitz, "*Methods of Tunneling Spectroscopy with the STM*," from *Scanning Probe Microscopy and Spectroscopy: Theory, Techniques, and Applications*, 2nd ed., Ed. by D. A. Bonnell, New York: Wiley-VCH, Inc., 2001.

[24] R. Wiesendanger, "*Scanning Probe Microscopy and Spectroscopy: Methods and Applications"*, Cambridge, UK: Cambridge University Press, 1994.

[25] J. A. Kubby, J. E. Griffith, R. S. Becker, and J. S. Vickers, "*Tunneling microscopy of Ge(001)*", Phys. Rev. B **36,** 6079–93 (1987).

[26] R. M. Feenstra, J. A. Stroscio, A. P. Fei, "*Tunneling spectroscopy of the Si(111)2×1 surface*", Surf. Sci. **181**, 295–306 (1987).

[27] R. J. Hamers, P. H. Avouris, and F. Boszo, "*Imaging of chemical-bond formation with the scanning tunneling microscope-NH3 dissociation on Si(001)*", Phys. Rev. Lett. **59,** 2071–74 (1987).

[28] M. F. Crommie, C. P. Lutz, and Eigler, "*Confinement of electrons to quantum corrals on a metalsurface*", Science **262,** 218–20 (1993).

[29] P. K. Hansma, "*Tunneling Spectroscopy*", Plenum Press, New York (1982)

[30] D.G. Walmsley and J.L. Tomlin, "*Compilation of inelastic electron tunnelling spectra of molecules chemisorbed on metal oxides*", Prog. Surf. Sci., **18**, 247–447 (1985).

[31] J.T. Yates and T.E. Madey (eds), "*Vibrational Spectroscopy of Molecules on Surfaces*", Plenum Press, New York (1987).

[32] J.C. Reviere, "*Surface Analytical Techniques*", Clarendon Press, Oxford, Chapter 20 (1990).

[33] K.W. Hipps and U. Mazur, "*Inelastic electron tunneling: an alternative molecular spectroscopy*", J. Phys. Chem. **97**, 7803 (1993).

[34] S. Reynolds and D.P. Oxley, "*Inelastic Electron Tunnelling Spectroscopy (IETS): Principles, Applications and Future Directions*", in "*Proceedings of the International School on Condensed Matter Physics*", ed. J.M. Marshall, World Scientific, Singapore, 209–217 (1997).

© 2012 Tous droits réservés.

---

[35] K. W. Hipps, and U. Mazur, "*Inelastic Electron Tunneling Spectroscopy*", from "*Handbook of Vibrational Spectroscopy*", Ed. by John M. Chalmers and Peter R. Griffiths: John Wiley & Sons Ltd, Chichester 2002.

[36] R. C. Jaklevic, and J. Lambe, "*Molecular vibration spectra by electron tunneling*", Phys. Rev. Lett. **17**, 1139 (1966).

[37] G. Binnig, N. Garcia, and H. Rohrer, "*Conductivity sensitivity of inelastic scanning tunneling microscopy*", Phys. Rev. B. **32**, 1336–38 (1985).

[38] J. D. Langan and P.K. Hansma, "*Can the concentration of surface species be measured with inelastic electron tunneling?*" Surf. Sci. **52**, 211–216 (1975).

[39] A. A. Cederberg, "*Inelastic electron tunneling spectroscopy: Intensity as a function of surface coverage*", Surf. Sci. **103**, 148 (1981).

[40] J. Kirtley, "*Inelastic Electron Tunneling Spectroscopy*", ACS Symp. Ser. **137**, 217 (1980).

[41] K.W. Hipps and A.T. Aplin, "*The tricyanomethanide ion: an infrared, Raman, and tunneling spectroscopy study including isotopic substitution*", J. Phys. Chem. **89**, 5459–5464 (1985).

[42] K.W. Hipps and U. Mazur, "*Vibrational and low-lying electronic transitions in tetraalkylammonium salts of tetrabromocobaltate(2-), tetrachlorocobaltate(2-) and tetrathiocyanatocobaltate(2-) as observed by Raman, IR and tunneling spectroscopies*",J. Phys. Chem. **91**, 5218–5224 (1987).

[43] J. Kirtley and P. Soven, "*Multiple-scattering theory of intensities in inelastic-electron-tunneling spectroscopy*", Phys. Rev. B **19**, 1812 (1979).

[44] J. Igalson and J.G. Adler, "*Effect of hydrogen-isotope implantation on aluminum oxide tunnel-junction barriers*", Phys. Rev. B **28**, 4970 (1983).

[45] S. Gauthier, S. de Cheveigne, J. Klein and M. Belin, "*Evidence for the formation of Al-H bonds in tunneling junctions*", Phys. Rev. B **29**, 1748 (1984).

[46] R.D. Ramsier, P.N. Henriksen and A.N. Gent, "*Adsorption of phosphorus acids on alumina*",Surf. Sci. **203**, 72–88 (1988).

[47] K.W. Hipps, S.D. Williams and U. Mazur, "*Forbidden vibrational modes in iron(II), ruthenium(II), and osmium(II) hexacyanides: a tunneling, IR, and Raman spectroscopy study*", Inorg. Chem. **23**, 3500–3505 (1984).

[48] K.W. Hipps and U. Mazur, "*An inelastic electron tunneling spectroscopy study of some iron cyanide complexes*", J. Phys. Chem. **84**, 3162 (1980).

[49] K. W. Hipps, and S. L. Peter, "*Line shape in normal metal tunneling spectroscopy*", *J. Phys. Chem.* **93***,* 5717–5721 (1989).

[50] K.W. Hipps and U. Mazur, "*Constant-resolution tunneling spectroscopy*", Rev. Sci. Instrum. **59**, 1903 (1988).

© 2012 Tous droits réservés.

---

[51] J. A. Stroscio, R. M. Feenstra, and A. P. Fein AP, "*Local state density and long-range screening of adsorbed oxygen-atoms on the GaAs(110) surface*", Phys. Rev. Lett. **58**, 1668–71 (1987).

[52] J. A. Stroscio, R. M. Feenstra, and A. P. Fein, "*Electronic-structure of the Si(111)2×1 surface by scanningtunneling Microscopy*", Phys. Rev. Lett. **57**, 2579–82 (1986).

[53] R. J. de Vries, A. Saedi, D. Kockmann, A. van Houselt, B. Poelsema, H. J. W. Zandvliet, "*Spatial mapping of the inverse decay length using scanning tunneling microscopy*", Appl. Phys. Lett. **92**,174101 (2008).

[54] K. Siegbahn, C. Nordling, A. Fahlman, R. Nordberg, K. Hamrin, J. Hedman, G. Johnsson, T. Bergmark, S. E. Karlsson, I. Lindgren, and B. Lindberg, Nova. Acta. Regiae. Soc. Sci. Ser. IV, **20** (1967); Nobel Prize in Physics "for his contribution to the development of high resolution electron spectroscopy", (1981).

[55] H. Hertz, Ann. Physik. **31**, 983 (1887); The IEEE Heinrich Hertz Medal was established by the Board of Directors in 1987 "for outstanding achievements in Hertzian (radio) waves."

[56] A. Einstein, Ann. Physik. **17**, 132 (1905); Nobel Prize in Physics "for his services to Theoretical Physics, and especially for his discovery of the law of the photoelectric effect", (1921).

© 2012 Tous droits réservés.

Chapter 3

Manipulating the charge state of a Si dangling bond

3.1. Introduction

The properties of semiconductor materials are strongly affected by impurities and point defects. These types of imperfections modify the chemical bonds, the crystalline structure, the lattice stability and also the atomic arrangement. Those defects also give rise to localized states that create electron trapping sites, which are empty or occupied depending on the electrochemical potential of the crystal. Understanding the change of charge state of a single point defect is crucial since it governs many important properties of materials, such as the conductivity [1, 2], color [3], chemical reactivity [4, 5], and the diffusion of atoms [6, 7]. The transport through single dopants in gated nanowires had been investigated [8]. With a STM tip, the charges which was induced on a small grain has been showed [9], also the charge switching on a single donor was reported [10]. Via the tip–induced decharging of the Mn acceptors in InAs, the influence of the manipulated charge on scanning tunneling spectra and the screened potential of the charged acceptor were introduced by Felix Marczinowski et al. [11]. The controlling of the charge state of individual gold atoms on insulator layers by adding or removing a single electron to or from the adatom with a STM tip has also been demonstrated [12].

A detail understanding of the charge state of single point defects is extremely important for improving the transport properties, optical properties of materials for the fabrication of electronic devices. However, knowing the Coulomb energy, U, is a challenge to overcome the problem of charge manipulation of a point defect. Due to the strong localization of the defect state and depending on the screening strength of the host materials, U can be in order of a few eVs [13]. Several techniques like deep level transient spectroscopy, capacitance measurements and optical experiments also allows the determination of the coulomb energy, but all of them probe the macroscopic properties of a sample and can not simultaneously characterize the nature of the point defects and measure the Coulomb interaction. It is true for the case of the

© 2012 Tous droits réservés.

Si dangling bond (DB), the major type of defects found in amorphous silicon and also at the Si/SiO_2 interface [14, 15, 16, 17].

In this chapter, we present a new method to measure the Coulomb energy of a point defect with the STM spectroscopy technique (STS) at low temperature (~ 5 K) in ultra high vacuum (~ 8×10^{-11} T). The thermal annealing of the highly B−doped Si(111) surface at high temperature results in a small residual concentration of defects holding an electronic state lying in the band gap of the semiconductor [18]. Although, high current, larger than few nano−Ampere, can be driven through this state. Injecting two electrons into the same state requires o overcome their Coulomb interaction. We will describe how the Coulomb energy can be measured and compose it to theoretical tight−binding calculations. This comparison will highlight the screening induced by the metallic tip.

3.2. The Si(111)−$\sqrt{3}\times\sqrt{3}R30^{\circ}$ −B surface

3.2.1. Reconstruction of the Si(111)−B surface

Si is known as the second most abundant chemical element on the earth's surface (after oxygen), but naturally Si is found in form of silicon dioxide SiO_2. But for devices applications, it must be purified and crystallized in order to get pure Si monocrystals.

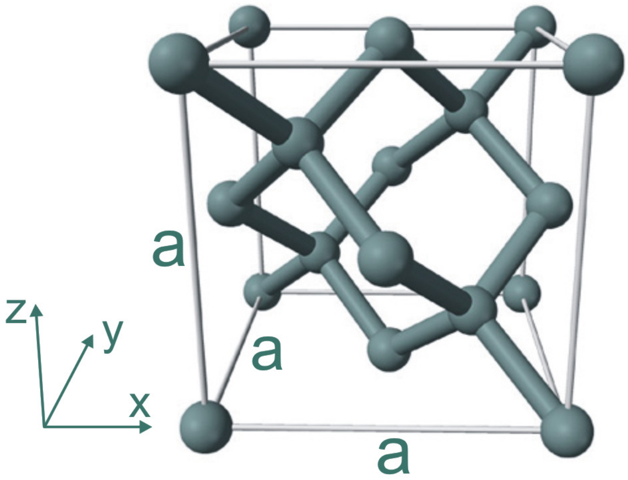

Figure 3.1: Crystalline Diamond structure of Silicon, that is made of two face-centered cubic (fcc) lattices.

© 2012 Tous droits réservés.

Crystalline silicon has a diamond structure, with a lattice parameter, a, of 543 pm, which is made of two intricated fcc lattices, one at the origin and the second shifted by $\left(\frac{a}{4},\frac{a}{4},\frac{a}{4}\right)$, as shown in Figure 3.1. Naturally, the cleaved (111) surface in Ultra High Vacuum (UHV) forms the 2×1 reconstruction [19, 20]. But this reconstruction is not stable at high temperature where it becomes the well-known 7×7 reconstruction which was imaged early by Bignnig et al. [21]. The 7×7 is the most common reconstruction of the Si(111) surface.

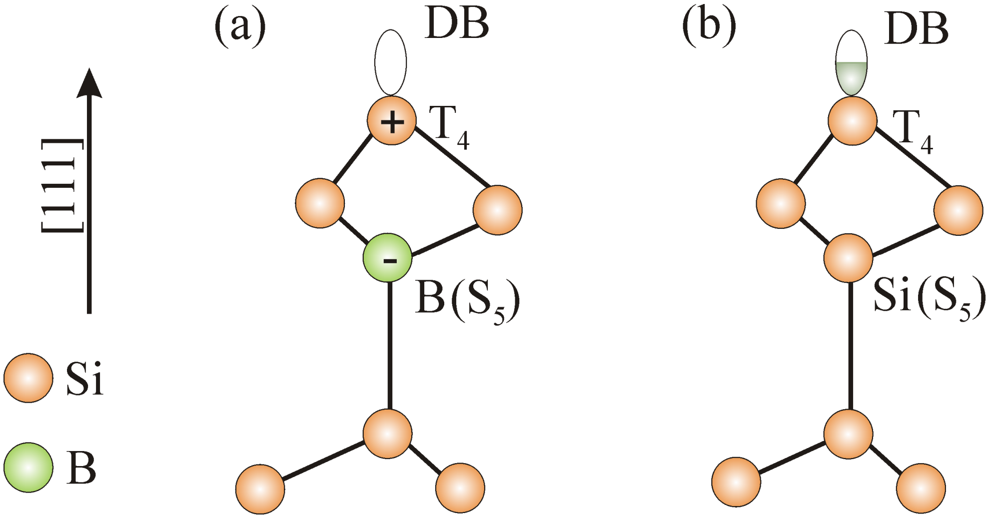

Figure 3.2: Atomic relaxation of Si adatom on $\sqrt{3}\times\sqrt{3}R30°$ *reconstruction surface. (a) a B atom occupies the* S_5 *position and the dangling bond state is empty, (b)* S_5 *is filled up with a Si atom and the dangling bond is partial with an electron.*

However, when Boron impurities are incorporated at a high concentration the surface structure turns into a $\sqrt{3}\times\sqrt{3}R30^{\circ}$ reconstruction which was firstly observed by RHEED [22]. When a B–doped silicon crystal is heated, the B impurities segregate and a majority of impurities stabilize in the subsurface layer at the substitutional position S_5 [23]. The surface has two main adsorption sites: a threefold hollow site H_3 and a threefold occupied site T_4, which is on top of the S_5 position. If Si adatoms adsorb at the T_4 position, a charge transfer from the Si adatoms to the substitutional B atoms occurs, making the last adatom DB (Dangling Bond) state passivated [16] (Figure 3.2a). Inversely, if the substitutional position S_5 is occupied by a Si atom, the DB is partially filled with an electron making the unpassivated state [16]. This is only true for the small clusters shown below. In fact, for the real surface, the electrons also leave the DB and recombine with a hole provided Boron impurities in the bulk. However,

© 2012 Tous droits réservés.

the electronic structure of both types of DB differs from each other. In the second one, the ground state related to the dangling bond is positioned in the band gap and will be discussed later.

3.2.2. Sample preparation

In our experiments, the sample is prepared by establishing a DC current through the sample for heating. The annealing process is automatically controlled by programming the temperature. This latter parameter is checked with a pyrometer as described below:

1. The B-doped Si(111) surface is heated gradually to 950 °C with a pressure kept lower than $5x10^{-10}$ *Torr*. This step will help in degassing the sample and removing the native oxide layer.

2. Since the Carbon atoms can make up to four covalent bonds, they are usually strongly bond to Si atom. Therefore, several flashes at around 1200 °C are done for 5 or 6 seconds to remove the Carbon contaminants.

3. After flashing the sample, the temperature is reduced to 950^{o} C and maintained there for several hours in order to allow the segregation of Boron dopants towards the surface. During this step, the number of substitutional Boron atoms at the S_5 sites can be tuned by well controlling the duration of this process.

4. Finally, the temperature is slowly decreased from 950 °C to 700 °C in about 2 hours to keep a sufficient adatom mobility during the reconstruction of the surface. After this step, the temperature is lowered at a faster rate.

The sample then is loaded into the STM chamber kept at the liquid helium temperature (5 K). A sharp clean Tungsten tip is used to scan the sample surface and the surface topography is recorded at constant current mode. In order to study the electronic configurations of the Si DB, tunneling spectroscopic measurements were performed with a lock-in amplifier.

3.2.3. Topographic image of the Si(111) $-\sqrt{3}\times\sqrt{3}R30^{\circ}$ –B surface

The segregation of B atoms at the temperature higher than 900 °C results in the

© 2012 Tous droits réservés.

replacement of Si atoms located just under the Si adatom position [16]. But for a few atomic sites the substitution does not take place, leading to the occurrence of bright adatoms in the empty state STM image of the surface [18]. Fig. 3.3(a) shows a large-scale constant–current image of the Si(111) $-\sqrt{3}\times\sqrt{3}R30^{\circ}$ –B surface (V_{bias} = + 1.5 V) where several types of defect are seen. Particularly, two isolated bright Si adatoms are visible and their contrasts extend up to region limited by the six first neighbors on the surface. Where as, a considerable number of dark atoms can be seen in Figure 3.3(a), those are related to the subsurface B dopants located at least 4 atomic layers below the surface [18].

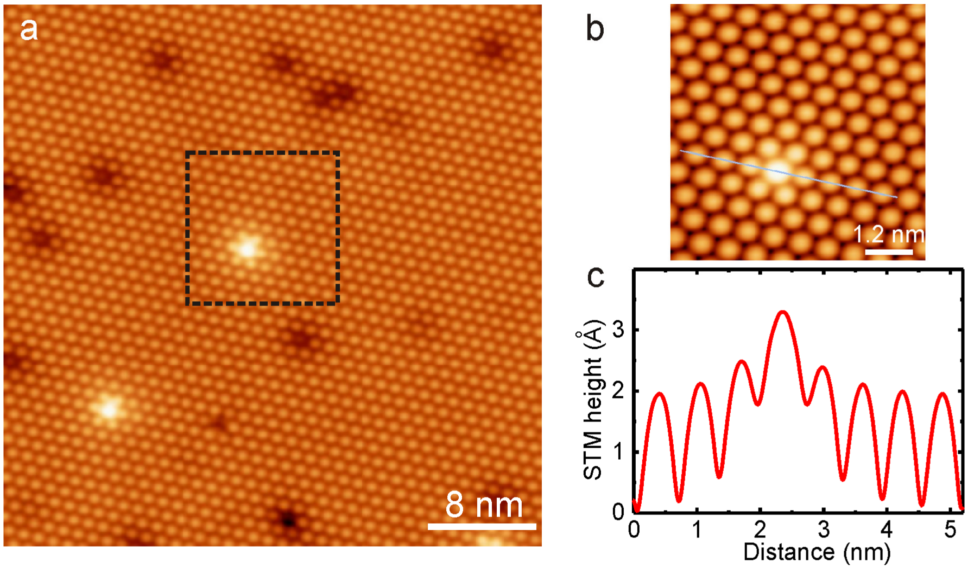

Figure 3.3: STM image of the Si(111)–$\sqrt{3}\times\sqrt{3}R30^{O}$ -B surface at 5 K. (a) Large scale image where adatoms are clearly seen. Most of them have the same contrast and correspond to Si adatoms with a Boron atom underneath. In contrast, two Silicon adatoms appear much brighter and correspond to the configuration with a Si atom underneath (V_{bias} = +1.5 V and I_{set} = 1.8 nA). (b) higher magnified view of a bright Si adatom and (c) profile curve along the line denoted in (b).

The brighter adatom is seen more clearly in Fig. 3.2(b). Its contrast was explained to arise from the localized state of the DB that is positioned in the Si band gap [18]. The height profile curve in Fig. 3.3(c) shows the difference in height between a Si adatom and one of the first six neighbors and a bare Si atom on Si(111)-$\sqrt{3}\times\sqrt{3}R30^{\circ}$ –B reconstruction. The average difference in height of approximate 1 Å and 0.6 Å are found between a DB and one of the first six neighbors with a passivated Si adatom far from the bright adatom respectively. Those values are consistent with the ones reported by I.-. Lyo et al. [16].

© 2012 Tous droits réservés.

3.3. Coulomb energy determination of a single Si dangling bond

3.3.1. Tunneling spectroscopic measurements of a Si adatom

In order to study the electronic configurations of the Si DB, tunneling spectroscopic measurements were carried out with a lock-in amplifier. As shown in Fig. 3.4(a), three types of tunneling differential conductance spectra have been acquired:

(i). On a bright adatom.

(ii). On one of the six first neighbors.

(iii). On a passivated Si adatom positioned a few nanometers away from a bright adatom.

It is easy to recognize dissimilarities between the three dI/dV curves, although all curves were performed at the same setpoint current of 0.6 nA and with the same parameters used for lock–in amplifier (V_{mod} = 6 mV$_{\text{p-p}}$, f_{mod} = 495 Hz). On a bare Si atom located a few nanometer away from a bright adatom [curve (iii)], the curve shows a large region without signal that extends up to +1.11 V. This onset corresponds to the the position of the conduction band edge E_C. Indeed, the bulk is p–type doped with Fermi level lying 100 meV below the valence band edge [24]. Above E_C, a peak exists and has been attributed to the empty state of the DB due to the capture of electron by the subsurface B atoms. Therefore, the zero conductance zone in curve (iii) corresponds to the band gap of passivated Si atom. In curve (i), measured on a bright Si adatom, a prominent peak occurs and is followed by a negative peak at a higher voltage. Both peaks are positioned in the Si band gap revealing a negative differential resistance (NDR) behavior. The linewidth of the peaks is related to the strong excitation of the vibrational states [18], the first vibronic state being already observed in the dI/dV curve at the upward edge of the positive peak.

Interestingly, the tunneling spectroscopic measurements performed on the six first adatom neighbors of a bright adatom [curve (ii)] show one peak positioned just below the conduction band edge. This peak, centred at +1.05 V, has a sharp linewidth, which was found to be limited by the amplitude of the modulation. The smallest linewith that was found to be 3 meV. It contrasts with the broad peak observed on a bright adatom. This difference could be seen more clearly by mapping out the electron density at the energies of the positive broad peak and the sharp peak. Fig. 3.4(c) and 3.4(d) shows

© 2012 Tous droits réservés.

the dI/dV conductivity maps measured at $V_S = +0.5V$ and $+1.5V$, respectively. The spatial extent of the square of the wave function related to both states is quite different. The electronic state corresponding to the broad peak is strongly localized on the bright adatom in agreement with the radius expected for a deep bound state [25], while the state related to the sharp peak radially extends over a few atomic sites around the bright adatom.

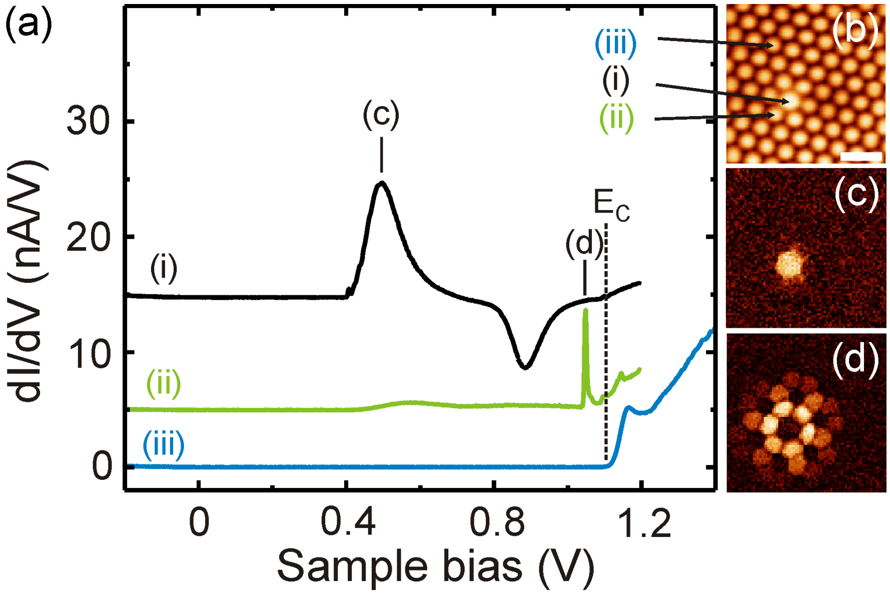

Figure 3.4: (a) Tunneling differential conductance spectra measured on (i) a non passivated bright Si adatom with empty dangling bond, (ii) one of its six first neighbours and (iii) a passivated Si adatom, as indicated in (b). The spectra were measured at a setpoint current of 0.6 nA (V_{mod} = 6 mV_{p-p}, f_{mod} = 495 Hz). The conduction band edge is labelled E_C. (b-d) Spatially resolved tunneling spectroscopic measurements obtained on a bright adatom: (b) topographic image (sample voltage V_s = +1.60 V, tunneling current I_t = 3.0 nA, scale bar 1 nm), (c) and (d) dI/dV conductivity maps measured at V_s = +0.50 V and +1.05 V respectively.

3.3.2. Electronic structure of a positively charge Si DB

The origins of the peaks observed in Figure 3.4 are explained as follows: due to the high concentration of Boron acceptors in the sample (resistivity of 1 mΩ.cm), the Fermi level is positioned at the top of the valence band. Therefore, the DB is positively charged (*n=0*) (here *n* implies the number of electron) until an electron is transferred from the tip, resulting in a neutral DB (*n=1*). The broad peak thus corresponds to the (+/0) transition level [Figure 3.5(a)]. As mention in the experiment of Fig. 3.4, the intensity of the current transferred through the DB is much smaller than the intensity required to saturate the current [18]. Thus, the DB remains positively

© 2012 Tous droits réservés.

charged on average. It induces a screened Coulomb potential that attracts a hydrogenic–like state below the conduction band edge. From the wave function mapping in Fig. 3.4(d), it shows clearly that the weight of the wave function for this state, related to the sharp peak, is zero at the position of the bright adatom. Hence, this wave function is orthogonal to the ground state of the neutral DB. For that reason, the sharp peak is identified as the level (+/0*) for the transition from the positive charge state to the first excited state of the neutral DB [Figure 3.5(a)].

The sharp linewidth of the peak is consistent with a state that can not couple to the main vibrational mode of the Si adatom, because the wave function is zero at the position of the Si adatom. Additionally, its localization is consistent with the spatial extent of 3 to 5 nm of shallow levels measured by tunneling spectroscopy of subsurface donor and acceptor in other semiconductor surfaces with similar dielectric constants [26, 27].

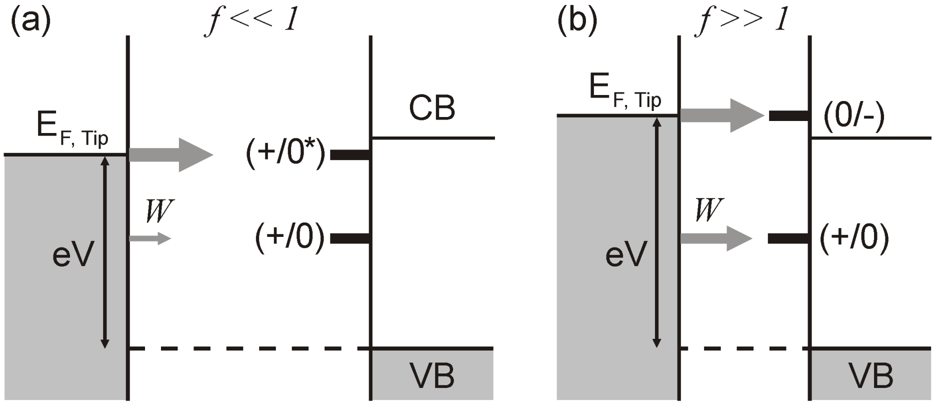

Figure 3.5: Available electronic states of a non passivated dangling bond as a function of the occupation probability f. (a) At large tip-sample distances, f is small and the dangling bond (DB) is empty and thus positively charged on average. When the tip Fermi level is close to the conduction band (CB) edge, the DB ground state and first excited state contribute to the tunneling current giving rise to the transitions (+/0) and (+/0) respectively. (b) At small tip-sample distances, f is close to 1 and the DB ground state is continuously occupied. The degeneracy of the DB ground state is lifted and electrons are transferred when the tip Fermi level becomes resonant with the transition level (0/−). The tunneling rates through the different states are indicated by arrows and the rate through the DB ground state is labelled W. The valence and conduction bands, tip Fermi level, sample bias and effective intra-atomic Coulomb repulsion energy are respectively labelled VB, CB,* $E_{F,Tip}$*, V.*

3.3.3. Occupation probability

By increasing the setpoint current, the current intensity transferred through (+/0) increases and finally becomes saturated. Such behaviour is clearly seen in Fig. 3.6,

© 2012 Tous droits réservés.

where, for the DB studied in this case, the saturation of the inelastic current through (+/0) is measured for a current setpoint of 35 nA. The current through (+/0) is expressed in permanent regime as [28]:

$$I_{(+/0)} = -e\left(1-f\right)W \qquad (3.1)$$

where W is the tunneling rate between the tip and the DB, and f is the occupation probability of the DB state. The transport through a DB's non resonant ground state is demonstrated to be a two–process that involves the tunneling of an electron from a tip state to the DB state and, then, non–radiative recombination of the electron with a hole from the valence band [18]. Hence, as I must be equal to the current generated from the capture of hole by the DB, we obtain from the intensity at saturation:

$$f = I_{(+/0)} / I_{Max} \qquad (3.2)$$

with $I_{Max} = -ec_p p$, c_p is the hole capture coefficient of the DB and p is the hole concentration, respectively [25].

Experimentally, I_{Max} is determined by searching for the value at saturation of the tunneling current measured at the energy of the transition level (+/0). From the set of tunneling current spectra shown in Figure 3.6 measured at sample bias of +1.6 V, the value of the intensity at saturation is around 23.7 nA. by measuring the intensity of the current transferred through the DB for each setpoint current allows plotting the variation of f , as displayed in the inset of Fig. 3.6. When the tip–sample distance is large, W is small in comparison with $c_p p$ and f is close to zero, corresponding to a predominantly positively charged DB. Conversely, when W is higher than $c_p p$, f is close to unity and the DB is continuously occupied with one electron. In this regime, the transfer of the second electron into the DB should give rise to a second peak (0/−) which is separated from (+/0) by the screened electron–electron interaction estimated in the range from 0.2 to 1.2 V, depending on the environment of the Si DB [29, 30]. Nevertheless, no additional peak is visible at high setpoint currents between 0.8 and 1.6 V in Fig. 3.6.

Interestingly we notice that the tunneling current decreases once the tip Fermi level is higher than the level (+/0), measured at V_s=0.79 V for a setpoint current of 35 nA [Fig. 3.6]. Such effect occurs because the electrons resonantly tunnel at the energy of (+/0) and the probability of transmission is strongly peaked near the Fermi level of

© 2012 Tous droits réservés.

the tip [31]. Once the tip Fermi level becomes higher than the transition level (+/0), the probability transmission decreases resulting in a smaller current. This reduction of current explains the observed negative differential resistance (NDR). Consequently, the condition that the DB is continuously filled with one electron is never fulfilled when the tip Fermi level is higher than (+/0). In this respect, tunneling through (0/−) is unlikely to occur unless the current at saturation is maintained constant for energies above (+/0).

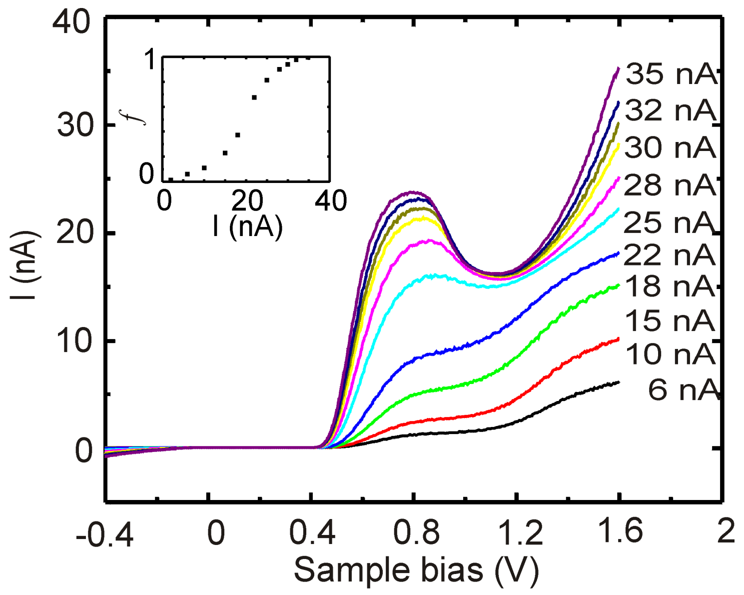

Figure 3.6: Tunneling current spectra measured on a non passivated bright Si adatom for different setpoint currents at a sample voltage $V_S = +1.6$ V. Inset: Measured variation of the occupation probability f with respect to the tunneling current setpoint.

However, the dependence of the transmission probability on energy for transferring an electron through a single energy level that is weakly coupled to the leads generally results in a reduction of the tunneling rate for energies above the DB ground state [32]. Therefore, the occupation probability of the DB can not be kept constant when the sample voltage increases, preventing the defect from changing its charge state.

3.3.4. Transition from the neutral DB to the negative charge state

To circumvent the mentioned limitation in the section 3.3.3, spectroscopic measurements have been performed with closed feedback loop. In this “mode”, the tunnelling current remains constant by changing the tip height to cancel any decrease

© 2012 Tous droits réservés.

of W, while the tip Fermi level is shifted above (+/0) (see Figure 3.7(a)). As a result, the tip retracts as the voltage increases (as shown in Figure 3.7(b)). In these conditions, if the current set–point corresponds to the current required to saturate the empty DB, there is a continuous occupation of the DB with one electron preventing the injection of an electron through (+/0*) (first excited state of the neutral DB) when the tip Fermi level become aligned with this level. This behaviour can be clearly seen in the variation of the (+/0*) intensity with respect to the tunnelling current setpoint when measured on the first neighbours of the bright adatoms.

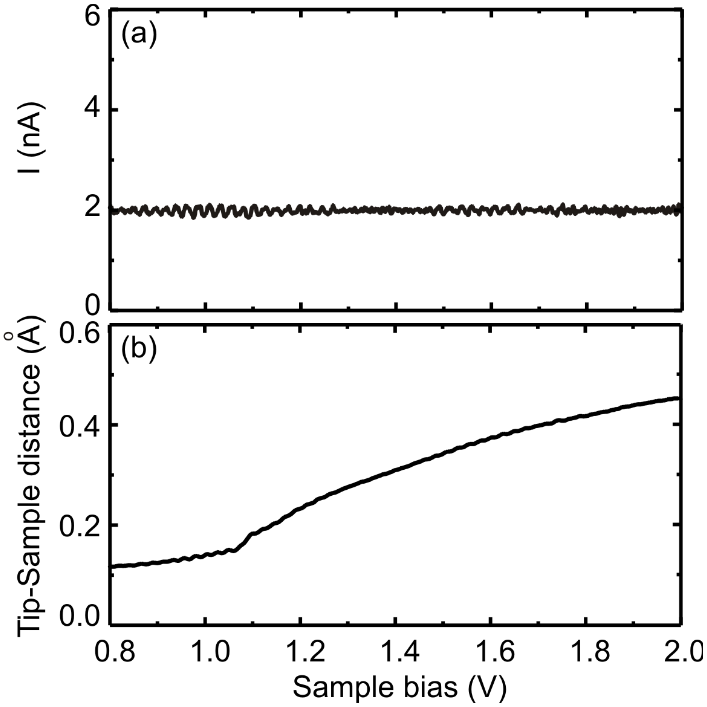

Figure 3.7: Tunneling spectroscopy at constant current, also called the constant tunneling current (a) and the variation of tip–sample distance Z(V) (b) versus the sample bias V measured on one of the first six neighbors of a bright adatom with closed feedback loop.

Figure. 3.8 gives an example of such measurements performed on one of the six first neighbours of a bright adatom. The constant-current differential conductance is measured at a frequency higher than the cut-off frequency of the feedback loop (the frequency level above which the feedback loop operates ineffectively). Whatever the tunnelling setpoint current is, the current could be kept constant between 0.8 and 1.0 V, due to the tunnelling of electrons into the tail of the DB ground state. At small tunnelling setpoint currents, a step and a sharp peak are clearly visible in the $Z(V)$ and dI/dV spectra, respectively, this peak corresponds to electron tunnelling into the

© 2012 Tous droits réservés.

(+/0*) level. With the increase of tunnelling setpoint currents, the step in the $Z(V)$ curve quickly disappears and is replaced by a smoother step that is attributed to the edge of the conduction band (Figure 3.8). In the dI/dV spectra, the peak related to (+/0*) is still resolved, but its intensity decreases. Such decrease is consistent with an increase of the occupation probability of the DB, preventing the excited states from being further filled. For a setpoint current of 22 nA, a new downward step emerges below +1.4 V in the dI/dV curve.

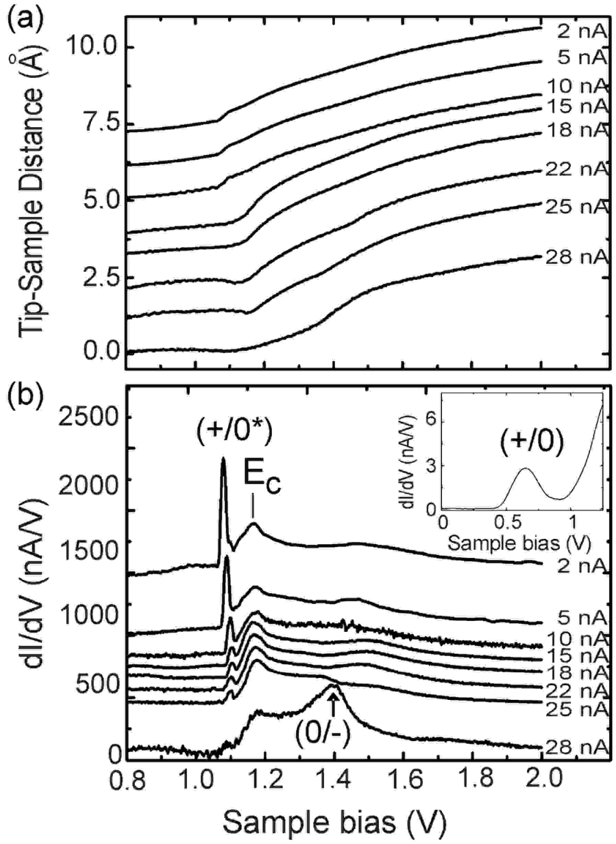

Figure 3.8: Spectroscopic measurements performed on the first neighbour of a non passivated bright Si adatom for different tunneling setpoint currents. The feedback loop was maintained close to keep the tunnel current constant and thereby filling continously the DB ground state even at larger voltages. Variation of (a) the tip sample distance and (b) the differential conductance as a function of the sample voltage. The peaks labelled (+/0), (+/0*), (0/-) and E_c respectively correspond to the transition from the positive charge state to the ground state of the neutral DB, the transition from the positive charge state to the first excited state of the neutral DB, the transition from the neutral DB to the second electron excitation of the ground state and the bottom of the conduction band. The frequency of the lock-in amplifier was set at 2.0 kHz. The spectra were averaged, except for the data corresponding to I_t = 10nA, where a single curve was acquired. Inset : Tunneling differential conductance spectrum measured on the non passivated bright Si adatom with the feedback switched off to measure the energy transition (+/0) (V_S = +1.6 V, I_t = 2 nA).

© 2012 Tous droits réservés.

For I_t = 28 nA, this step turns into a strong peak, while the signal becomes more noisy for the voltages below this peak. We attribute this peak to the transition (0/−) that is centred at the sample bias of 0.65 V. From the inset of Figure 3.7(b), showing the position of (+/0), measured with the feedback open, we deduce:

$$\Delta E = (0/-) - (+/0) = 0.75\, eV \tag{3.3}$$

3.3.5. Coulomb repulsion in the DB

In case the DB is occupied by n electrons, the total energy is written as in Ref. 30:

$$E(n,Q) = n\varepsilon_o + \frac{Un^2}{2} - F_n(q-Q) + \frac{k}{2}(q-Q)^2 \tag{3.4}$$

where q is the configuration coordinate for the displacement of the DB and Q is the coordinate where the energy of the oscillator is the lowest, ε_o is the bond energy of the tetrahedral hybrid without distortion, k is the stiffness of the oscillator and F_n is the force induced by n electrons on the DB state (by convention, $F_0 = 0$ and $F_1 = F$). The level (0/−) being resonant in the CB, we assume that there is no supplementary force ($F_2 = F$) when a second electron is injected in the DB state due to its short lifetime. Indeed, the full width at half maximum (110 meV) of the (−/0) resonance is large compared to the vibration energy of the DB (30 meV [18]) and such linewidth suggests a strong coupling with the states of the conduction band. Following Huang–Rhys theory in the strong electron–vibration coupling regime [33], the energy of the tunneling peak maximum related to the first transition level is given by (See Figure 3.9):

$$E(+/0) = E(1,Q_0) - E(0,Q_0) \tag{3.5}$$

where Q is the minimum of the oscillator when an electron resides in the dangling bond. From Equation (3.4), $E(1,Q_0)$ and $E(0,Q_0)$ can be written as:

$$E(0,Q_0) = -F_n(q-Q_0) + \frac{k}{2}(q-Q_0)^2 \tag{3.6a}$$

© 2012 Tous droits réservés.

and

$$E\left(1,Q_0\right)=\varepsilon_0+\frac{U}{2}-F\left(q-Q_0\right)+\frac{k}{2}\left(q-Q_0\right)^2 \tag{3.6b}$$

Combining (3.5), (3.6a) and (3.6b), we have:

$$E\left(+/0\right)=\varepsilon_0+\frac{U}{2} \tag{3.7}$$

The energy of the tunneling peak corresponding to the transition level from the neutral charge state to the negative charge state of the DB is given by:

$$E\left(0/-\right)=E\left(2,Q_1\right)-E\left(1,Q_1\right) \tag{3.8}$$

Based on Equation (3.4), we have:

$$E\left(2,Q_1\right)=2\varepsilon_0+2U-F\left(q-Q_1\right)+\frac{k}{2}\left(q-Q_1\right)^2 \tag{3.9a}$$

and

$$E\left(1,Q_1\right)=\varepsilon_0+\frac{U}{2}-F\left(q-Q_1\right)+\frac{k}{2}\left(q-Q_1\right)^2 \tag{3.9b}$$

Substracting equation (3.9a) to equation (3.9b), we get:

$$E\left(0/-\right)=\varepsilon_0+\frac{3U}{2} \tag{3.10}$$

From (3.7) and (3.10), the energy difference between (+/0) transition and (0/−) transition is determined:

© 2012 Tous droits réservés.

$$\Delta E = E(0/-) - E(+/0) = U \qquad (3.11)$$

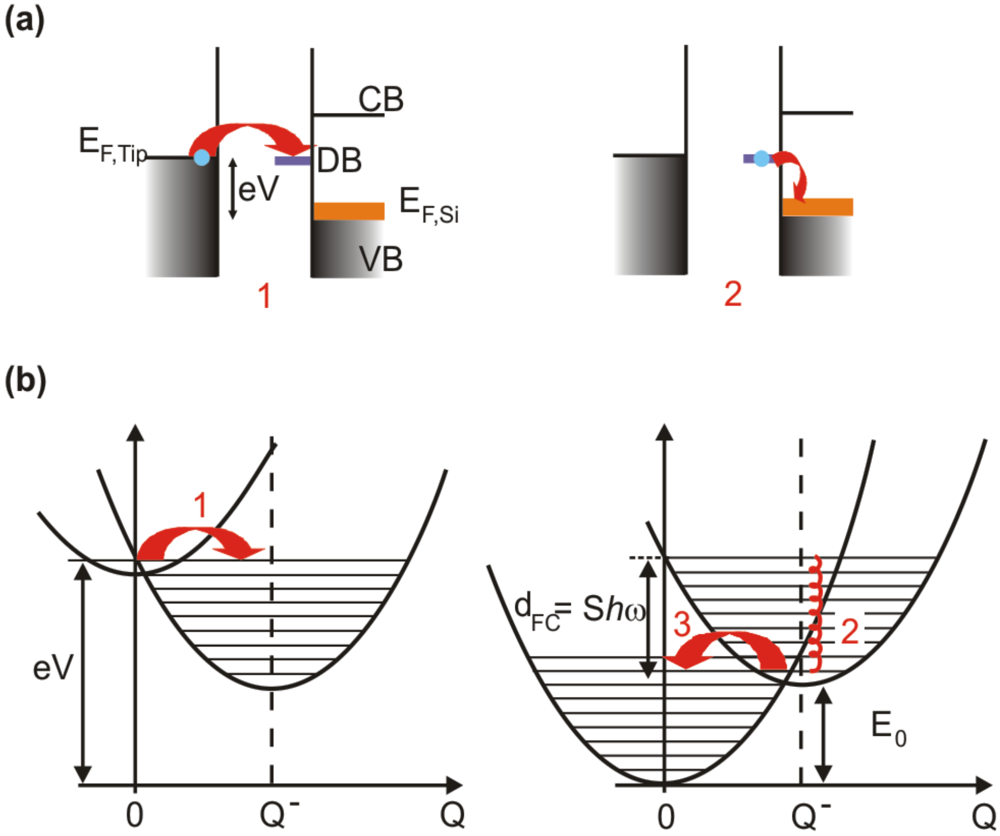

Figure 3.9: (a) Energy diagrams sketching the two–step transport process: (1) the energy, eV, of the electron in the tip is tuned via the STM bias voltage, to become resonant with the dangling–bond state (DB) at a given vibrational state; (2) when sufficient energy has been transferred to the adatom, the probability of nonradiative transfer of a hole from the partially empty band of Boron impurities becomes high enough. The conduction and valence bands are, respectively, labeled by CB and VB, the tip and silicon Fermi levels by $E_{F,Tip}$ and $E_{F,Si}$. (b) Total energy curves as a function of the vibrational coordinate, Q, of the dangling-bond. On the left graph (process 1), the adatom in its ground state (top parabola) changes its charge state and its total energy corresponds to the bottom parabola, centered at $Q = Q_0$. On the second diagram, the adatom in the excited state (top parabola) may dissipate up to S quanta of vibration of energy $\hbar\omega$, corresponding to the Franck-Condon shift d_{FC} (process 2). Finally, the electron is transferred into the degenerated band of Boron impurities, leaving the adatom in a vibrationally excited state about its initial position (process 3); E_0 is the ionization energy [18].

Using the simple electrostatic arguments, a Coulomb charging energy U = 1.2 eV has been estimated for a DB at a free Si surface [30]. Our measured value (~0.75 eV) is smaller. This reduced value could be caused by the screening of the metallic tip. To check that hypothesis, we performed self-consistent tight binding calculations on spherical Si nanocrystals. In this method, one DB has been introduced at the

© 2012 Tous droits réservés.

nominally hydrogen passivated surface and the variation of the DB energy upon addition of a charge was calculated. The tight binding method provides a very good description of the dielectric screening and allows studying non–periodic (to avoid long-range interactions) systems containing up to 1700 atoms (diameter of ~4 nm). The Hamiltonian is written as $H = H^0 + W$ where H^0 is the bare Hamiltonian parameterized in Ref. 34 and W is the potential induced by the variation of charges in the system. Since the potential is slowly variable, only the diagonal matrix elements of W are considered: on an atom i, W_{ii} is given by $-e\sum_j V_{ij}$ where V_{ij} is the potential caused by the charge q_j on the atom j. For an isolated nanocrystal, V_{ij} is simply equal to q_j/R_{ij} with R_{ij} is the distance between the two atoms ($V_{ii} = v_0 q_i$ where $v_0 = 10.6$ V represents the intra-atomic interaction [35, 36]). The Hamiltonian matrix is diagonalized and the net charge on each atom is deduced from the occupied states. The problem is solved iteratively until self–consistency, for two charge states of the DB (see Figure 3.9).

The influence of the tip is simulated by a metallic plane perpendicular to the surface and lying at 1 nm from the DB. The metallic plane is described by the image charge method, i.e. $V_{ij} = q_j\left(1/R_{ij} - 1/R'_{ij} \right)$ where R'_{ij} is the distance from the atom i to the image of the atom j with respect to the metallic plane. In all the cases, we obtain that the charging energy varies like $U_0 + b/R$ where R is the nanocrystal radius. The term b/R comes from the uncomplete screening in the finite system [35] and U_0 is the charging energy in the limit $R \to \infty$. For an isolated nanocrystal, we obtain b=1.44 eV.nm and U_0=1.12±0.06 eV, confirming previous estimations [30]. In presence of a tip, we get b=1.29 eV.nm and U=0.82±0.06 eV, in good agreement with the experimental value of 0.75 eV.

3.4. Conclusion

In summary, in this chapter the correlation effects in a single atomic orbital have been studied. By performing tunneling spectroscopic measurements where the voltage dependence of the transmission probability is cancelled, the transition from the shell-tunneling regime to the shell-filling regime of a Si DB on a B-doped Si(111) $\sqrt{3}\times\sqrt{3}R30^{\circ}$ surface has been analyzed. We emphasize that this method can be applied to a wide range of quantized system from single atoms and molecules to inorganic nanostructures. It is a prerequisite to ascertain that correlation effects occur when tunneling spectroscopic measurements are performed and it should be quite helpful to discriminate the electronic states probed by STM on individual semiconductor nanocrystals.

© 2012 Tous droits réservés.

References

---

[1] W. Shockley and W. T. Read, "*Statistics of the Recombinations of Holes and Electrons*", Phys. Rev. 87, 835–842 (1952).

[2] J. –Hao. Chen, W. G. Cullen, C. Jang, M. S. Fuhrer, and E. D. Williams, "*Defect Scattering in Graphene*", Phys. Rev. Lett. **102**, 236805 (2009).

[3] R. M. Sheetz, I. Ponomareva, E. Richter, A. N. Andriotis, and M. Menon, "*Defect-induced optical absorption in the visible range in ZnO nanowires*", Phys. Rev. B **80**, 195314 (2009).

[4] T. Mitsui, M. Rose, E. Fomin, D. Ogletree, and M. Salmeron, "*Dissociative hydrogen adsorption on palladium requires aggregates of three or more vacancies*", Nature **422**, 705 (2003).

[5] T. König, G.H. Simon, H.-P. Rust, M. Heyde, and H.-J. Freund, "*Measuring the Charge State of Point-defects on MgO/Ag(001)*", J. Am. Chem. Soc. **131**, 7544 (2009).

[6] P. M. Fahey, P. B. Griffin, and J. D. Plummer, "*Point defects and dopant diffusion in silicon*", Rev. Mod. Phys. **61**, 289 (1989).

[7] U. Kaiser, D.A. Muller, J.L. Grazul, A. Chuvilin and M. Kawasaki, "*Direct observation of defect-mediated cluster nucleation*", Nature Materials **1**, 102 - 105 (2002).

[8] H. Sellier, G. P. Lansbergen, J. Caro, S. Rogge, N. Collaert, I. Ferain, M. Jurczak, and S. Biesemans, "*Transport Spectroscopy of a Single Dopant in a Gated Silicon Nanowire*", Phys. Rev. Lett. **97**, 206805 (2006).

[9] Jascha Repp, Gerhard Mayer, Fredrik E. Olsson, and Mats Person, "*Controlling the Charge State of Indivual Gold Adatoms*", Science **305**, 493 (2004).

[10] K. Teichmann, W. Wenderoth, S. Loth, R. G. Ulbrich, J. K. Garleff, A. P. Wijnheijmer, and P. M. Koenraad, "*Controlled Charge Switching on a Single Donnor with a Scanning Tunneling Microscope*", Phys. Rev. Lett. **101**, 076103 (2008).

[11] Felix Marczinowski, Jens Wiebe, Focko Meier, Katsushi Hasimoto, and Roland Wiesendanger, "*Effect of charge manipulation on a scanning tunneling spectra of single Mn acceptors in InAs*", Phys. Rev. B **77**, 115318 (2008).

[12] J. Repp, G. Meyer, F. Olsson, M. Persson, "Controlling the Charge State of Individual Gold Adatoms", Science **305**, 493 (2004).

© 2012 Tous droits réservés.

---

[13] M. Lannoo, C. Delerue, and G. Allan, "*Screening in Semiconductor Nanocrystallites and Its Consequences for Porous Silicon* ", Phys. Rev. Lett. **74**, 3415 (1995).

[14] W. Futako, N. Mizuochi, and S. Yamasaki, "*In situ ERS Observation of interface Dangling Bond Formation Processes During Ultrathin* SiO_2 *Growth on Si(111)*", Phys. Rev. Lett. **92**, 105505 (2004).

[15] Takahide Umeda, Masayasu Nishizawa, Tetsuji Yasuda, Junichi Isoya, Satoshi Yamasaki, and Kazunobu Tanaka, "*Electron Spin Resonance Observation of the Si(111)-(7×7) Surface and Its Oxidation Process*", Phys. Rev. Lett. **86**, 1054 (2001).

[16] I.−W. Lyo, E. Kaxiras, and Ph. Avouris, "*Adsorption of boron on Si(111): Its effect on surface electronic states and reconstruction*", Phys. Rev. Lett. **63**, 1261, (1989).

[17] P. Gupta, C. H. Mak, P. A. Coon, and S. M. George, "*Oxidation kinetics of Si(111) 7×7 in the submonolayer regime*", Phys. Rev. B **40**, 7739 (1989).

[18] M. Bethe, A. Urbieta, L. Perdigão, B. Grandidier, D. Deresmes, C. Delerue, D. Stiévenard, R. Rurali, N. Lorente, L. Magaud, and P. Ordejón, "*Electron Transport via Local Polarons at Interface Atoms*", Phys. Rev. Lett. **97**, 206801 (2006).

[19] K. C. Pandey, "*New* π*−Bonded Chain Model for Si(111)−(2×1) Surface*", Phys. Rev. Lett. **47**, 1913 (1981).

[20] J. E. Nothrup, and M. L. Cohen, "*Reconstruction Machanism and Surface−State Dispersion for Si(111)−(2×1)*", Phys. Rev. Lett. **49**, 1349 (1982).

[21] G. Binnig, H. Rohrer, CH. Gerber, and E. Weibel, "*7×7 Reconstruction on Si(111) Resolved in Real Space*", Phys. Rev. Lett. **50**, 120-123 (1983).

[22] H. Hirayama, T. Tatsumi, and N. Aizaki, "*Reflection high energy electron diffraction and Auger electron spectroscopic study on B/Si(111) surface*", Surf. Sci. **193**, 47 (1988).

[23] H. Q. Shi, M. W. Radny, and P. V. Smith, "*Electronic structure of the Si(111)* $\sqrt{3}\times\sqrt{3}R30^{\circ}$ *-B surface*", Phys. Rev. B **66**, 085329 (2002).

[24] C. Tournier−Colleta, "*Study the electron spectroscopy at the metal−semiconductor interface*", Thesis at the University of Nancy (2011).

[25] M. Berthe, R. Stiufiuc, B. Grandidier, D. Deresmes, C. Delerue, and D. Stivénard, "*Probing the Carrier Capture Rate of a Single Quantum Level*", Science **319**, 436 (2008).

[26] A. P. Wijinheijmer, J. K. Garleff, K. Teichmann, M. Wenderoth, S. Loth, E. G. Ulbrich, P. A. Maksym, M. Roy, and P. M. Koenraad, "*Enhanced Donor Binding Energy Close to a Semiconductor Surface*", Phys. Rev. Lett. **102**, 166101 (2009).

[27] G. Mahieu, B. Grandidier, D. Deresmes, J. P. Nys, D. Stiévenard, and P. Ebert, "*Direct evidence for*

© 2012 Tous droits réservés.

---

shallow acceptor states with nonspherical symmetry in GaAs", Phys. Rev. Lett. **94**, 26407 (2005).

[28] X. de la Broise, C. Delerue, M. Lannoo, B. Grandidier, and D. Stiévenard, "*Theory of scanning tunneling microscopy of defects on semiconductor surfaces*", Phys. Rev. B **61**, 2138 (2000).

[29] Y. Bar-Yam and J. D. Joannopoulos**,** "*Dangling Bond in a-Si:ZZH*", Phys. Rev. Lett. **56**, 2203–2206 (1986).

[30] M. Lannoo, P. Fridel, "*Atomic and electronic structure of surfaces*" (Springer varlag, Berlin, 1991).

[31] I.-W. Lyo, and Ph. Avouris, "*Negative Differential Resistance on the Atomic Scale: Implications for Atomic Scale Devices*", Science **245**, 1369 (1989).

[32] R. M. Feenstra, J. A. Stroscio, and A. P. Fein, "*Tunneling Spectroscopy of the Si(111)2×1 Surface*", Surf. Sci. **181**, 295 (1987).

[33] K. Huang, and A. Rhys, "*Theory of Light Absorption and Non-Radiative Transitions in F-centre*", Proc. R. Soc. London, Ser. A **204**, 406 (1950).

[34] Y. M. Niquet, D. Rideau, C. Tavernier, H. Jaouen, and X. Blase, "Model for the on-site matrix elements of the tight-binding hamiltonian of a strained crystal: Application to silicon, germaniumand their alloys", Phys. Rev. B **79**, 245201 (2009).

[35] C. Delerue, M. Lannoo, and G. Allan, "*Concept of dielectric constant for nanosized systems*", Phys. Rev. B **68**, 115411 (2003).

[36] C. Delerue, M. Lannoo, and G. Allan, "*Calculations of the electron energy loss spectra of silicon nanostructures and porous silicon*", Phys. Rev. B **56**, 15306 (1997).

© 2012 Tous droits réservés.

© 2012 Tous droits réservés.

http://doc.univ-lille1.fr

Chapter 4

Bipolar transport in PbSe nanocrystals with partial CdSe shell

4.1. Introduction

The exceptional properties of semiconductor QDs or NCs, like: high efficiency, tunable electronic properties, narrow luminescence, blueshift of the optical band gap…, make them attractive for various applications, such as: biolabeling when used as LEDs (Light Emitting Diodes) [1] and single–electron tunneling devices [2]. However, applications related to light emission have been limited partially due to the intermittent quenching of their photoluminescence which makes them turning on or off randomly [3] at no particular timescales [4]. The fundamental mechanisms of this behaviour is assumed to be caused by extra charges in the nanocrystal that enhance greatly the non–radiative decay rates [5, 6]. These charges arise from the separation of photoexcited electron–hole pairs, and are long–lived, as one charge carrier from the pair probably resides at the nanocrystal surface in deep–trap energy states [3, 7, 8].

Similarly, measurements of the tunneling current acquired on top of a single semiconductor QDs placed in a double barrier tunneling junction also exhibited noise, which was attributed to the fluctuations of charge in the NCs environment [9]. Great efforts have been done in order to reduce the trapping of charge carriers on the surface of the NCs and the growth of a shell layer around the NCs has been considered as an effective solution [10, 11]. With the appearance of a shell as a protecting layer of NC core the continuous photoluminescence has been found [7], also the addition of the shell results in the formation of heterostructures, where the localization of charge carriers may be significantly modified with respect to the core only [12, 13, 14, 15]. As a good control over the optical properties of heterostructured NCs is required, the knowledge of the carrier localization in the heterostructured NCs implies thorough studies of their electronic structure.

A prototypical case concerns PbSe NCs that emit in the infrared range and suffer from a reduction of the quantum yield with time as a consequence of surface oxidation of the NC [16]. By capping the core with a CdSe shell, it has been shown that the brightness stability of the core–shell NCs increases [17]. But the origin of the optical transitions is not still well understood [18]. In this chapter, we study the electronic

© 2012 Tous droits réservés.

structure of PbSe/CdSe core/shell NCs by mean of scanning tunneling spectroscopy (STS) at low temperature. Tunneling spectroscopy on these systems is based on resonant tunneling across a double–barrier tunneling junction [19, 20]. So far, most of the tunneling experiments have dealt with asymmetric junctions, where the tip–NC distance was larger than the NC–substrate distance, giving access to the quasi–particle band gap of the NCs and to the energy separation between the lowest quantized levels of the conduction band (CB) and valence band (VB) [21, 22, 23]. However, in case of a core/shell structure, the potential drop across the tunneling junctions is strongly modified as the consequence of an additional shell, making the interpretation of the tunneling spectra delicate [24].

In this study, we show that the potential drop across both tunneling junctions is rather symmetric when we study PbSe/CdSe core/shell NCs with an intended shell thickness of 0.4 Å. As a result, the peaks observed in the tunneling spectra at both negative and positive voltages are related to one type of charge carriers only, that corresponds to holes for most of the NCs. Such configuration is appropriate to investigate the shell–filling regime and measure the charging energy in such quantum dots. As the nature of the tunneling charge carriers varies from NCs to NCs, the shell structure has also been investigated by photoemission spectroscopy. It reveals the existence of a partial shell that accounts for the fluctuations of the potential drop measured across the tunneling junctions, depending on the orientations that the NCs have adopted on the substrate.

4.2. Experiment details

For our experiment, PbSe core particles were synthesized according to literature methods [25]. The formation of the shell was achieved via the cationic exchange of Pb by Cd, where a mixture of Cd oleate was added to the PbSe NCs suspension in toluene heated at 100 °C [26]. The reaction leaves unchanged the mean diameter of NCs at 7.9 nm and was halted when the replacement of the outermost Pb atoms by Cd cations yielded as a shell thickness of 0.4 nm. To create stable samples for tunneling spectroscopy measurement, Langmuir–Blodgett (LB) monolayers were formed by dropping the resulting NCs, suspended in $CHCl_3$ on a Langmuir through, followed by a single–stroke compression of the Langmuir film. The transfer of PbSe/CdSe QDs to a flame–annealed Au(111) substrate was typically achieved with a surface pressure of 25 mN/m, as shown in Figure 4.1.

The sample was then quickly loaded in an ultra high vacuum (UHV) system containing an Omicron Low Temperature Scanning Tunneling Microscope (LT–STM). In order to remove residual organic contaminations, the sample was annealed at 120 ^{o}C for several hours in high vacuum. The spectroscopic experiments were performed on individual nanocrystals with different diameters by measuring the dynamic differential conductance using a lock–amplifier (normally, we used $V_{mod\ p\text{–}p}$ = 11–15 mV and f_{mod} = 0.5–1 kHz) at Helium temperature (4.8 K).

© 2012 Tous droits réservés.

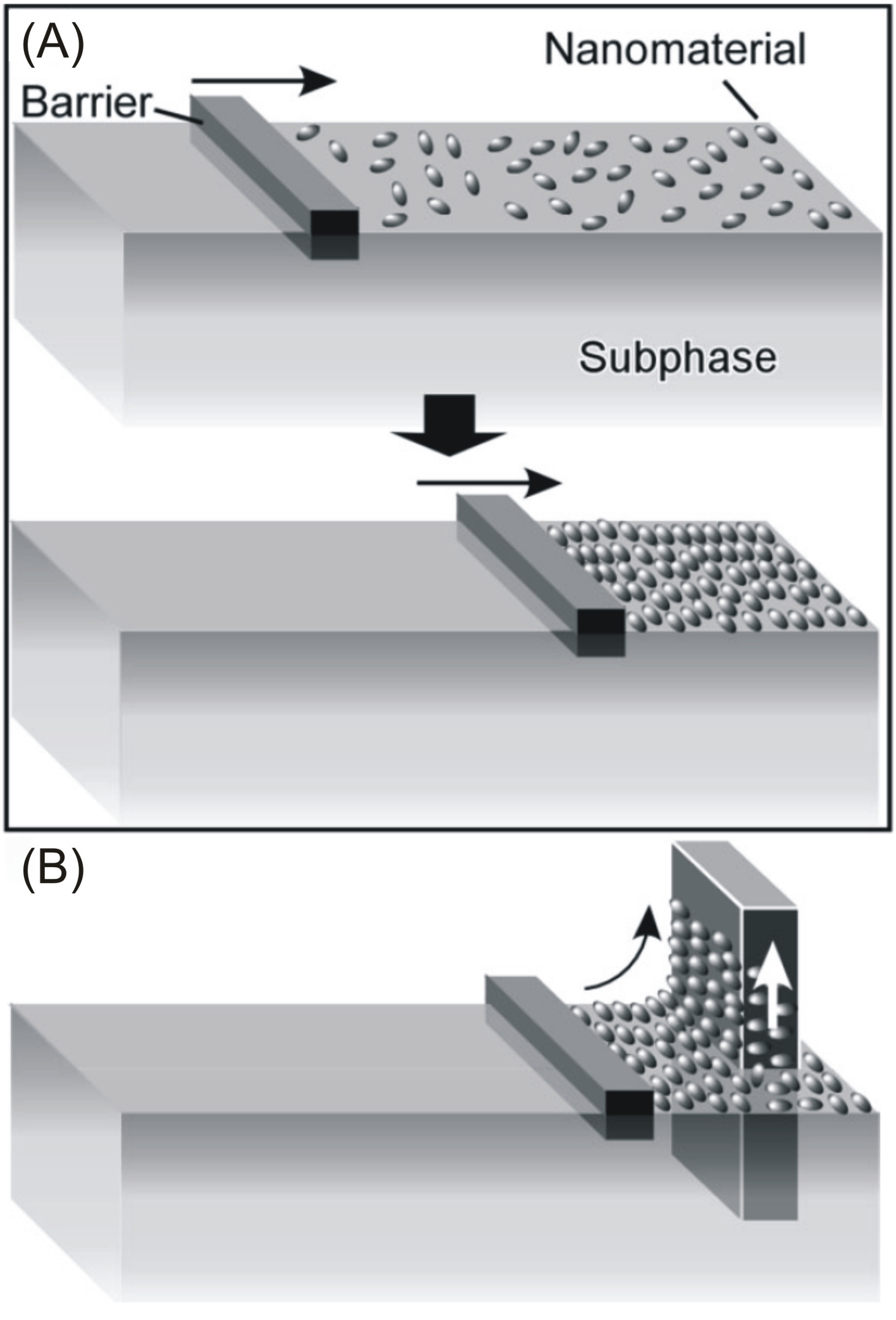

Figure 4.1: Langmuir–Blodgett technique for depositing NCs: (A) schematic illustration of compression of nanomaterials by barrier motion at the air/water interface and (B) transfer process of monolayer NCs onto the substrate [27].

© 2012 Tous droits réservés.

For studying the core levels by X–ray Photoelectrons Spectroscopy (XPS), a monochromatic Al Kα X–ray source and an analyzer pass energy of 11.75 eV were used. Under these conditions, the overall resolution as measured from the FWHM (Full Width at Half Maximum) of the Ag $3d_{5/2}$ line is 0.55 eV. The binding energy scale is calibrated using the Au $4f_{7/2}$ line at 84.0 eV. The acceptance angle of the analyzer has been set to 14° and the angle between the incident X-rays and the analyzer is 90°. The detection angle of the photoelectrons is 45°. For the core level decomposition, we use Voigt functions and a least-square minimization procedure after standard Shrley background substraction. The different components are modeled with the same parameters, i.e. the Gaussian and Lorentzian broadenings are kept fixed for each component of a given core level. The spin orbit splitting for the Cd 4*d*, Se 3*d* and Pb 5*d* peaks was set at 0.67 ± 0.05 eV, 0.65 ± 0.05 eV and 2.61 ± 0.05 eV respectively.

4.3. STM images of a monolayer PbSe/CdSe core/shell NCs

STM was successfully used to image a monolayer of PbSe/CdSe NCs. For example, a constant current height image of a LB monolayer of PbSe/CdSe core/shell NCs transferred onto an Au(111) surface is shown in Figure 4.2(a). The layer of nanocrystals has a two dimensional close–packed arrangement with local hexagonal packing, as presented in Figure 4.2(b). All the images are acquired at the sample voltage V_s of +2 V and a tunnelling current I_{set} of 10 pA. From the large scale image in Figure 4.2 and the corresponding Fourier transform image (see Figure 4.2(c)), an average dot–to–dot distance (or center–to–center spacing) of 8.1±0.1 nm is found. This separation is slightly larger than the mean diameter 7.9 nm of the NCs. But it is still smaller than the separation usually observed between NCs that are deposited into and array the drop casting method [28], suggesting that the oleic acid ligands are more strongly compressed in LB monolayer.

As the mean interdot separation is consistent with the mean NC diameter, it is possible to determine the size of the NCs directly from the high resolution STM images. For example in Figure 4.2(b), the smallest NC (indicated by the cross) has a diameter of around 7 nm, whereas, the biggest NC (ticked by the circle) has a diameter of ~10 nm.

By locating the tip above a PbSe/CdSe dot, sweeping the tip–substrate voltage with the feedback loop open allows to measure the differential conductance spectrum across the double barrier tunneling junction of tip–NC–substrate system. Typical tunnelling spectra measured on a PbSe/CdSe NC with a diameter of 10.5 nm (i) and on a PbSe NC with a diameter of 8.7 nm (ii) are shown in Figure 4.3. The curve (i) reveals a zero–conductivity gap surrounded by sequences of peaks at positive and negative sample voltages. These conductance peaks are caused by the tunnelling of charge carriers through the quantized levels of the nanocrystal. Interestingly, the zero–conductivity gap and the energy level separation appear to be much larger than the ones measured for a slightly smaller PbSe NC with similar feedback loop settings.

© 2012 Tous droits réservés.

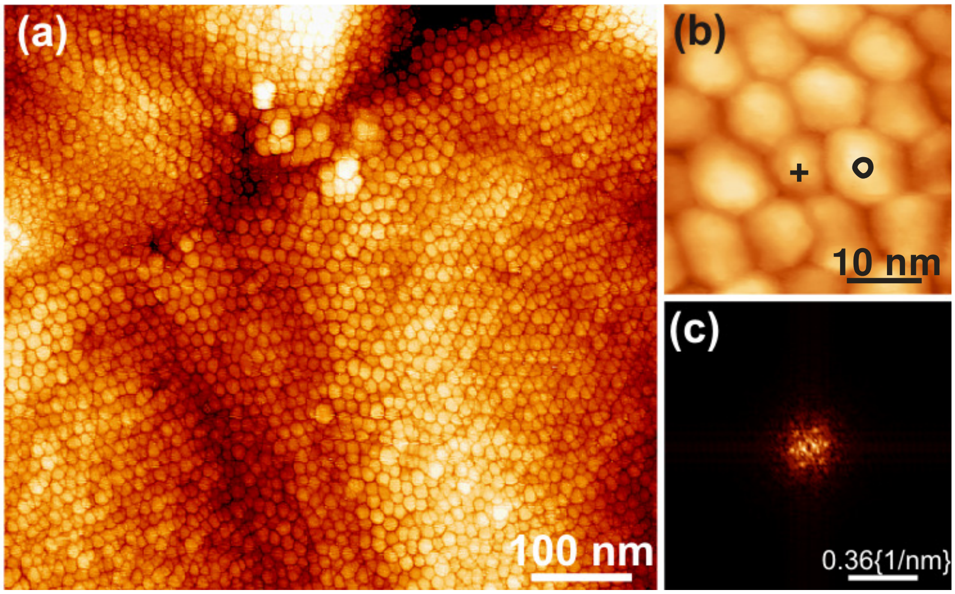

Figure 4.2 : (a) Large scale STM image of PbSe/CdSe NCs transferred onto a Au(111) surface by the Langmuir-Blodgett technique. (b) High resolution STM image of the close-packed NC monolayer. The images were acquired at a sample voltage V_S *of + 2.0 V, a tunnelling current* I_{set} *of 10 pA. (c) Fourrier transform image from the one in (b).*

To be able to give an explanation for the observation mentioned above, we have to take into account the presence of the shell. In fact, as the shell thickness is 0.4 nm, the core size of PbSe/CdSe core/shell dot is bigger by a difference of 0.6 nm than the diameter of the PbSe NC. Thus, a reduction of the confinement should lead to a smaller apparent ban gap of the PbSe/CdSe NCs with respect to the PbSe NCs, but instead, an increase is observed. This behaviour is thus attributed to the change of potential distribution between both tunnelling junctions. In such a system, the potential distribution is usually characterized by the lever arm η, which corresponds to the ratio between the potential drop across the tip–NC junction and the voltage applied to the gold surface with respect to the tip held at virtual ground. In case of a PbSe core only, for low set–point currents the DBTJ is typically asymmetric, with the tip–NC separation being much larger than the NC–substrate distance. As a result, the lever arm is close to 1.

In contrast, the NC–substrate distance increases as the consequence of an additional shell around the core. So, the transmission probability across DBTJ gets smaller and to be able to work with similar tunnelling current setpoints requires a decrease of the tip–NC distance. If the shell thickness is assumed to be homogeneous, then the width of both tunnelling junctions become comparable and a decrease of the lever arm would be expected. It should even reach 0.5. Such a lever arm leads to an increase of the zero–conductivity gap since the apparent band gap corresponds to the quasiparticle gap divided by the level arm [29].

© 2012 Tous droits réservés.

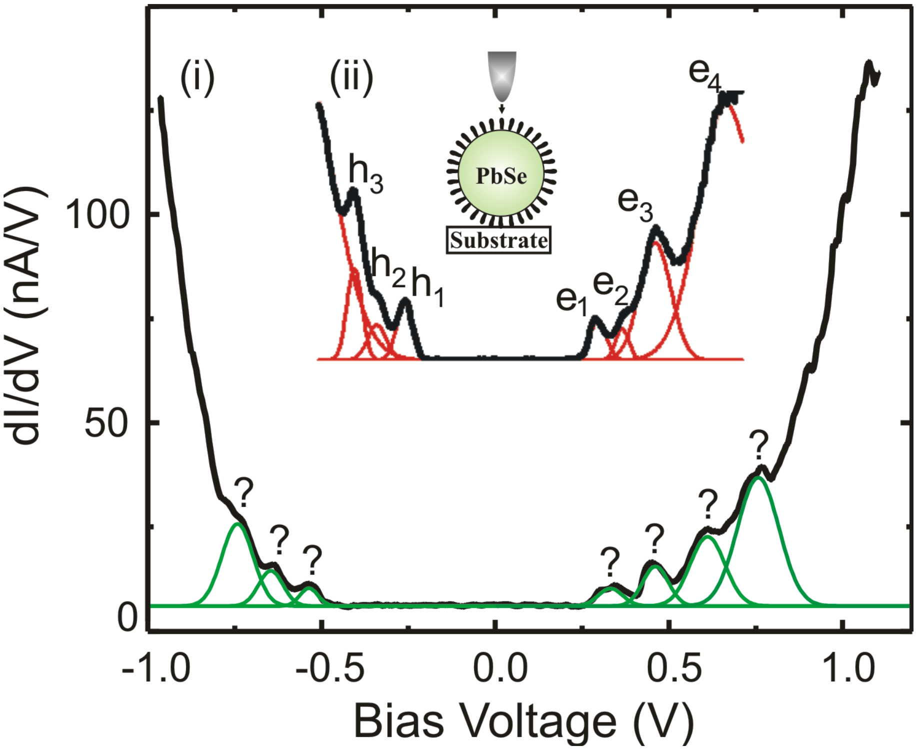

Figure 4.3: Tunneling spectra measured on a PbSe/CdSe NC with a diameter of 10.5 nm and a PbSe NC with a diameter of 8.7 nm. The spectra are fitted with Gaussian functions and the resonances are labelled h_1 to h_3 for the valence levels and e_1 to e_4 for the conduction levels of the PbSe NC. Feedback conditions : (i) $V_S = +1.2$ V, $I_{set} = 0.5$ nA; (ii) $V_S = 0.7$ V, $I_{set} = 0.4$ nA. The inset presents the experimental schematics of tunnelling spectra measurements of performed with PbSe NC, curves (i). The question marks in curve (ii) are related to the quantized states that will be discriminated in this chapter.

4.4. Interpretation of tunneling spectra

4.4.1. Tunneling of electrons on positive side and holes on negative side of the zero–conductivity gap

While a more symmetric potential distribution across the DBTJ significantly affects the width of the zero–conductivity region, it is also makes the assignment of the resonance peaks more difficult [24, 29, 30]. Indeed, depending on the position of the Fermi level in the band gap, the same type of carriers can contribute to the tunnelling current on both sides of the zero–conductivity gap before the occurrence of a combined electron–hole transport. In order to determine if the levels at the edge of the zero–conductivity region are related to the electron or hole ground state, a set of differential conductance spectra acquired with increasing set–point currents can be measured. If the separation between the peaks surrounding the zero–conductivity region increases with higher set–point currents, then the peaks arise from the

© 2012 Tous droits réservés.

contribution of the hole and electron ground states at negative and positive sample voltages respectively [29]. In what follows, we will label such peaks $V_{h_1}^-$ and $V_{e_1}^+$.

Such a set of spectra are seen in Figure 4.4(a) for a PbSe/CdSe core/shell NC with a diameter of 8.5 nm. $V_{h_1}^-$ and $V_{e_1}^+$ are labelled to stand for tunnelling of holes and electrons through the hole and electron states on both sides of the gap respectively. A shift of the peaks $V_{h_1}^-$ and $V_{e_1}^+$ (see Figure 4.5(b)) induces a slight widening of the apparent band gap with increasing setpoint currents. Knowing the diameter and assuming that the electronic properties of the core are not strongly affected by the shell, a band gap E_G of 0.55 eV and a polarization energy Σ of 23 meV were respectively calculated [21, 31]. From the measurement of the zero–conductance region, the level arm was deduced to decrease from 0.72 to 0.71 when the setpoint current changes from 0.5 nA to 3.0 nA. In such a case, the potential predominantly drops across the tip–NC junction, suggesting that this junction is larger than the NC–substrate junction.

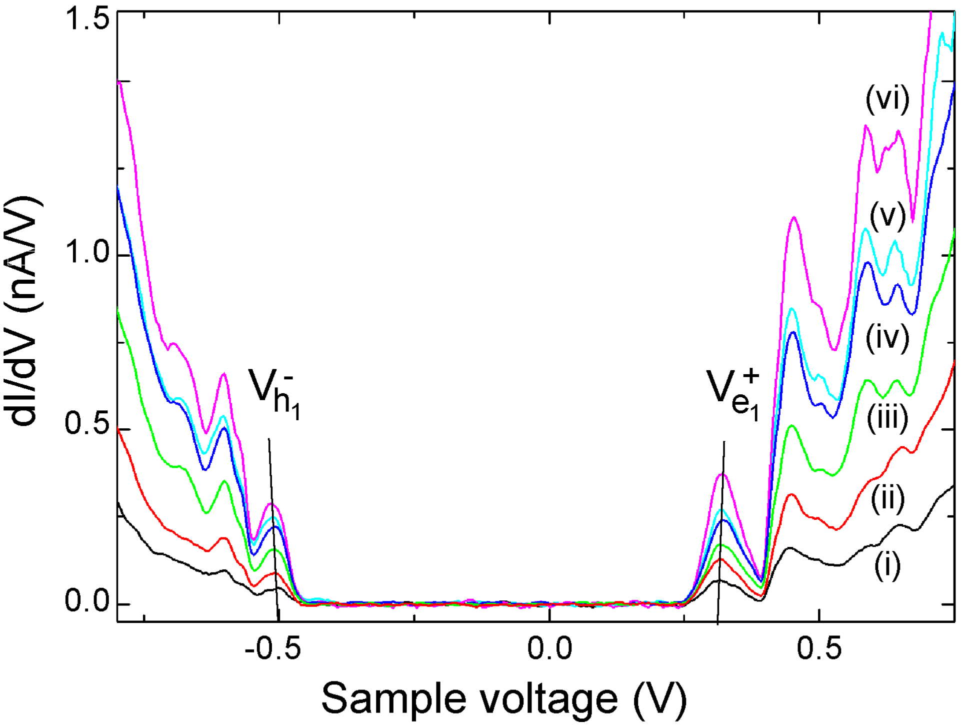

Figure 4.4: Set of differential conductance spectra measured on a PbSe/CdSe NC with a diameter of 8.5 nm. The feedback parameters were $V_S = +1.2$ V and $I_{set} = 0.5$ nA (i), 1.0 nA (ii), 1.5 nA (iii), 2.0 nA (iv), 2.5 nA (v), 3.0 nA (vi). The peaks labelled $V_{h_1}^-$, $V_{e_1}^+$ correspond to the tunneling of holes and electrons through the hole and electron ground states respectively. The oblique segments are used as eye guide to highlight the shift of the peak positions with increasing I_{set}.

© 2012 Tous droits réservés.

4.4.2. Holes tunneling on both sides of the zero–conductivity gap

However, most of the spectra recorded on other PbSe/CdSe NCs did not show the same behaviour. Instead, the majority of the NCs exhibited a set of differential conductance spectra similar as the one shown in Figure 4.5(a). Whatever the set–point current is, the peak structure of the spectra is similar, but the shift of the peaks on both sides of the zero–conductivity gap differ readily from the shift of the peaks in Figure 4.4(a). Indeed, the increase of the set–point current causes a shift of the lowest peak measured at positive bias towards smaller value of sample voltages (see Figure 4.5(b)). This shift is opposite to what is expected if electrons were tunnelling through the conduction band ground state for smaller lever arms [29]. Thus, it is identified as the contribution of the hole ground state h_1 to the tunnelling current. The peak is labelled $V_{h_1}^{+}$ in Figure 4.5(a), since this state is probed at positive bias.

In order to confirm that the onsets of the differential conductance are caused by tunnelling through the hole ground state at negative and positive voltages, the evolution of the zero–conductivity region can be analyzed as a function of the lever arm, based on the electronic properties of the NC, as shown in Figure 4.5(c). Taking into account the position of $V_{h_1}^{+}$ and the separation of $V_{h_1}^{+}$ and $V_{h_1}^{-}$ allows us to deduce the lever arm in case of holes tunnelling on both sides of the zero–conductivity region, as:

$$\eta = \frac{V_{h_1}^{+}}{V_{h_1}^{+} - V_{h_1}^{-}} \tag{4.1}$$

Experimentally, we find that the lever arm is proportional to the set–point current. At low set–point current, a lever arm of 0.53 is measured. Then, the level arm monotonously decreases as the set–current increases. Knowing the diameter of the NC from the topographic STM image and assuming that a very thin layer of CdSe around the core does not affect significantly the electronic structure of the core, we calculate a quasiparticle gap of 596 meV for a PbSe core with a diameter of 7.7 nm, the band gap E_G and the polarization energy Σ being 550 meV and 23 meV respectively [31]. As a result, the position of the hole ground state h_1 with respect to the Fermi level E_F is given by:

$$h_1 - E_F = \eta e V_{h_1}^{-} + \Sigma = -\left((1-\eta) V_{h_1}^{+} - \Sigma \right) \tag{4.2}$$

Considering E_F as the reference energy, we obtain h_1 = −169 meV, with a variation of ±1 meV for the range of set–point currents used in the experiments, as found in Figure 4.5(a) for example.

© 2012 Tous droits réservés.

The theoretical knowledge of the band gap yields e_1 = 381 meV. Although the peaks $V_{e_1}^{+}$, $V_{e_1}^{-}$, that correspond to the tunnelling of electrons from the conduction band ground state at positive and negative voltages respectively, are not provided by the spectroscopic experiments, they can be deduced from the knowledge of e_1:

$$eV_{e_1}^{+} = \frac{(e_1 - E_F) + \Sigma}{\eta} \tag{4.3}$$

and:

$$eV_{e_1}^{-} = -\frac{(e_1 - E_F) + \Sigma}{1-\eta}$$

(4.4)

Derived from the equations (4.2), (4.3) and (4.4), the position of the peaks $V_{h_1}^{-}$, $V_{e_1}^{-}$, $V_{e_1}^{+}$, and $V_{h_1}^{+}$ can be plotted as the functions of the lever arm, as shown in Figure 4.5(c). The shaded area of Figure 4.5(c) corresponds to the range of lever arms deduced from Figure 4.5(a). $V_{e_1}^{+}$ and $V_{e_1}^{-}$ are clearly higher and lower than $V_{h_1}^{+}$ and $V_{h_1}^{-}$ respectively, demonstrating that only holes are allowed to tunnel on both sides of the zero–conductivity region.

We also note that the second peak observed at positive and negative voltages shift in the same way as the set–point current increases. This peak could arise from the contribution of the first hole excited state, labelled as $V_{h_2}^{-}/V_{h_2}^{+}$ depending on the bias. However, a lever arm close to 0.5 means that the probabilities to tunnel into or out of the NC are similar, implying that a hole can already reside in the NC when a new hole tunnels into the NC. In this case, the second peak would be caused by the charging energy required to keep two holes on the ground state and the corresponding peaks are marked as $V_{2h_1}^{-}$ and $V_{2h_1}^{+}$ for both signs of sample voltages. To clarify between the first excited state and the charging of hole ground state, we calculate the position of the first excited state and the charging energy versus the lever arm η [31]. As shown in Figure 4.5(c), the spectral separation between $V_{h_2}^{-}$ and $V_{h_1}^{-}$ for a lever arm around 0.5 is about 270 meV. Conversely, the spectral separation between $V_{2h_1}^{-}$ and $V_{h_1}^{-}$ is smaller, around 100 meV. This value is consistent with the separations found between the first and the second peaks at the negative voltage in figure 4.5(a), that yields a charging energy of 50 meV. Therefore, the second peak at negative voltage in Figure 4.5(a) is attributed to the tunnelling of a second hole into the hole ground state that already bears one hole. At positive voltage, the energy separation between the first and the second peaks is slightly higher by a difference of about 20 meV, because here the separation of energy is divided by $(1-\eta)$ instead of η, and this second peak is

© 2012 Tous droits réservés.

identified as $V^{+}_{2h_1}$: corresponding to a second hole is transferred into the hole ground state at positive bias.

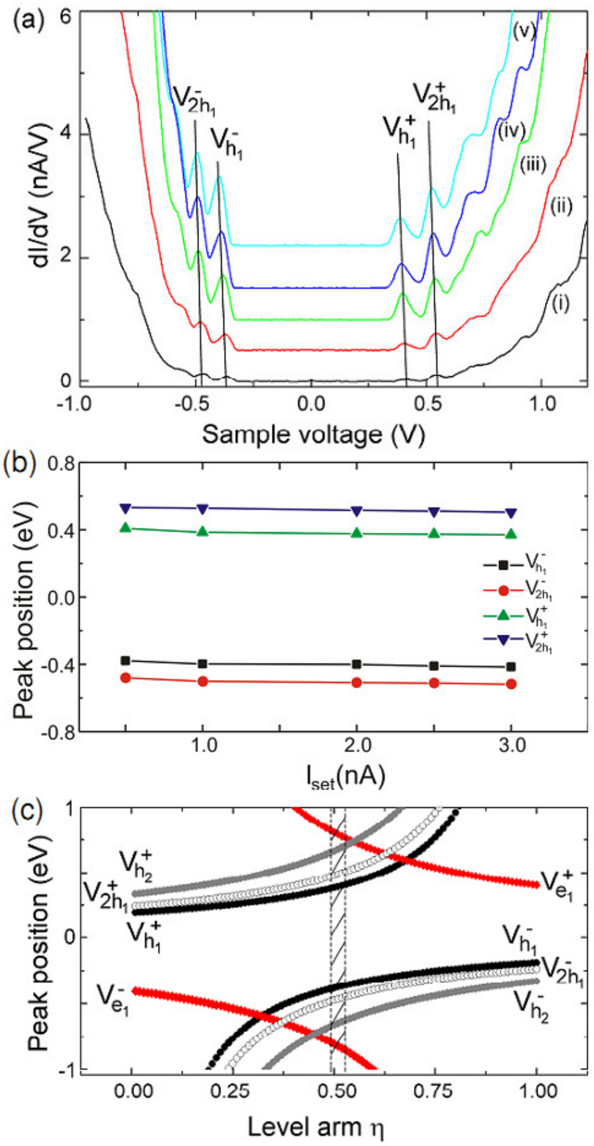

Figure 4.5: (a) Set of differential conductance spectra measured on a PbSe/CdSe NC with a diameter of 8.5 nm. The feedback parameters were $V_S = +1.2$ *V and* $I_{set} = 0.5$ *nA (i), 1.0 nA (ii), 2.0 nA (iii), 2.5 nA (iv), 3.0 nA (v). The peaks labelled* $V^{-}_{h_1}$, $V^{-}_{2h_1}$, $V^{+}_{h_1}$, $V^{+}_{2h_1}$ *correspond to tunneling through the hole ground state with zero and one hole at negative and positive bias. The oblique segments are used as eye guide to highlight the shift of the peak positions with increasing* I_{set}. *(b) Positions of* $V^{-}_{h_1}$, $V^{-}_{2h_1}$, $V^{+}_{h_1}$, *and* $V^{+}_{2h_1}$ *peaks form the set of tunnelling spectra in (a) measured as a function of set–point currents. (c) Variation of the peak position measured in tunneling spectroscopy as a function of the lever arm* η.

© 2012 Tous droits réservés.

The hole first excited and electron ground states measured at negative and positive voltages are respectively labelled $V_{h_2}^{-}$, $V_{h_2}^{+}$, $V_{e_1}^{-}$, $V_{e_1}^{+}$. *The shaded region corresponds to the range of lever arms found in (a).*

Finally, the third peak observed at negative voltage, which mostly appears as a shoulder, is separated by the same amount of energy than $e\left(V_{2h_1}^{-}-V_{h_1}^{-}\right)$. This third peak is reasonably attributed to the tunnelling of a third hole into the hole ground state that contains already two holes. This suggestion is in agreement with the fact that an energy level can accommodate up to 8 holes due to its spin degeneracy.

4.4.3. Electrons tunneling on both sides of the zero–conductivity gap

The opposite regime can also be found in much smaller cases, where only electrons tunnel on both sides of the zero–conductivity region. Figure 4.6(a) gives an example of a set of spectroscopic measurements performed with increasing set–point currents. The onset of the first peaks shifts toward higher sample voltages whatever the polarity is (as seen in Figure 4.6(b)). This behaviour allows us to attribute the peaks $V_{e_1}^{+}$ and $V_{e_1}^{-}$ to the contribution of the electron ground state at positive and negative voltages.

In order to determine the origin of the second peak observed at positive voltage, it is possible to deduce the lever arm from the position of $V_{e_1}^{-}$ and the separation of $V_{e_1}^{+}$ and $V_{e_1}^{-}$, then:

$$\eta=\frac{V_{e_1}^{-}}{V_{e_1}^{-}-V_{e_1}^{+}} \tag{4.5}$$

At low set–point current, we can measure a lever arm of 0.43. Then the lever arm decreases to 0.4 as the set–point current increases. Based on the diameter of the NC, 8.1 nm, that corresponds to a core size of 7.4 nm, the charging energy should be 50 meV. Translating the charging energy into voltage yields a voltage separation between the first and the second peaks of 116 meV, as shown in Figure 4.6(c). Such separation, which is much smaller than the first electron intraband transition of 120 meV divided by the lever arm, is close to the energy separation of 129 meV found at low set–point current.

Therefore, we identify the second peak to the transfer of an electron into the electron ground state that already hosts one electron. Similarly, the energy separation between the second peak and the third peak is 136 meV suggesting that the second peak is related to the charging of the electron ground state which already hosts two electrons. Interestingly, at a lever arm just smaller than 0.4, a hole and an electron are likely to be transferred to the NC quantum levels simultaneously. As there are some uncertainties on the NC size and thus on the peak positions, such situation might

© 2012 Tous droits réservés.

explain why the third peak disappears when the set–point current increases in Figure 4.6(a).

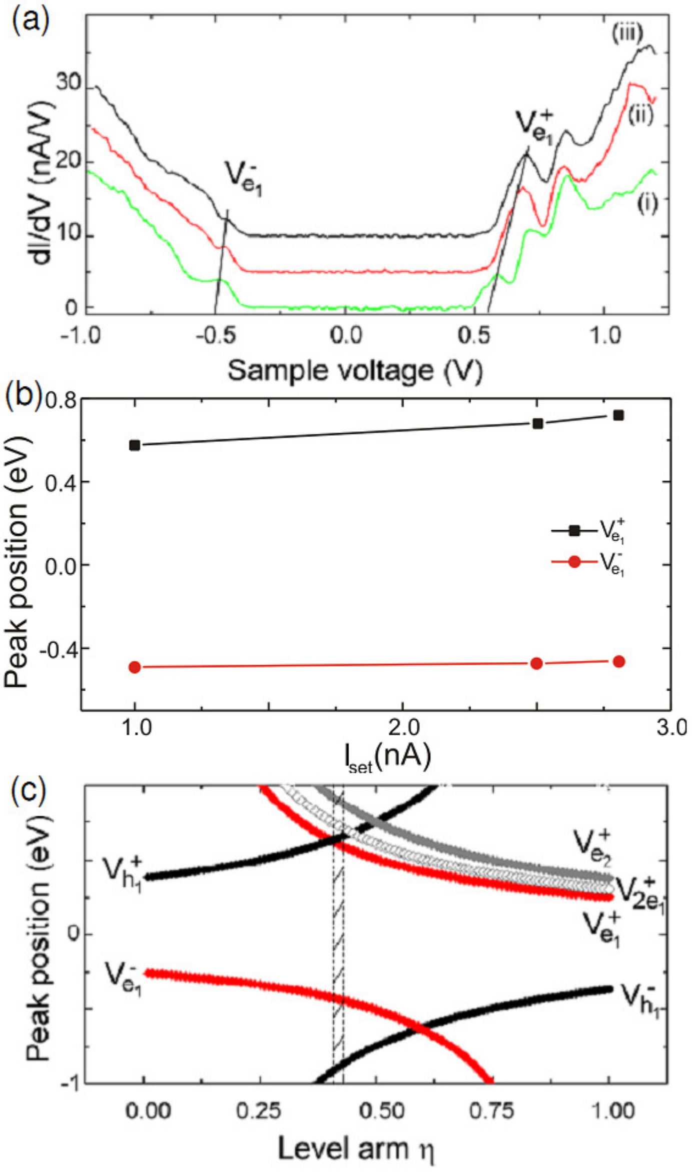

Figure 4.6: Set of differential conductance spectra measured on a PbSe/CdSe NC with a diameter of 8.1 nm. The feedback parameters were V_S = +1.2 V and I_{set} = 1 nA (i), 2.5 nA (ii) and 2.8 nA (iii). The peaks labelled $V_{e_1}^-$, $V_{e_1}^+$ correspond to the tunneling of electron from the electron ground state at negative and positive bias. The oblique segments are used as eye guide to highlight the shift of the peak positions with increasing I_{set}. (b) Positions of $V_{h_1}^-$, $V_{h_1}^+$, $V_{2e_1}^+$, V_{e2}^+ peaks in Figure 4.6(a) measured as a

© 2012 Tous droits réservés.

function of current set–point. (c) Variation of the peak position measured in tunneling spectroscopy as a function of the lever arm η. *The peaks labelled* $V_{h_1}^-$, $V_{h_1}^+$, $V_{2e_1}^+$, V_{e2}^+ *correspond to tunneling through the hole ground state at negative and positive bias, the electron ground state that holds one electron, and the electron first excited at positive bias. The shaded region corresponds to the range of lever arms found in (a).*

4.5. Discussion

In contrast to most of the tunnelling spectroscopic measurements performed on PbSe quantum dots [21, 31], the addition of a very thin shell of CdSe results in the accumulation of charge carriers in the NC, due to the similar transmission probability across both tunnelling junction (tip–NC junction and NC–junction). While the level arm is close to 0.5 for more than 80% of the NCs that were probed, the Fermi level is not positioned at the same energy in the band gap of the NC.

Usually, it is closer to the valence band edge as holes tunnel on both sides of the zero−conducting region (see Figure 4.5(a)). But, for some NCs it lies in the upper part of the band gap, as the dot since some spectra show that electrons tunnel on both sides of the zero−conductivity region (see Figure 4.6(a)). Additionally, the latter example reveals that the level arm can be lower than 0.5, indicating that the potential drop predominantly occurs between the NC and the substrate. Such result suggests that the tip−NC distance becomes smaller than the NC−substrate distance. Therefore, the shell thickness would be inhomogeneous around the PbSe core.

To clarify this point, X−ray photoemission spectroscopic (XRD) measurements have been performed on the same sample. For comparison, two others additional set of NCs were investigated: a sample consisting of PbSe NCs only and a sample with PbSe/CdSe core/shell NCs, where the thickness of the shell was 2 nm. Both samples are not annealed prior to the XPS experiments to avoid any phase transformation of the NCs [32]. When the XPS spectra of all three samples are compared, see Figure 4.7, the successful cation exchange between Pb and Cd, at the surface of the NCs considered in STS study, is demonstrated through:

- The presence of the Cd 4*d* peak, that is almost similar to the Cd 4*d* peak observed for the NCs with a thick CdSe shell.
- The occurrence of a Se 3*d* peak that shows an intermediate lineshape between the lineshape obtained for the PbSe NCs and the PbSe NCs surrounded by a thick CdSe shell.

For this later element, the lineshape rather resembles that of PbSe NCs, although fitting the peak required four components, two of them being related to Se species bound to Cd atoms, consistent with a thin layer of CdSe.

As shown in Figure 4.7 for the Pb 5*d* core level, the comparison of the spectra reveals a significant variation of the linewidth between the PbSe/CdSe core/shell NCs

© 2012 Tous droits réservés.

and the PbSe NCs. In the case of the PbSe/CdSe NCs with a thick shell, the Pb $5d_{5/2}$ (lower binding energy) and Pb $5d_{3/2}$ (higher binding energy) peaks are decomposed with a single component that is mainly related to the Pb atoms bound to Se atoms in the core of the NCs. For the Pb $5d_{5/2}$ peak, this component is centred at a binding energy of 19.27 eV and has a full width at half maximum (FWHM) of 0.84 eV.

Conversely, the Pb $5d_{5/2}$ peak of PbSe NCs requires the use of two components. From the comparison of the peak position with the one obtained for the PbSe/CdSe NCs with a thick shell, we attribute the component at the lowest binding energy, centred at 19.13 eV (FWHM 0.80 eV), to the bulk contribution. The second peak with the highest binding energy, centred at 19.74 eV (FWHM 1.05 eV), is thus related to the surface. Its position as well as its width would correspond to surface Pb atoms bound to oxygen, in agreement with results reported for the oxidation of PbSe.[33] Such PbO species exist due to the passivation of the NC surface with ligands through the existence of PbO chemical bond, but also because the surface of the NCs oxidizes during the transfer of the NCs in air for surface site which are not passivated with ligands.

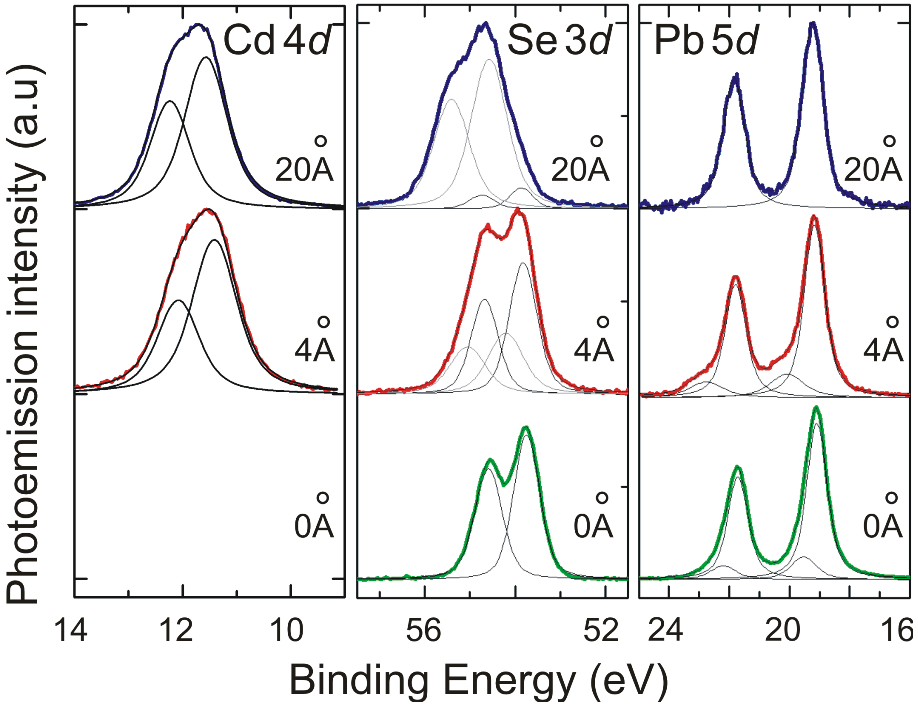

Figure 4.7: Background-substracted Cd 4d, Se 3d and Pb 5d core level spectra and fits of PbSe/CdSe NCs with different CdSe thickness as indicated in the graph.

Looking at the Pb peaks of the NCs considered in the STS experiments, the linewidth is smaller than the linewidth of the PbSe NCs. But the Pb $5d_{5/2}$ peak can not

© 2012 Tous droits réservés.

be decomposed with a single component, that is centred at 19.16 eV. Instead, a broad shoulder exists at a higher binding energy (centred at 20.10 eV). As the exchange of Pb by Cd was very limited in time to obtain an equivalent shell thickness smaller than one monolayer for these NCs (the lattice parameter of zincblende CdSe being 6.05 Å), the observation of this shoulder means that a part of the NC surface exposed uncovered PbSe facets, where the Pb atoms are bound to O species. Such results suggests that most of the NCs have a partial CdSe shell, leaving one or several PbSe facets unprotected, in agreement with TEM images of similar NCs where the shell was even thicker. Such fluctuation in the shell thickness from one NC to another one may explain why three types of tunneling spectra have been found. It also accounts for the variations of the Fermi level position, as the pinning of this level certainly changes with the structural and chemical composition of the NC surface. Finally, depending on the location of the unprotected PbSe facets, either exposed to the STM tip or below the NCs against the substrate, the lever arm can greatly vary. In some particular case, it can becomes smaller than 0.5 in contrast to the range of level arms that are usually measured on semiconductor NCs using STS [20, 31].

4.6. Conclusion

In conclusion, we have investigated the electronic structure of PbSe/CdSe core-shell NCs by means of scanning tunneling spectroscopy. The zero conductivity region around the Fermi level was found to be wider than the one usually measured for PbSe NCs with sizes identical to the core diameter. From the analysis of the peak position with respect to the change of the potential drop across the tunneling junctions, we have demonstrated that only one type of charge carriers contribute to the tunneling current on both sides of the zero conductivity gap for the majority of the NCs. Thus, the width of the zero conductivity region is not related to the quasi-particle band gap of the NCs. Instead, the determination of the peak position on both sides of the zero conductivity region yields the lever arm. For the majority of the NCs, a lever arm close to 0.5 was obtained, indicating that the probability for a carrier to tunnel into or out of the NCs is almost similar. Such configuration is known to favor the charging of the NCs. A charging energy of the order of 50 meV was measured for NCs with a mean diameter around 8 nm, consistent with the charging energy expected for PbSe NCs with similar sizes. Therefore, while the addition of a very thin CdSe shell does not seem to significantly modify the electronic structure of the PbSe core, it offers the possibility to study transport regimes that would not be accessible without the shell.

© 2012 Tous droits réservés.

© 2012 Tous droits réservés.

References

---

[1] V. L. Colvin, M. C. Schlamp, and A. P. Alivisatos, "*Light-emitting diodes made from cadmium selenide nanocrystals and a semiconductor polymer*", Nature **370**, 354–357 (1994).

[2] D. L. Klein, R. Roth, A. K. L. Lim, A. P. Alivisatos, and P. L. McEuen, "*A single electron transistor made from a cadmium selenide nanocrystal*", Nature **389**, 699–701 (1997).

[3] M. Nirmal, B. O. Dabbousi, M. G. Bawendi, J. J. Macklin, J. K. Trautman, T. D. Harris, and L. E. Brus, "*Fluorescence intermittency in single cadmium selenide nanocrystals*", Nature **383**, 802–804 (1996).

[4] M. Kuno, D. P. Fromm, H. F. Hamann, A. Gallagher, and D. J. Nesbitt, "*Nonexponential 'blinking' kinetics of single CdSe quantum dots: A universal power law behavior*", J. Chem. Phys. **112**, 3117–3120 (2000).

[5] Al. L. Efros, and M. Rosen, "*Random telegraph signal in the photoluminescence intensity of a single quantum dot*", Phys. Rev. Lett. **78**, 1110–1113 (1997).

[6] P. Frantsuzov, M. Kuno, B. Janko, and R. A. Marcus, "*Universal emission intermittency in quantum dots, nanorods and nanowires*", Nature Phys. **4**, 519–522 (2008).

[7] X. Wang, X. Ren, K. Kahen, M. A. Hahn, M. Rajeswaran, S. Maccagnano-Zacher, J. Silcox, G. E. Cragg, A. L. Efros, and T. D. Krauss, "*Non-blinking semiconductor nanocrystals*", Nature **459**, 686–689 (2009).

[8] X. Brokmann, J.-P. Hermier, G. Messin, P. Desbiolles, J.-P. Bouchaud, and M. Dahan, "*Statistical Aging and Nonergodicity in the Fluorescence of Single Nanocrystals*", Phys. Rev. Lett. **90**, 120601 (2003).

[9] L. Jdira, K. Overgaag, R. Stiufiuc, B Grandidier, C. Delerue, S. Speller, and D. Vanmaekelberg, "*The line width of the resonance in scanning tunneling spectroscopy*", Phys. Rev. B. **77**, 205308 (2008).

[10] B. Mahler, P. Spinicelli, S. Buil, X. Quelin, J. Hermier, and B. Dubertret, "*Towards non-blinking colloidal quantum dots*", Nature Materials. **7**, 659–664 (2008).

[11] F. Garcia–Santamaria, Y. Chen, J. Vela, R. D. Schaller, J. A. Hollingsworth, and V. I. Klimov, "*Suppressed Auger Recombination in "Giant" Nanocrystals Boosts Optical Gain Performance*", Nano. Lett. **9** (10), 3482–3488 (2009).

[12] J. Müller, J. M. Lupton, P. G. Lagoudakis, F. Schindler, R. Koeppe, A. L. Rogach, J. Feldmann, D. V. Talapin, and H. Weller, "*Wave Function Engineering in Elongated Semiconductor Nanocrystals with Heterogeneous Carrier Confinement*", Nano. Lett. **5** (10), 2044–2049 (2005).

© 2012 Tous droits réservés.

---

[13] M. G. Lupo, F. D. Sala, L. Carbone, M. Zavelani-Rossi, A. Fiore, L. Lüer, D. Polli, R. Cingolani, L. Manna, and G. Lanzani "*Ultrafast Electron−Hole Dynamics in Core/Shell CdSe/CdS Dot/Rod Nanocrystals*", Nano. Lett. **8** (12), 4582–4587 (2008).

[14] P. Reiss, M. Protière, and L. Li, "*Core/Shell Semiconductor Nanocrystals*", Small **5**, 154−168 (2009).

[15] G. Raino, T. Stöferle, I. Moreels, R. Gomes, J. S. Kamal, Z. Hens, and R. F. Mahrt, "*Probing the Wave Function Delocalization in CdSe/CdS Dot−in−Rod Nanocrystals by Time− and Temperature−Resolved Spectroscopy*", ACS Nano **5** (5), 4031−4036 (2011).

[16] J. W. Stouwdam, J. Shan, F. C. J. M. Van Veggel, A. G. Pattantyus−Abraham, J. F. Young, and M. Raydsepp, "Photo-stability of Colloidal PbSe and PbSe/PbS Core/shell Nanocrystals in Solution and in the Solid State", J. Phys. Chem. C. **111**, 1086−1092 (2007).

[17] J. M. Pietryga, D. J. Werder, D. J. Williams, J. L. Casson, R. D. Schaller, V. I. Klimov, and J. A. Hollongsworth, "*Utilizing the Lability of Lead Selenide to Produce Heterostructured Nanocrystals with Bright, Stable Infrared Emission*", J. Am. Chem. Soc. **130**, 4879 (2008).

[18] B. De Geyter, Y. Justo, I. Morrels, K. Lambert, P. F. Smet, D. Van Thourhout, A. J. Houtepen, D. Grodzinska, C. De Mello Donega, A. Meijerink, D. Vanmaekelbergh, and Z. Hens, "*The Different Nature of Band Edge Absorption and Emission in Colloidal PbSe/CdSe Core/Shell Quantum Dots*", ACS Nano **5**, 58−66 (2011).

[19] U. Banin, Y.W. Cao, D. Katz, and O. Millo, "*Identification of atomic−like electronic states in indium arsenide nanocrystal quantum dots*", Nature **400**, 542−544 (1999).

[20] L. Djira, P. Liljeroth, E. Stoffels, D. Vanmaekelbergh, and S. Speller, "*Size-dependent single-particle energy levels and interparticle Coulomb interactions in CdSe quantum dots measured by scanning tunneling spectroscopy*", Phys. Rev. B **73**, 115305 (2006).

[21] E. P. A. M. Bakkers, and D. Vanmaekelbergh, "*Resonant electron tunneling through semiconducting nanocrystals in a symmetrical and an asymmetrical junction*", Phys. Rev. B **62**, 7743−7746 (2000).

[22] P. Liljeroth, P. A. Zeijlmans van Emmichoven, S. G. Hickey, H. Weller, B. Grandidier, G. Allan, and D. Vanmaekelbergh, "*Density of states measured by scanning-tunneling spectroscopy sheds new light on the optical transitions in PbSe nanocrystals*", Phys. Phys. Lett. **95**, 086801 (2005).

[23] G. A. Grinbom, M. Saraf, C. Saguy, A. C. Bartnik, F. Wise, and E. Lifshitz, "*Density of states in a single PbSe/PbS core-shell quantum dot measured by scanning tunneling spectroscopy*", Phys. Rev. B **81**, 245301 (2010).

[24] I. Swart, Z. Sun, D. Vanmaekelbergh, and P. Liljeroth, "*Hole−Induced Electron Transport through Core−Shell Quantum Dots: A Direct Measurement of the Electron−Hole Interaction*", Nano. Lett. **10** (5), 1931−1935 (2010).

[25] I. Moreels, K. Lambert, D. De Muynck, F. Vanhaecke, D. Poelman, J. C. Martins, G. Allan, and Z. Hens, "*Composition and Size-Dependent Extinction Coefficient of Colloidal PbSe Quantum Dots*", Chem. Mater. **19** (25), 6101−6106 (2007).

© 2012 Tous droits réservés.

---

[26] K. Lambert, B. De Geyter, I. Moreels, and Z. Hens, "*PbTe|CdTe Core|Shell Particles by Cation Exchange, a HR-TEM study*", Chem. Mater. **21** (5), 778–780, (2009).

[27] S. Acharya, J. P. Hill, and K. Ariga, "*Soft Langmuir–Blodgett Technique for Hard Materials*", Adv. Mat. **21**, 2959–2981 (2009).

[28] P. Liljeroth, K. Overgaag, A. Urbieta, B. Grandidier, S. G. Hickey, and D. Vanmaekelbergh, "*Variable Orbital Coupling in a Two–Dimensional Quantum–Dot Solid Probed on a Local Scale*", Phys. Phys. Lett. **97**, 096803 (2006).

[29] Y. M. Niquet, C. Elerue, G. Allan, and M. Lannoo, "*Interpretation and theory of tunneling experiments on single nanostructure*", Phys. Rev. B **65**, 165334 (2002).

[30] B. Li, C. Zeng, J. Zhao, J. Yang, J. G. Hou and Q. Zhu, "*Single-electron tunneling spectroscopy of single C_{60} in double-barrier tunnel junction*", J. Chem. Phys. **124**, 064709 (2006).

[31] K. Overgaag, D. Vanmaekelbergh, P. Liljeroth, G. Mahieu, B. Grandidier, C. Delerue, and G. Allan, "*Electron-phonon coupling and intervalley splitting determine the linewidth of single-electron transport through PbSe*", J. Chem. Phys. **131**, 224510 (2009).

[32] D. Grodzińska, F. Pietra, M. A. van Huis, D. Vanmaekelbergh and C. de Mello Donegá, "*Thermally induced atomic reconstruction of PbSe/CdSe core/shell quantum dots into PbSe/CdSe bi-hemisphere hetero-nanocrystals*", J. Mat. Chem. **131**, xxx (2011).

[33] A. L. Hagström and A. Fahlman, "*The Electronic Structure of PbSe and Its Interaction with O_2 Adsorbate Layers*", Physica Scripta. **16**, 432–435 (1977).

© 2012 Tous droits réservés.

© 2012 Tous droits réservés.

Chapter 5

Tunneling spectroscopy of CdSe/CdS Dot–in–Rod nanocrystal

5.1. Introduction

Precise manipulation of the charge carrier localization in nanocrystals (NCs) is critical for implementing those structures in devices, such as: LEDs, lasers, and photovoltaic cells [1, 2, 3]. The ability of tailoring the overall composition of NCs makes core/shell heterostructures promising for such a kind of applications. In principle, the band offset between the material components are the main parameter that determine their optical and electronic properties [4]. By changing the shape and composition, it is possible to control the electronic structures of semiconductor nanorods (NRs). For this reason, heterostructured nanocrystals have attracted great attention in fundamental research and also provided news ways for light harvesting, carrier collection, and surface catalysis [5, 6, 7]. Generally, in core/shell nanocrystal structures, the wave functions of electrons and holes can be confined together to the core or extend out to the shell. Hence, it is possible to engineer the band offsets by selecting appropriate semiconductor components. Depending on the overlapping of hole and electron wave functions, the core/shell nanocrystals can be classified as Type–I or Type–II heterostructures showing different behaviors. For example, Type–I core/shell structures exhibit bright and stable fluorescence which is useful for biological tagging and light emitting diode applications [1, 8]. Conversely, multiexciton properties, which is important in optical gain applications, are found in Type–II band alignments due to the separation of the photoexcited charge carriers [9, 10]. Therefore, the understanding of band–offsets in core/shell nanostructures is necessary for designing useful heterostructures.

Among the wide range of existing semiconductor NCs, CdSe and CdS quantum dots and rods are materials of choice for optical and electronic applications due to their easy synthesis, high optical quality, and stable surface passivation. Furthermore, both band gaps of CdSe and CdS are in the visible range and also can be tuned by changing the nanocrystal size. Those properties open up the opportunities for optical applications, including solar cell and photoelectrochemical cells. Band offsets in these type of semiconductor heterostructures have been investigated by theoretical calculations on band offset, optical bowings, intraband spectroscopy previously [11, 12,

© 2012 Tous droits réservés.

[13, 14, 15, 16]. The valence–band offset (Δ_V) for the CdSe/CdS interface suggests a confinement of holes in the CdSe materials. In contrast, the conduction–band offset (Δ_C) of CdSe/CdS NCs varies considerably from –0.25 eV [15] (corresponding to Type–II band alignment) up to +0.27 eV [13, 14] (Type–I band alignment), see Figure 5.1.

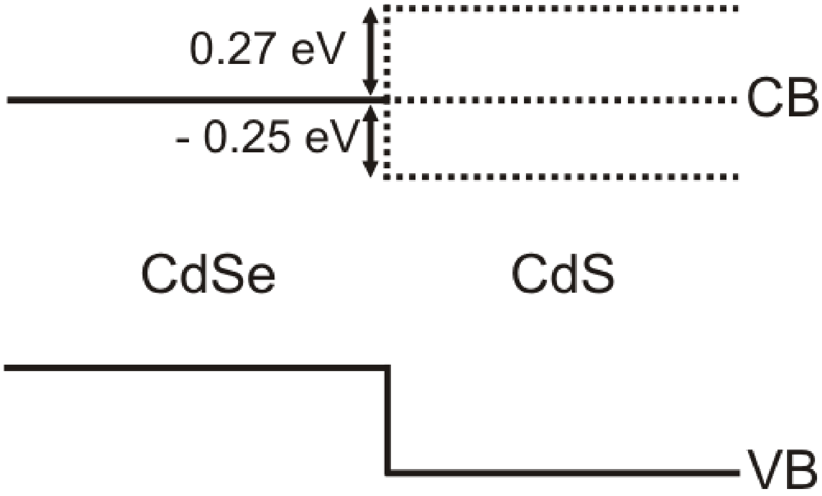

Figure 5.1: Illustration of the band alignment for CdSe/CdS hetero–NCs.

In case of Type–I core/shell structure, the smaller band gap of CdSe (E_g(CdSe) = 1.84 eV at 4 K [17]) lies completely inside the larger band gap of CdS (E_g(CdS) = 2.58 eV at 4K [17]). However, in many previous reports, the heterostructure had a symmetrical form, such as: spherical core/shell quantum dot or cylindrical core/shell nanowire,… Recently, the synthesis of asymmetrical nanoheterostructures has attracted much attention where a spherical CdSe core covered by a rod–shape CdS shell (as seen in Figure 5.2).

Figure 5.2: CdSe/CdS core/shell nanorod.

This asymmetrical heterostructure was firstly reported with linearly polarized photoemission by Talapin et al. [7]. A better control growing process for synthesizing CdSe/CdS core/shell nanorods also has been developed [18, 19]. Since the original work till now, many other seeded–growth heterostructure nanosystems have been synthesized [20, 21]. Besides, metallic particles also can be grown on the surfaces of

© 2012 Tous droits réservés.

core/shell nanorods in order to enhance the extracting carriers for different types of applications [22]. However, all these studies have not yet been able to conclude whether holes and electrons localize in the CdSe core or in the CdS shell. The early works showed that the electrons might be outside the core [23, 24], whereas, later experiments indicated that both electrons and holes might reside in the CdSe core [4, 7]. There is more than one factor that makes the determination of carrier localizations complex. Along with the band alignment, there are also the effects of quantum confinement, the dipole moment, and the electrical field caused by the piezoelectric effects [25]. By using *ab initio* methods, Y. Luo et al. [26] have shown that the hole wave functions are localized inside the CdSe core and the electron wave functions are localized in the shell, but, it can be very close to the core, depending on the surface passivation. Additionally, the control of the degree of electron localization in the lowest conduction band level by changing the size of the core and the experimental measurement temperature has been reported recently [27]. As there is no consensus on the charge carrier localization, we have investigated the electronic properties of CdSe/CdS dot−in−rod with tunneling spectroscopy. In light of the previous chapter where we have shown the tunneling of the same charge carrier on both sides of the band gap, we have decided to revise the carrier localization in this system.

By moving the STM tip along the rod, conductance spectra measured at individual positions were recorded. Based on the difference of the onsets on both signs of the voltage it was possible to determine the position of the core in the CdS rod−shell. It is found that the interpretation of the peaks in the spectra may be more complex than the initial report [4].

5.2. Experimental details

The CdSe/CdS dot−in−rod nanocrystals were prepared in Gent based on the synthesis method described in previous reports [18]. Then the nanorods were deposited on a Gold−Si substrate by using the LB methods (as presented in Chapter 4). To prepare the substrate, a gold filament was heated below a Si(√3×√3)R30°−B surface to evaporate a 10 nm−thick layer of gold (around 120 seconds). The sample was then annealed at 200 °C for 10 mn to ensure a rather smooth surface, see Figure 5.3.

Additionally, SEM (Scanning Electron Microscopy) was combined to observe the morphology of the monolayer of core/shell nanorods on the Au−Si substrate. In our experiments, the CdSe core has a diameter of around 3.5 nm and the rod−like shell has a thickness of ~0.36 nm and the average length is around 20 nm, as deduced from UV−US spectroscopy and transmission electron microscopy (TEM). Immediately after the NC deposition (carried out a Nitrogen glow box), the sample was inserted into a vacuum vessel and transferred to Lille for STM measurements.

We used electrochemically etched tungsten tips and the topography images were acquired in constant current mode, with typical imaging parameters being set−point current of $10 - 50\ pA$ at a bias voltage (applied to the sample) of $3\ V$. The electronic

© 2012 Tous droits réservés.

density of states was obtained by positioning the STM tip above the center of the rods of interest and disconnecting the feedback loop. The tunnel current I was measured as a function of the bias V between the tip and the substrate. The conductance dI/dV was measured simultaneously using a lock-in amplifier (rms modulation 6 mV at 500 Hz) or by numerically differentiating the experimental $I-V$ curves. Typically, a large number of spectra (~100) were acquired on a given point along the rod maintained stable in the monolayer. In general, the measured spectra were reproducible, although discrete shifts of the spectra along the bias axis were observed in some cases. Sets of reproducible $I-V$ and dI/dV spectra were averaged to increase the signal to noise ratio which did not affect the width of the resonances in the spectra.

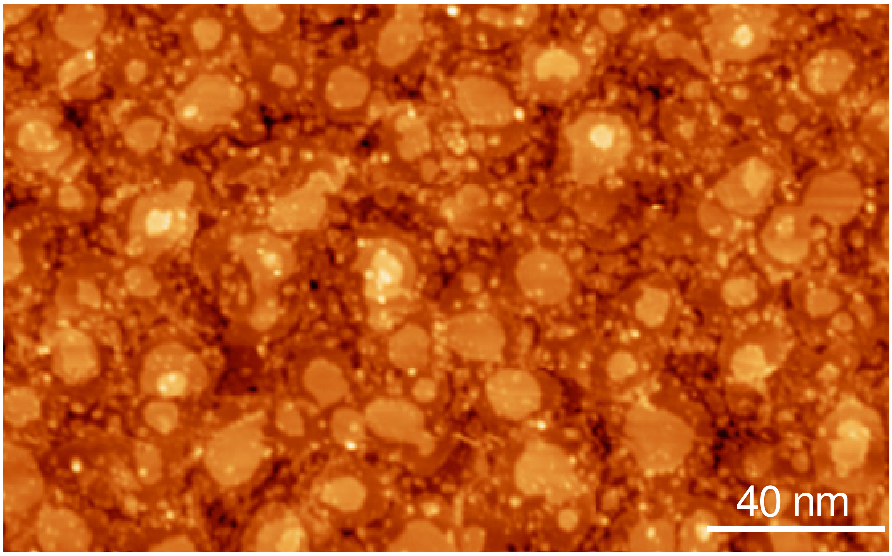

Figure 5.3: Large scale STM image of gold evaporated on Si(√3×√3)R30°–B surface, the contrast varies from 0 to 1.584 nm.

5.3. Experimental results

5.3.1. Observation of colloidal CdSe/CdS Dot–in–Rod nanostructures and absorption spectra

According to the work done by L. Carbone et al. [18], it is possible to synthesize a narrow size distribution of nanorod diameters and lengths. Typical SEM images are presented in Figure 5.4(a) and (b), both images show a narrow dispersion in rod diameters and lengths. Generally, a high–close packed monolayer is found, but in some places the rods appear to be brighter, such rods have been attributed to the formation of the double–layer architectures (see the inset in Figure 5.4(b)). The formation of such architecture could be explained as a result of the change in transfer ratio in the depositing process [28] or a different stacking mechanism [29] or even a random orientation of the rods.

© 2012 Tous droits réservés.

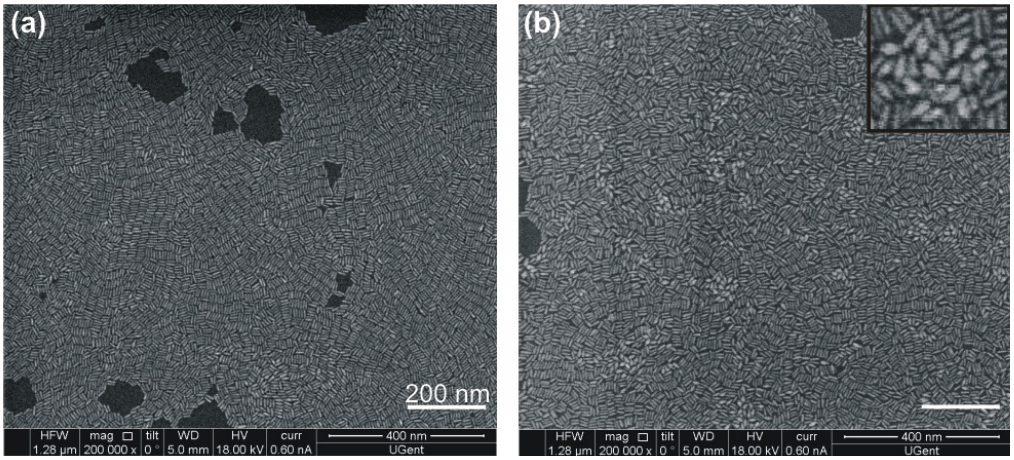

Figure 5.4: Representative SEM images of CdSe/CdS Dot–in–Rod on the Au–Si substrate, the inset in (b) shows the formation of a double–layer architecture in some areas of the monolayer.

In solution, the rods give rise to the absorption spectrum shown in Figure 5.5. It exhibits a small peak followed by an abrupt step. The step is seen at an energy of ~2.6 eV and is attributed to the band gap of CdS. The peak appears at about 2.1 eV (seen more clearly in the inset) and it is ascribed to the CdSe core. These results are in good agreement with previous report, where absorption spectra were performed on a dilute ensemble of CdSe/CdS QDs/NRs dissolved in toluene [4]. Such a peak measured at an onset higher than the CdSe bulk band gap is caused by a confinement effect.

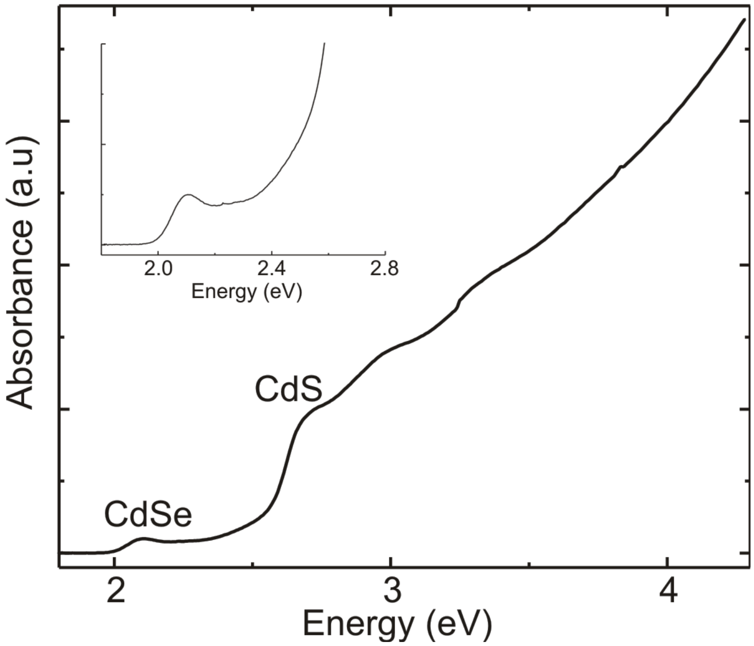

Figure 5.5:Absorption spectra of CdSe/CdS Dot–in–Rod nanostructures

© 2012 Tous droits réservés.

From the absorption spectra alone it is not possible to directly determine either the band–offsets or the electron localization. Probing the electron localization was carried out indirectly by using optical measurements under electric field, where the lifetime measurements are compared with calculated electron–hole overlaps [30]. Nevertheless, it is difficult to relate the exciton lifetime to the band–offsets. Conversely, direct information about the band–offsets and the degree of carrier localizations should be achieved with Scanning Tunneling Spectroscopy (STS) measurements.

5.3.2. STM topography of CdSe/CdS nanorods

A large scale STM image of CdSe/CdS core/shell nanorods on Au–Si substrate is shown in Figure 5.6. The layer shows a high–closed packing of nanorods. At some position in the image, we see a marked difference in contrast in good agreement with SEM image in Figure 5.4(b).

The height difference between the bright positions and the gold substrate (the right lower part in Figure 5.6) was found to be around 8.1 nm. This value refers to a double–layer at the brighter position of the sample surface since the total diameter of the rods is ~4.2 nm and no tilted rods are observed in the layer in contact with the surface.

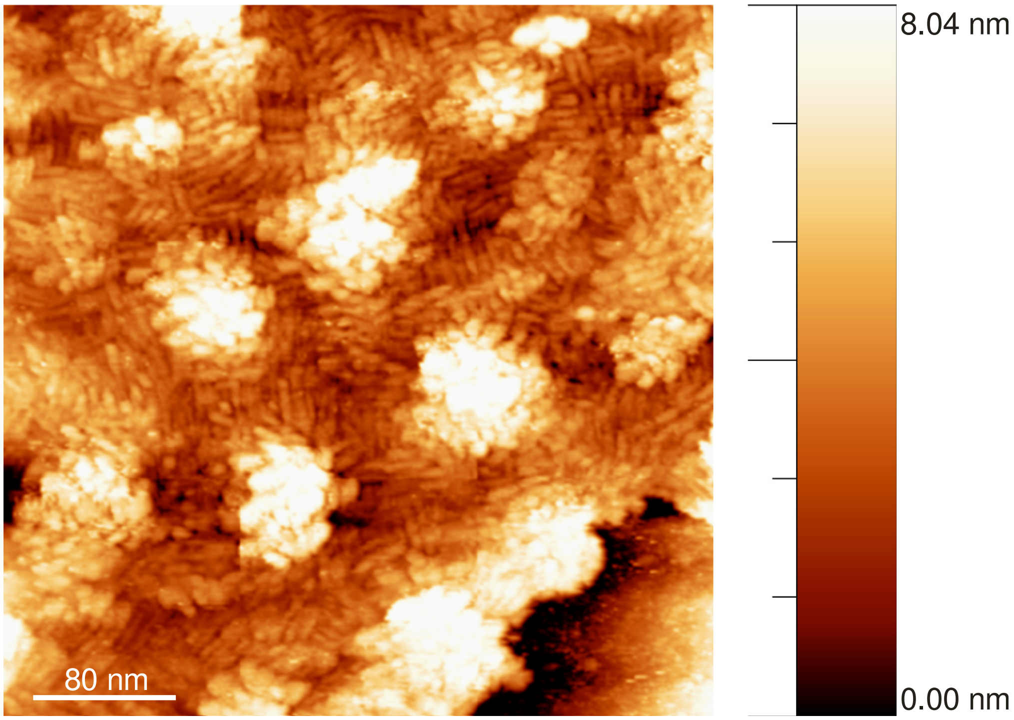

Figure 5.6: Large scale topography image of CdSe/CdS nanorods, the height difference between the brightest point and the gold surface is around 8.1 nm in regards to the CdSe core diameter of ~3.5 nm and the shell thickness of ~0.35 nm.

© 2012 Tous droits réservés.

5.3.3. Spectroscopic measurement of CdSe/CdS core/shell nanorods

Typical spatially resolved differential conductance spectra and corresponding *I–V* spectra are shown in Figure 5.7(a) and (b). While a zero–conductivity gap is observed for all three spectra, the width of this gap is found to vary along the length of the rod. At one of the nanorod end, region (i), it extends over 2.27 eV. Then, for the two others positions, it is much larger. It reaches 3.16 eV in the middle of the rod, region (j), and 3.06 eV at the other end, region (k). Such a result is consistent with a previous STS study on similar rods [4], indicating that the rod is indeed made of two materials with well–contrasted band gaps, the CdSe core being located in the region where the zero–conductivity gap has the smallest value, spectrum (i), since the band gap in the CdSe region is expected to be much smaller.

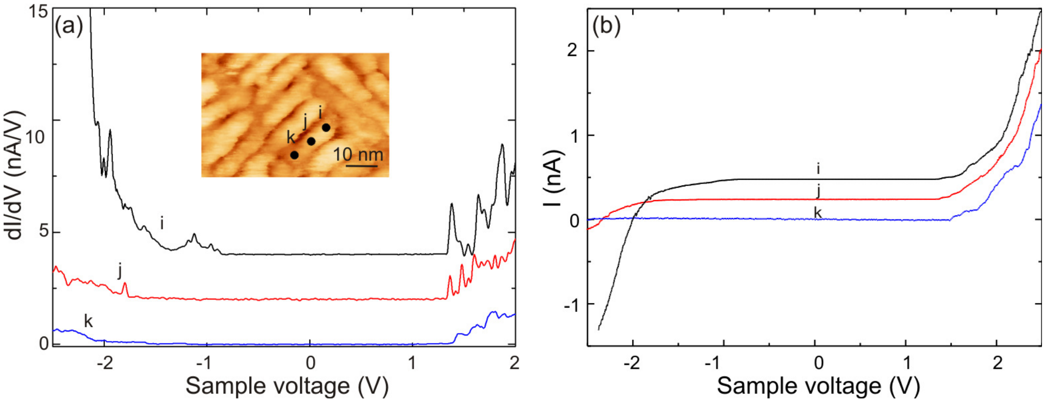

Figure 5.7: (a) Tunneling spectra acquired along the CdSe/CdS nanorod shown in the inset. Feedback conditions: I_{set} = 2 nA, V_s = +2 V, (b) corresponding I–V spectra that have been vertically shifted for clarity.

As already mentioned in Chapter 4, tunneling spectroscopy on core–shell NCs is based on resonant tunneling across a double–barrier tunnel junction (DBJT). If we assume that the potential predominantly drops across the tip–nanorod junction (case where the tip is far from the rod in comparison with the nanorod–substrate distance), then the width of the zero–conductivity gap measured at position (i) is slightly larger than the small absorption onset of 2.1 eV, observed in Figure 5.5 and ascribed to the CdSe core. Therefore the zero–conductivity gap would almost correspond to the quasiparticle gap, with the electrons and holes states probed at positive and negative bias respectively. In such a configuration, the shift of the onset for the conduction and valence states along the nanorod would indicate a delocalization of the electron ground state in the whole rod, whereas the hole ground state would be confined in the core only.

In positions (j) and (k), the measured zero–conductivity region is respectively 3.2 eV and 3.3 eV. Therefore, they are larger than the expected absorption onset of the CdS shell (2.6 eV in Fig. 5.3). Although this effect could be attributed to a lack of

© 2012 Tous droits réservés.

sensitivity in the measurements at lower and lower sample bias [31], preventing the precise observation of the valence band edge, we rather think that the larger zero–conductivity gap arises from the potential distribution across both tunnel junctions. From the conductance spectra, the lever arm η is found to be ~0.82 at position j and k. If the onsets in curve (i) are supposed to be the electron state and hole states in CB and VB of the CdSe core respectively, then, we get a lever arm, η, of 0.92. Such a higher lever arm is difficult to understand and supposes the tip to be far from the rod in comparison with points j and k. This is in contradiction with the presence of a shell that should decrease the transmission probability. Instead, if the onset in CB in curve (i) is attributed to the hole ground state, we get η of ~0.6 based on the equation (4.1) in chapter 4, which was suggested by Y. Niquet et al. [32]. This value seems to be consistent to the study on PbSe/CdSe core/shell NC discussed in chapter 4. The width of both tunnel junctions becomes comparable, of the order of the shell thickness (~0.36 nm) and we should expect a situation with a nearly symmetric potential distribution in the DBJT. While a decrease of the lever arm causes an increase of the zero–conductivity gap with respect to the quasiparticle gap, it can also give rise to more complicated tunneling shemes, leading to bipolar transport for example (see the case of PbSe/CdSe NCs in Chapter 4). Therefore a zero–conductivity gap larger than the quasiparticle gap of CdS questions the assignement of the peaks to electron states at positive sample voltages, in particular in region (i).

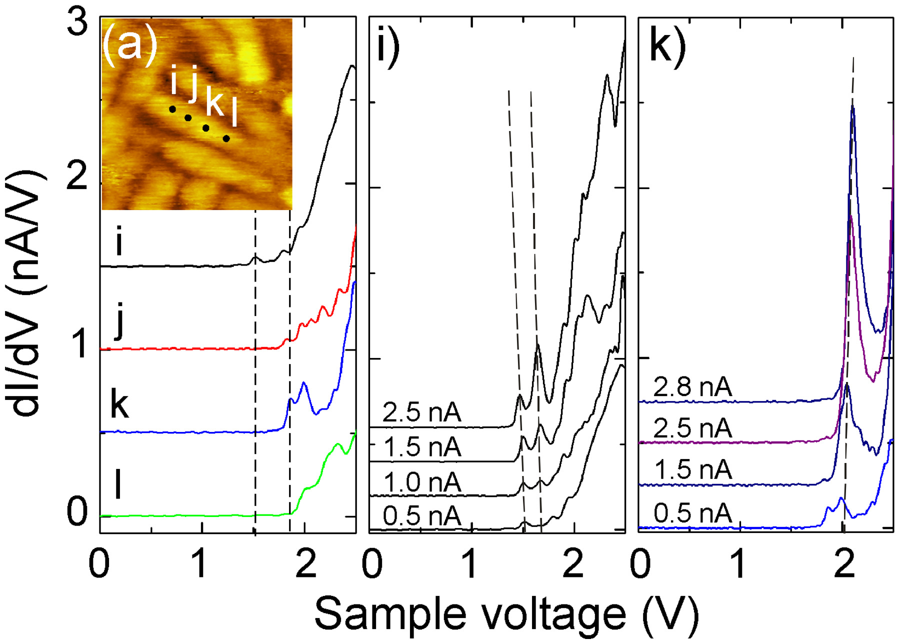

Figure 5.8: (a) Set of tunneling spectra measured along a CdSe/CdS dot-in-rod NC with a set-point current of 0.5 nA. Inset : STM image of the close-packed NC monolayer. (i) and (k) Set the differential conductance spectra acquired at positions i and k along the NC for increasing set-point currents, from 0.5 to 2.8 nA.

© 2012 Tous droits réservés.

Figure 5.8 shows another example of spatially resolved conductance spectra acquired at four different positions along a nanorod. Focussing on the onset of the curves at positive bias, we measure a shift of 0.39 eV between the lowest peak observed in region (i) and the onset of the first step in region (l). While such a result suggests that the core is again located in region (i), discriminating between the contributions of electron or hole states to the conductance spectrum requires to study the change of the onsets as a function of the tunneling current set point. As seen in Figure 5.8(i), an increase of the current set point leads to a shift of the two lowest peaks towards lower energies. This shift is opposite to the expected shift that should occur if electrons were injected through the conduction band ground state of the CdSe core for smaller and smaller lever arms [32]. We thus identify the lowest peaks in spectrum (i) as the contribution of holes states to the tunneling current. Conversely, in the middle of the nanorod, the onset of the spectra (k) shifts towards higher energies as the current setpoint increases, indicating that away from region (i) the current is related to electron states at positive sample voltages.

5.4. Discussion

In order to understand the contribution of the different states, a band diagram can be drawn, as shown in Fig. 5.9. The CdSe core material has a smaller band gap (1.84 eV at 5 K), that resides inside the larger CdS band gap (2.58 eV at 5 K). Numerous experimental results have shown that the CdSe/CdS interface is characterized by a large valence band offset, that confines the hole wave function to the core region of the nanorod. The electron wave function usually extends through the rod [11, 33, 34, 35].

Assuming a Fermi level close to the valence band edge of the CdSe core, then a lever arm close to 0.5 (in this case, the voltage distributions are equal across both tunnelling junctions) would result in the contribution of the hole ground state at both negative and positive sample voltages, as shown in Fig. 5.9(a). Indeed, at positive bias, the tip Fermi level can not reach the electron state before the sample Fermi level becomes aligned with the hole state. This situation is reversed at negative bias, where the sample Fermi level is kept in the band gap while the tip Fermi level becomes resonant with the hole state. Therefore, holes tunnel first on both sides of the zero−conductivity region. If the Fermi level in the NC is far from the valence band edge and most of the potential drop occurs between the tip and the rod, then both electron and hole state are respectively probed at positive and negative bias. This situation is observed in Figure 5.9(b) in the case of the rod. As a result when a core is embedded in a shell material, the potential distribution across the DBJT is strongly affected. Therefore great cares have to be taken to first determine the origin of the electronic states to the conductance spectra. Then the band offset might be measured depending on states that are probed. This was not done in Ref. 4, where the authors assumed a level arm close to one, without measuring it.

© 2012 Tous droits réservés.

http://doc.univ-lille1.fr

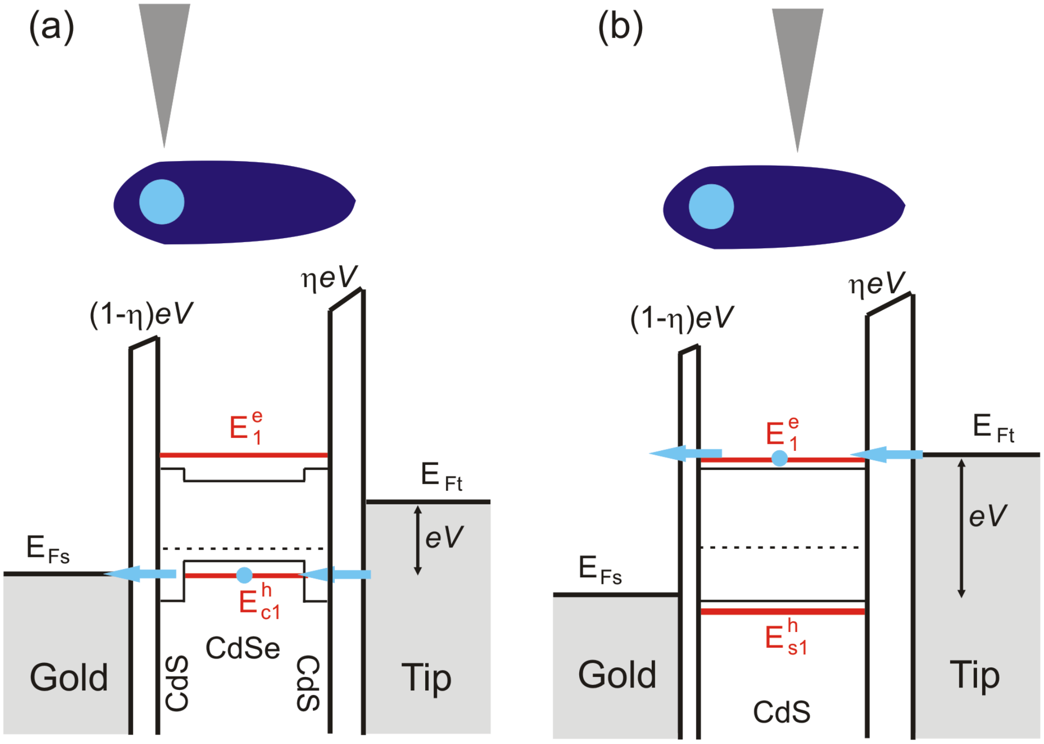

Figure 5.9: Schematic illustration of carriers tunneling through the CdSe core (a) and through CdS shell (b).

5.5. Conclusion

In this Chapter, STM is used to observe the topography of colloidal CdSe/CdS dot–in–rod nanocrystals on Au–Si Substrate. Both SEM and STM images show high close–packed monolayer of rods on the substrate and at some location, a double–layer architecture can be found. The correct arrangement of the latter structure has still to be correctly understood.

With the STS technique, we are able to measure peaks. However, the assignment of the peaks is not straightforward, in particular above the position of the rod that shows the smallest zero–conductivity region. We attribute this position to the core in the rod. Due to the presence of the surrounding shell, measurements at different current set–points are required to correctly interpret the origin of the peaks in the rod. In the ensemble of rods we probe, we found that it is a general fact to measure the hole ground state of the core at positive bias, preventing the measurement of the conduction band offset in these systems.

© 2012 Tous droits réservés.

References

---

[1] S. Coe, W. K. Woo, M. G. Bawendi, and V. Bulovic, “*Electro−luminescence from Single Monolayers of Nanocrystals in Molecular Organic Devices*”, Nature **420**, 800−803 (2002).

[2] N. C. Greenham, X. Peng, and A. P. Alivisatos, “*Charge Separation and Transport in Conjugated−Polymer/Semiconductor−Nanocrystal Composites studied by Photoluminescene Quenching and Photoconductivity* ”, Phys. Rev. B **54**, 17628 (1996).

[3] V. I. Klimov, A. A. Mikhailovsky, S. Xu, A. Malko, J. A. Hollingworth, C. A. Leatherdale, H. −J. Eisler, and M. G. Bawendi, “*Optical Gain and Stimulated Emission in Nanocrystal Quantum Dots*”, Science **290**, 134 (2000).

[4] D. Steiner, D. Dorfs, U. Banin, F. D. Sala, L. Manna, and O. Millo, “*Determination of Band Offsets in Haterostructured Colloidal Nanorods Using Scanning Tunneling Spectroscopy*”, Nano Lett. **8** (9), 2954−2958 (2008).

[5] D. M. Whang, J. Song, Y. Mu, C. Lieber, M. D. Whang, S. Jin, Y. Wu, and M. C. Lieber, “*Large−Scale Hierarchical Organization of Nanowire Arrays for Intergarated Nanosystems*”, Nano Lett. **3**, 1255−1259 (2003).

[6] R. D. Robinson, B. Sadtler, D. O. Demchenko, C. K. Erdonmez, L. W. Wang, and A. P. Alivisatos “*Spontaneous Superlaticce Formation in Nanorods through Partial Cation Exchange*”, Science **317**, 355−358 (2007).

[7] D. V. Talapin, R. Keoppe, S. Gotzinger, A. Komowski, J. M. Lupton, A. L. Rogach, O. Benson, J. Feldman, and H. Weller, “*Emissive Colloidal CdSe/CdS Heterostructures of Mixed Dimensionality*”, Nano Lett. **3**, 1677−1681 (2003).

[8] Y. Xing, Q. Chaudry, C. Shen, K. Y. Kong, H. E. Zhau, L. W. Chung, J. A. Petros, R. M. O’Regan, M. V. Yezhelayv, J. W. Simmons, M. D. Wang, and S. Nie, “*Bioconjugated quantum dots for multiplexed and quantitative immunohistochemistry*”, Nature Protoc. **2**, 1152−1165 (2007).

[9] V. I. Klimov, S. A. Ivanov, J. Nanda, M. Archermann, I. Bezel, J. A. McGuire, and A. Pirytinski, “*Single−exciton optical gain in semiconductor nanocrystals*”, Nature **447**, 441−447 (2007).

[10] S. Kumar, M. Jones, S. S. Lo, and G. D. Scholes, “*Nanorod Heterostructures Showing Photoinduced Charge Separation*”, Small **3**, 1633−1639 (2007).

[11] A. Pandev, and P. Guyot−Sionnest, “*Intraband spectroscopy and band offsets of colloidal II−VI core/shell structures*”, J. Chem. Phys. **127**, 104710 (2007).

[12] B. O. Dabbousi, J. Rodriguez−Viejo, F. V. Mikulec, J. R. Heine, H. Mattoussi, R. Ober, K. F. Jensen, and M. G. Bawendi, “*(CdSe)ZnS Core−Shell Quantum Dots: Synthesis and Characterization of a Size Series of Highly Luminescence Nanocrystallites*”, J. Phys. Chem. B **101**, 9463−9475 (1997).

[13] X. Peng, M. C. Schlamp, A. V. Kadavanich, and A. P. Alivisatos, “*Epitaxial Growth of Highly Luminescent CdSe/CdS Core/Shell Nanocrystals with Photostability and Electronic Accessibility*”, J. Am. Chem. Soc. **119**, 7019−7029 (1997).

© 2012 Tous droits réservés.

---

[14] A. H. Nethercot, "*Prediction of Fermi Energies and Photoelectric Thresholds Based on Electronegativity Concept*", Phys. Rev. Lett. **33**, 1088−1091 (1974).

[15] C. Targer−Cowan, P. J. Parbrook, B. Henderson, and K. P. O'Donnell, "*Band alignments in Zn(Cd)S(Se) strained leyer superlattices*", Semicond. Sci. Technol. **7**, 536–541 (1992).

[16] K. P. O'Donnel, P. J. Parbrook, F. Yang, X. Chen, D. J. Irvine, C. Targer−Cowan, B. Henderson, P. J. Wright, and B. Cockayne, "*The optical properties of wide bandgap binary II−VI superlattices*", Cryst. Growth **117**, 497−500 (1992).

[17] K. H. Hellwege, and O. Madelung, "*Numerical Data and Functional Relationships in Science and Technologies*", Landolt−Börnstein, New Series, Group III, Vol. **17b**, Springer−Verlag, Berlin (1982).

[18] L. Carbone, C. Nobile, M. D. Giorgi, F. D. Sala, G. Morello, P. Pompa, M. Hytch, E. Snoeck, A. Fiore, I. R. Franchini, et al., "*Synthesize and Micrometer−Scale Assembly of Colloidal CdSe/CdS Nanorods Prepared by a Seeded Growth Approach*", Nano Lett. **7**, 2942−2950 (2007).

[19] D. V. Talapin, J. H. Nelson, E. V. Shevchenko, S. Aloni, B. Sadtler, and A. P. Alivisatos, "*Seeded Growth of Highly Luminescent CdSe/CdS Nanoheterostructures with Rod and Tetrapod Morphologies*", Nano Lett. **7**, 2951−2959 (2007).

[20] A. Fiore, R. Mastria, M. Grazia−Lupo, G. Lanzani, C. Giannini, E. Carlino, G. Morello, M. D. Giorgi, Y. Li, R. Cingolani, et al., "*Tetrapod−Shaped Colloidal Nanocrystals of II−VI Semiconductors Prepared by Seeded Growth*", J. Am. Chem. Soc. **131**, 2274−2282 (2009).

[21] P. Reiss, M. Protiere, and L. Li, "*Core/Shell Semiconductor Nanocrystals*", Small **5**, 154−168 (2009).

[22] G. Menagen, D. Mocatta, A. Salant, I. Popov, D. Dorfs, and U. Banin, "*Selective Gold Growth on CdSe Seeded CdS Nanorods*", Chem. Mater. **20**, 6900−6902 (2008).

[23] S. Pokrant, and K. B. Whaley, "*Tight−Binding Studies of Surface Effects on Electronic Structure of CdSe Nanocrystals: The Role of Organic Ligands, Surface Reconstruction, and Inorganic Capping Shells*", Eur. Phys. J. D. **6**, 255−267 (1999).

[24] L. Manna, L. W. Wang, R. Cingolani, and A. P. Alivisatos, "*First−Principles Modeling of Unpassivated and Surfactant−Passivated Bulk Facets of Wurtzite CdSe: A Model System for Studying the Anisotropic Growth of CdSe Nanocrystals*", J. Phys. Chem. B **109**, 6183−6192 (2005).

[25] G. Morello, F. D. Sala, L. Carbone, L. Manna, G. Maruccio, R. Cingolani, and M. D. Giorgi, "*Intrinsic Optical Nonlinearity in Colloidal Seeded Grown CdSe/CdS Nanostructures: Photoinduced Screening of the Internal Electric Field*", Phys. Rev. B **78**, 195313 (2008).

[26] Y. Luo, and L. W. Wang, "*Electronic Structures of the CdSe/CdS Core−Shell Nanorods*", ACS Nano **4**, 91−98 (2010).

[27] G. Raino, T. Stöferle, I. Moreels, R. Gomes, J. S. Kamal, Z. Hens, and R. F. Mahrt, "*Probing the Wave Function Delocalization in CdSe/CdS Dot−in−Rod Nanocrystals by Time− and Temperature−Resolved Spectroscopy*", ACS Nano **xxx**, xxx−xxx (2011).

© 2012 Tous droits réservés.

---

[28] Y. J. Shen, Y. L. Lee, and Y. M. Yang, "*Monolayer Behavior and Langmuir−Blodgett Manipulation of CdS Quantum Dots*", J. Phys. Chem. **110**, 9556−9564 (2005).

[29] K. Lambert, R. K. Capek, M. I. Bodnarchuk, M. V. Kovalenko, D. V. Thourhout, W. Heiss, and Z. Hens, "*Langmuir−Schaefer Deposition of Quantum Dot Multilayers*", Langmuir **26**, 7732−7736 (2010).

[30] J. Müller, J. M. Lupton, P. G. Lagoudakis, F. Schindler, R. Koeppe, A. L. Rogach, and J. Feldmann, "*Wave Function Egineering in Elongated Semiconductor Nanocrystals with Heterogeneous Carrier Confinement*", Nano Lett. **5**, 2044−2049 (2005).

[31] R. M. Feenstra, J. A. Stroscio, and A. P. Fein, "*Tunneling spectroscopy of the Si(111)2 × 1 surface*", Surf. Sci. 181, 295 (1987)

[32] Y. M. Niquet, C. Delerue, and G. Allan, "*Interpretation and theory of tunneling experiments on single nanostructures*", Phys. Rev. B **65**, 165334 (2002).

[33] J. Muller, J. M. Lupton, A. L. Rogach, J. Feldmann, D. V. Talapin, and H. Weller, "*Monitoring Surface Charge Movement in Single Elongated Semiconductor Nanocrystals*", Phys. Rev. Lett. **93**, 167402 (2004).

[34] J. Muller, J. M. Lupton, P. G. Lagoudakis, F. Schindler, R. Koeppe, A. L. Rogach, J. Feldmann, D. V. Talapin, and H. Weller, "*Wave Function Engineering in Elongated Semiconductor Nanocrystals with Heterogeneous Carrier Confinement*", Nano Lett. **5**, 2044−2049 (2005).

[35] M. G. Lupo, F. D. Sala, L Carbone, M. Zavelani−Rossi, A. Fiore, L. Luer, D. Polli, R. Cingolani, L. Manna, and G. Lanzani, "*Ultrafast Electron−Hole Dymanics in Core/Shell CdSe/CdS Dot/Rod Nanocrystals*", Nano Lett. **8**, 4582−4587 (2008).

© 2012 Tous droits réservés.

© 2012 Tous droits réservés.

Conclusion

The goal of this thesis was to study the electronic structure of novel colloidal particle composed of two types of semiconductor compounds. In the hetero-nanocrystals, the control of the band offset at the interface between both compounds is crucial to localize charge carriers with opposite signs in the same materials or to spatially separate both types of charge carriers.

Due to its unique resolution, scanning tunneling microscopy is a technique of choice to locate hetero-nanocrystals on a metallic surface. Taking advantage of the spectroscopic capability of this technique further allows to probe the quantized levels of individual quantum dots, when the electronic levels of the dots are weakly coupled to the electrodes. However, the identification of the resonances observed in the tunneling spectra is not straightforward. Charging effects might occur and as a result, a preliminary study has been performed on a prototypical system : an isolated Si dangling bond at the surface of a B–doped Si(111)–($\sqrt{3}$x$\sqrt{3}$)R30°. In order to change the charge state of the dangling bond, the occupation probability of the dangling bond has been tailored so that the Coulomb interaction between two electrons in the same atomic orbital was measured.

Based on this experience, the electronic structure of PbSe/CdSe core-shell nanocrystals has been investigated by tunneling spectroscopy. A wider apparent band gap has been reproducibly measured in the spectra with respect to spectra obtained on PbSe nanocrystals without a shell. Such effect has been assigned to a symmetrical potential drop in both tunnel junctions and leads to a transport regime where only one type of charge carriers contribute to the current whatever the polarization of the system is. The presence of a shell thus favors the charging of the dot and we were able to measure the charging energy of the s-level for dots with a PbSe core diameter around 7 nm.

A second type of hetero-nanocrystals has also been studied: CdSe/CdS dot–in–rod nanocrystal. Again, it has been found that transport through the core involves the same electronic state at both positive and negative biases. Thus, such situation makes the determination of the band offset difficult, since we have not been able to measure the electron ground state in the core and we lack of sensitivity to accurately probe the hole ground state in the CdS shell. However, the spatial localization of the core has been demonstrated and open new perspectives, in particular for nanorods with type II band-alignment. This new nanorods usually consists of two segments, where one of the segments can even be embedded in a thin shell. Such nanorods are very attractive for solar cells applications, since the charge carriers can be efficiently separated and their escape towards electrodes under an electric field should be easier.

© 2012 Tous droits réservés.

© 2012 Tous droits réservés.

http://doc.univ-lille1.fr

© 2012 Tous droits réservés.

Abstract

Semiconductor colloidal nanocrystals are quite attractive, because of their physical properties, such as discrete energy levels, which can be easily tailored from the variation of their size and chemical composition, and also because of their compatibility with the fabrication of low–cost electronic devices. However, devices prepared from semiconductor nanocrystals are still facing limitations due to a high environmental sensitivity of their organic shell. In order to increase their optical properties, core–shell nanocrystals have thus been synthesized, where a new degree of freedom is offered by the presence of a junction between two types of semiconductor material. Scanning tunneling microscopy is the appropriate tool to image and probe the electronic properties of individual nanostructures and, in particular, of heterostructure nanocrystals. This system can be compared to a double barrier tunnel junction, where the transport properties are governed by the transmission probability across both potential barriers (chapter 1). In principle, the synthesis of an homogenenous shell around the core should thus favor the charging phenomena.

In order to investigate the Coulomb effect in those quantum objects by tunneling spectroscopy (this technique being described in chapter 2), the thesis has first focussed on a prototypical model: an isolated silicon dangling bond, where its charge state has been changed in a controlled manner (chapter 3). Then, PbSe/CdSe core-shell nanocrystals have been studied and a general method is described to correctly identify the electrical nature of the charge carriers in the tunneling spectra (chapter 4). In contrast to nanocrystals that are covered by a layer of ligands only, the transport through core-shell structures reveals, for a majority of nanocrystals, that the same type of charge carrier tunnel on both sides of the apparent gap. Charging peaks are also observed and allow the measurements of the charging energy in these systems. A similar transport regime is obtained for CdSe/CdS dot in rod nanocrystals (chapter 5), demonstrating the reproducibility of the characterized transport phenomena when the nanocrystals consist of a heterostructure.

Résumé

Les nanocristaux semi-conducteurs possèdent des tailles qui se situent entre celles des molécules et des matériaux cristallins. Leurs propriétés physiques sont donc dominées par des effets de confinement quantique, leur spectre d'énergie étant caractérisé par des états électroniques discrets. Une telle structure électronique leur confère d'être des sources de lumière de longueur d'onde accordable, très prisées pour l'imagerie biologique. Cependant, pour palier aux problèmes de photostabilité et accroître les applications potentielles de ces objets, des nanocristaux à hétérostructures, formés généralement d'un cœur et d'une coquille, de composition chimique différente du cœur, ont été synthétisées ces dernières années. Une étude approfondie de leur structure électronique et en particulier de la localisation des porteurs de charge s'avère nécessaire pour pouvoir à plus long terme faire de l'ingénierie de structure de bande de manière similaire à ce qui existe avec des hétérostructures semi-conductrices réalisées à partir de matériaux massifs. La microscopie à effet tunnel est l'outil idéal pour imager et sonder les propriétés électroniques de nanocristaux individuels déposés sur une surface. Le système peut être comparé à une jonction tunnel à doublé barrière tunnel, dont les propriétés de transport sont en partie déterminees par les probabilités de transmission au travers de chaque barrière de potentiel (chapitre 1). A priori, la présence d'une coquille homogène autour du cœur doit favoriser le blocage de Coulomb dans de tels nanocristaux.

Pour caractériser les effets de Coulomb dans des objets quantiques par spectroscopie tunnel (technique détaillée au chapitre 2), mes travaux de recherche ont tout d'abord porté sur un système modèle : une liaison pendante silicium, dont l'état de charge a pu être modifié de manière contrôlée (chapitre 3). Des nanocristaux cœur–coquille (PbSe/CdSe) à symétrie sphérique ont ensuite été étudiés (chapitre 4). Pour lever toute ambiguïté sur la nature électrique des porteurs de charge, les mesures sont effectuées en variant l'épaisseur de la jonction tunnel entre la pointe et les nanocristaux. Contrairement aux nanocristaux sans coquille, les expériences révèlent que le transport est dominé par le même type de porteurs de charge à polarisation positive et négative de la jonction. Ces mesures donnent également accès à l'énergie de charge des nanocristaux. Un régime de transport similaire est obtenu pour des nanobâtonnets constitués d'un cœur sphérique CdSe enfermé dans un bâtonnet de CdS (chapitre 5), démontrant la reproductibilité des phénomènes observés lorsque les nanocristaux sont constitués d'hétérostructures cœur–coquille.

© 2012 Tous droits réservés.